



**London  
South Bank  
University**

# An Acoustic Emission Technique for Monitoring the Liquefied Natural Gas Cargo Tank

Farhan Tanvir Santo

<https://orcid.org/0000-0003-4159-3642>

This thesis is submitted to London South Bank University for the degree of Doctor of  
Philosophy

This research program was carried out in collaboration with London South Bank University  
and Lloyds Register Foundation

August 2019

# Abstract

Increase in the market of supersized LNG (Liquefied Natural Gas) vessel, with doubled walled cargo tanks, has led to concerns regarding their safe operations. If both the primary and secondary wall of the cargo tank fails simultaneously, the hull of the vessel can be exposed to the LNG's. This has the potential to cause brittle failure of the hull structure. This research presents a new Acoustic Emission (AE) technique that can be implemented to monitor the structural condition of the primary wall in the LNG cargo tank. The presented technique is able to provide information regarding critical damage so that appropriate maintenance can be carried out to avoid catastrophic failure.

Acoustic Emission (AE) is a passive Non-Destructive Testing (NDT) technique, employed to identify critical damage in structures before failure can occur. Currently, AE monitoring is carried out by calculating the features of the waveform received by the AE sensor. User defined settings (*i.e.* timing and threshold) in the AE data acquisition system significantly affects many traditional AE features such as count, energy, centroid frequency, rise-time and duration. In AE monitoring, AE features are strongly related to the damage sources. Therefore, AE features, calculated due to inaccurate user defined acquisition settings can result in inaccurately classified damage sources. The new AE technique presented in this study is based on an AE feature of the waveform, which is independent of some user defined parameter (*i.e.* timing and threshold) used in the AE data acquisition system, unlike many traditional AE features. The presented AE feature is referred to as AE entropy in this research and is a measure of randomness in the waveform calculated using quadratic Renyi's entropy.

The effectiveness of AE entropy is evaluated by comparing it and traditional AE features under ideal conditions for a range of varying acquisition settings. Unlike the traditional feature, the AE entropy showed no variance with the acquisition settings and was effective in identifying different waveform shapes. The AE entropy was validated through fatigue and tensile tests on coupon specimens of austenitic stainless steel (material of the primary wall). The result suggested that AE entropy is effective in identifying the critical damages in austenitic stainless steel, irrespective of the data acquisition settings. Since AE entropy reduces the human

involvement with the data acquisition system and can identify damages, it has the potential to be implemented in the commercial AE data acquisition system.

# Acknowledgement

أَلْحَمْدُ لِلَّهِ

I am truly grateful to be given the strength and patience for conducting this research. I dedicate this achievement to my family, who have been extremely supportive throughout these years. Firstly, I would like to thank my father and mother for the sacrifices they have made to get me this far with my studies and motivating me throughout my life. I would like to thank my wife for her patience on me while I was away from her for this research. I would like to thank my brother for his mental support. I would like to express my sincere gratitude to the director of studies Professor Tariq Pervez Sattar and my second supervisor Professor David Mba for the guidance and support with this research. I would also like to express my sincere gratitude to Graham Edwards for sharing his industrial knowledge and expertise. I have gathered immense knowledge and experience through their supervision. Lastly, I would like to thank London South Bank University, TWI Cambridge and London South Bank Innovation Centre for giving me the opportunity and funding to undertake this research.

# Contents

Abstract.....	II
Acknowledgement .....	IV
List of Figures .....	IX
List of Tables .....	XVI
Abbreviations.....	XVII
1 Introduction.....	1
1.1 Industrial problem.....	1
1.2 Drawback of state of the art solution .....	5
1.3 Aim and objectives .....	7
1.4 Summary of contribution to knowledge .....	7
1.5 Organisation of thesis .....	8
1.6 List of publication.....	10
1.7 Chapter summary .....	10
2 Review of the Acoustic Emission technique used in Condition Monitoring .....	12
2.1 Fundamentals of AE .....	12
2.1.1 Introduction.....	12
2.1.2 AE source localization .....	14
2.1.2.1 Linear localization algorithm.....	15
2.1.2.2 Planner localization algorithm.....	16
2.1.3 Wave Modes .....	18
2.1.3.1 Waves in infinite media.....	18
2.1.3.2 Waves in semi finite media .....	20
2.1.3.3 Waves in finite media .....	20
2.1.4 Attenuation.....	22
2.2 Damage Monitoring with AE.....	23
2.2.1 Application of AE in Fatigue Analysis .....	24
2.2.2 Application of AE in Tensile Analysis .....	29

2.2.3	Low Temperature AE .....	32
2.2.4	Noise Filtration using AE .....	34
2.3	Drawback of traditional Acoustic Emission Monitoring.....	35
2.4	Chapter summary .....	36
3	Methodology.....	38
3.1	First step of proposing a new AE feature.....	38
3.1.1	Exploration of independent waveform feature .....	38
3.1.2	Disorderness of the waveform as a new feature .....	42
3.1.3	Evaluation of the new feature .....	44
3.1.3.1	Performance against Threshold .....	44
3.1.3.1.1	Influence of threshold on Modelled Waveform .....	45
3.1.3.1.2	Influence of threshold on Pencil Lead Break test .....	46
3.1.3.2	Performance against Hit Definition Time .....	48
3.1.3.2.1	Influence of HDT on Modelled waveform.....	48
3.1.3.2.2	Influence of HDT on the elastic wave generated form AE sensor.....	49
3.1.3.3	Performance against disorderness .....	51
3.2	Experimental validation on standard specimen .....	52
3.2.1	Fatigue Test.....	52
3.2.1.1	Materials and Specimen.....	52
3.2.1.2	AE Testing Procedure.....	53
3.2.1.3	Secondary Monitoring Technique .....	55
3.2.1.3.1	Global Strain Measurement in fatigue .....	55
3.2.1.3.2	Digital Image Correlation measurement in Fatigue .....	56
3.2.1.4	Loading Condition.....	57
3.2.1.5	The experimental Setup.....	59
3.2.2	Tensile Test.....	59
3.2.2.1	Materials and Specimen.....	60
3.2.2.2	AE Testing Procedure.....	60
3.2.2.3	Secondary Monitoring Technique .....	61
3.2.2.3.1	Digital Image Correlation measurement in Tensile Deformation .....	62
3.2.2.3.2	Global strain measurement in tensile deformation.....	63
3.2.2.4	Loading Condition.....	64

3.3	Chapter summary .....	65
4	Results .....	66
4.1	Initial Evaluation of the new feature.....	66
4.1.1	Performance against threshold.....	66
4.1.1.1	Evaluation with the modelled waveform.....	66
4.1.1.2	Evaluation with a PLB test .....	70
4.1.2	Preformation against Hit Definition Time .....	72
4.1.2.1	Evaluation with a modelled waveform.....	73
4.1.2.2	Evaluation with the elastic wave generated from AE sensor .....	76
4.1.3	Performance against disorderness.....	77
4.2	Results of Fatigue Test.....	79
4.2.1	Secondary Monitoring Technique of Fatigue Test .....	79
4.2.1.1	Global Strain.....	79
4.2.1.2	Digital Image Correlation in Fatigue Test.....	80
4.2.2	AE Data Filtration.....	82
4.2.3	Correlation of AE monitoring with global strain.....	82
4.2.4	Correlation of AE monitoring with DIC for fatigue test.....	88
4.3	Results of Tensile Test.....	95
4.3.1	Secondary monitoring technique of tensile test .....	95
4.3.1.1	Strain extraction with Digital Image Correlation. ....	95
4.3.1.2	Comparison of material response extracted from DIC and global strain measurement. ....	96
4.3.2	Correlation of AE monitoring with DIC for tensile test .....	101
4.4	Chapter summary .....	106
5	Discussion.....	108
5.1	Correlation between standard test on coupon specimen and real structures under operation.....	108
5.2	Factors affecting AE entropy computation .....	117
5.3	Advantage of Renyi's entropy over Shannon's entropy .....	120

5.4	Effect of noise on Renyi’s entropy .....	125
5.5	Chapter summary .....	127
6	Conclusion and Future Work.....	129
6.1	Conclusions and contribution .....	129
6.2	Future Work .....	132
	References.....	134
	Appendix A.....	142
A.1	Equation for the modelled waveform.....	142
A.2	Dispersion curve of the material used in this study.....	142
A.3	Specification ARAMIS 3D 5MP system (DIC camera) .....	143
A.4	Representation of the increase in strain.....	143
A.5	Postulates of Renyi’s and Shannon’s Entropy .....	143

# List of Figures

Figure 1-1: Membrane type LNG vessel .....	2
Figure 1-2: (a) Cargo tank in membrane type LNG vessel, (b) A section of the cargo tank - highlighting the wall and insulation .....	2
Figure 1-3: Sloshing impact location: (a) Low filling condition (b) High filling condition...	3
Figure 1-4: Permanent deformation in the primary barrier due to sloshing .....	3
Figure 1-5: Failure of the primary barrier due to sloshing .....	3
Figure 1-6: An overview of the thesis structure.....	9
Figure 2-1: AE working principle.....	13
Figure 2-2: Definition of AE features: (a) Rise-time, Peak-amplitude, Duration (b) Energy (c) Count .....	14
Figure 2-3: Linear localization methods .....	15
Figure 2-4: Planner localization methods with two AE sensor.....	17
Figure 2-5: Planner localization methods using three sensors.....	18
Figure 2-6: A propagating longitudinal.....	19
Figure 2-7: A propagating transverse wave .....	19
Figure 2-8: Rayleigh Wave .....	20
Figure 2-9: Love Wave .....	20
Figure 2-10: Symmetric wave mode .....	21
Figure 2-11: Antisymmetric wave mode .....	21
Figure 2-12: Phase velocity of Aluminium .....	22
Figure 2-13: Group velocity of Aluminium .....	22
Figure 2-14: A typical plot of crack growth rate against stress intensity factor range .....	25
Figure 2-15: AE count rate against the crack propagation rate of different specimen.....	26

Figure 2-16: A comparison between AE and linear elastic fracture mechanics transition..	27
Figure 2-17: An illustration of the S-N curve .....	27
Figure 2-18: Cumulative energy against the number of cycles generated from fatigue of un-notched austenitic stainless steel .....	28
Figure 2-19: Cumulative count against the number of cycles generated from fatigue of un-notched austenitic stainless steel.....	29
Figure 2-20: Count rate against the number of cycles generated from fatigue of un-notched Incoloy 901 .....	29
Figure 2-21: Typical stress strain curve for a ductile material.....	30
Figure 2-22: Trend in AE activity during tensile deformation of austenitic stainless steel.	31
Figure 2-23: AE activity and load for specimen strained at low temperature .....	33
Figure 2-24:Relationship of fracture toughness with temperature recorded with: (1) GOST 25.506-85 and (2) AE .....	33
Figure 2-25: Cumulative energy released by concrete mixtures due to cryogenic cooling .	34
Figure 3-1: (a) VS-900 AE sensor (b) Frequency sensitivity spectrum of the sensor .....	39
Figure 3-2: AMSY-6 AE data acquisition system .....	39
Figure 3-3: Experimental setup for model waveform test .....	46
Figure 3-4: Nature of the waveform pulsed from signal generator to AMSY-6 system.....	46
Figure 3-5: Experimental setup for pencil lead break test .....	47
Figure 3-6: Nature of the waveform pulsed from the signal generator.....	49
Figure 3-7: Rectangular pulsing pattern.....	50
Figure 3-8: Sensor arrangement .....	50
Figure 3-9: Waveforms with SNR .....	51
Figure 3-10: Illustration of the fatigue specimen used in the test .....	53
Figure 3-11: (a) VS-160 AE sensor (b) Frequency sensitivity spectrum of the sensor .....	53

Figure 3-12: Sensor Setup in the fatigue specimen.....	54
Figure 3-13: ARAMIS 5M DIC Camera .....	57
Figure 3-14: Speckle pattern in the gauge of fatigue specimen.....	57
Figure 3-15: An Image taken by DIC camera, during a fatigue test.....	58
Figure 3-16: Schematic of Loading Condition in fatigue test.....	58
Figure 3-17: (a) The experimental Setup for fatigue test (b) The schematic of the experimental setup .....	59
Figure 3-18: Illustration of the tensile specimen used in this test.....	60
Figure 3-19: Sensor Setup in the tensile specimen .....	61
Figure 3-20: Speckle pattern in the gauge of tensile specimen.....	63
Figure 3-21: An image taken by DIC camera during tensile deformation.....	63
Figure 3-22: Loading Condition of tensile specimens .....	64
Figure 4-1: Influence of acquisition threshold on waveform 1: (a) Rise-time (b)Duration (c)Count (d)Energy (e)Peak-amplitude and (f) AE entropy .....	67
Figure 4-2: Influence of acquisition threshold on waveform 2: (a) Rise-time (b)Duration (c)Count (d)Energy (e)Peak-amplitude and (f) AE entropy .....	68
Figure 4-3: Influence of acquisition threshold on waveform 3: (a) Rise-time (b)Duration (c)Count (d)Energy (e)Peak-amplitude and (f) AE entropy .....	69
Figure 4-4: Influence of acquisition threshold on waveform generated from PLB: (a) Rise- time (b)Duration (c)Count (d)Energy (e)Peak-amplitude and (f) AE entropy .....	72
Figure 4-5: (a) Waveform recorded by the first channel (b)Waveform recorder by the first channel multiplied by multiplied by 2nd standard deviation and added SNR of 10. ...	73
Figure 4-6: Waveform generated from cyclic plastic zone in austenitic stainless steel.....	74
Figure 4-7: Acquired modelled waveform for HDT OF 200 $\mu$ s.....	75

Figure 4-8: Influence of HDT on modelled waveform (a) Rise-time (b)Duration (c)Count (d)Energy (e)Peak-amplitude and (f) AE entropy .....	75
Figure 4-9:Acquired AE waveform for HDT of 200 $\mu$ s. ....	77
Figure 4-10: Influence of HDT on a realistic AE waveform (a) Rise-time (b)Duration (c)Count (d)Energy (e)Peak-amplitude and (f) AE entropy .....	77
Figure 4-11: Sensitivity of AE entropy to the disorderness.....	78
Figure 4-12: Variance of %strain with time for the entire length of fatigue test (a) specimen 1 (b) specimen 2.....	80
Figure 4-13: DIC Images of specimen 4: (a) Reference stage (b) at 10000s (c) at 23636s (d) at 25084s (e) at 25265s (f) at 25446s (g) at 25627s. ....	81
Figure 4-14: DIC Images of specimen 3: (a) Reference stage (b) at 10000s (c) at 21556s (d) at 22911s (e) at 23250s (f) at 23590s (g) at 23928s .....	81
Figure 4-15: Unfiltered cumulative count of the AE event captured during fatigue test of: (a) Specimen 1, (b) Specimen 2, (c) Specimen 3 and (d) Specimen 4 .....	83
Figure 4-16: Filtered cumulative count of the AE event captured during fatigue test of: (a) Specimen 1, (b) Specimen 2, (c) Specimen 3 and (d) Specimen 4.....	83
Figure 4-17: a) First specimen at the end of test (b) Second specimen at the end of test....	84
Figure 4-18: Variation of AE features with time for the first specimen (a) Rise-time (b)Duration (c)Count (d)Energy (e)Peak-amplitude and (f) AE entropy .....	85
Figure 4-19: Variation of AE features with time for the second specimen (a) Rise-time (b)Duration (c)Count (d)Energy (e)Peak-amplitude and (f) AE entropy .....	86
Figure 4-20: Comparison of cumulative feature for the first specimen .....	87
Figure 4-21: Comparison of cumulative feature for the second specimen .....	88
Figure 4-22: (a) Third specimen at the end of test (b) Fourth specimen at the end of test. .	89

Figure 4-23: Variation of AE features with time for the third specimen: (a) Rise-time (b)Duration (c)Count (d)Energy (e)Peak-amplitude and (f) AE entropy .....	92
Figure 4-24: Variation of AE features with time for the fourth specimen: (a) Rise-time (b)Duration (c)Count (d)Energy (e)Peak-amplitude and (f) AE entropy .....	93
Figure 4-25: Comparison of cumulative feature for the third specimen .....	93
Figure 4-26: Comparison of cumulative feature for the fourth specimen.....	94
Figure 4-27: Images of displacement fields of a un-notched specimen (a) Reference stage (b) Prior to the onset of yielding .....	95
Figure 4-28: Images of displacement fields in the notched specimen (a) Reference stage (b) Prior to the onset of yielding .....	95
Figure 4-29: Material response of the first Un-notched specimen (a) For the entire length of the test (b) up to 0.02 strain .....	97
Figure 4-30: Material response of the second Un-notched specimen (a) For the entire length of the test (b) up to 0.02 strain .....	98
Figure 4-31: Material response of the notched specimen (a) For the entire length of the test (b) up to 0.02 strain.....	98
Figure 4-32:Material response extracted by Global strain.....	99
Figure 4-33:Material response extracted by DIC.....	99
Figure 4-34: Displacement fields at 0.3 strain (a) Un-notched specimen, (b) Notched specimen .....	100
Figure 4-35: Displacement fields at 0.45 strain (a) Un-notched specimen, (b) Notched specimen .....	100
Figure 4-36: Displacement fields at 0.52 strain (a) Un-notched specimen, (b) Notched specimen .....	101

Figure 4-37: Variation of AE features with the material response for the first un-notched specimen: (a) Rise-time (b)Duration (c)Count (d)Energy (e)Peak-amplitude and (f) AE entropy.....	102
Figure 4-38: Variation of AE features with the material response for the second un-notched specimen: (a) Rise-time (b)Duration (c)Count (d)Energy (e)Peak-amplitude and (f) AE entropy.....	103
Figure 4-39: Variation of AE features with the material response for the notched specimen: (a) Rise-time (b)Duration (c)Count (d)Energy (e)Peak-amplitude and (f) AE entropy .....	105
Figure 4-40: Crack length against strain of the notched specimen .....	106
Figure 5-1: Replicated sloshing impact on a coupon specimen.....	110
Figure 5-2: Pressure time history in a membrane LNG cargo tank .....	110
Figure 5-3: (a) Strain in the fatigue specimen for the entire duration of the test (b) strain in the specimen up to 500s (c) Applied stress up to 500sSinusoidal loading starts after this point .....	114
Figure 5-4: (a) Strain in the fatigue specimen for the entire duration of the test (b) strain in the specimen up to 500s (c) Applied stress up to 500s.....	114
Figure 5-5: Variation of AE features and strain up to 500 seconds: (a)Count, (b) Energy (c) Peak Amplitude and (d) AE entropy .....	115
Figure 5-6: Effect of voltage distribution range on AE entropy: (a) VDR -10 to +10, (b) VDR -20 to +20, (c) VDR -40 to +40, (d) VDR -60 to +60, (e) VDR -80 to +80 and (f) VDR -100 to +100.....	118
Figure 5-7: An AE waveform with a VDR of (a) -10 to +10, (b) -20 to +20, (c) -40 to +40, (d) -60 to +60, (e) -80 to +80 and (f) -100 to +100 .....	119
Figure 5-8: Probability distribution ( in Shannon’s entropy when ‘a’ is 1).....	122

Figure 5-9: (a) Discrete probability distribution raised to the power 2 against VDR (used in Renyi's entropy when 'a' is 2), (b) Discrete probability distribution is raised to the power 3 against VDR ((used in Renyi's entropy when 'a' is 3) (c) Discrete probability distribution is raised to the power 4 against VDR((used in Renyi's entropy when 'a' is 4) .....124

Figure 5-10: Delta entropy against SNR of each entropy technique .....125

Figure 5-11: (a) Original and de-noised waveform of the first fatigue specimen (b) Original and de-noised waveform of the second fatigue specimen .....127

# List of Tables

Table 1:Acquisition Settings for PLB Tests .....	40
Table 2: Acquisition Threshold.....	45
Table 3: Acquisition Settings for modelled waveform - threshold .....	45
Table 4: Threshold for each Channel .....	48
Table 5: HDT for each acquisition.....	49
Table 6: Mechanical Properties.....	52
Table 7:Chemical Composition .....	53
Table 8:Acquisition settings for fatigue test .....	54

# Abbreviations

<b>AE</b>	Acoustic Emission
<b>LNG</b>	Liquefied Natural Gas
<b>IMO</b>	International Maritime Organization
<b>CBM</b>	Condition Based Maintenance
<b>SHM</b>	Structural Health Monitoring
<b>LFL</b>	Lower Flammability Limit
<b>ABS</b>	American Bureau of Shipping
<b>NDT</b>	Non-Destructive Testing
<b>TOA</b>	Time of Arrival
<b>RMS</b>	Root Mean Square
<b>HDT</b>	Hit Definition Time
<b>FPLS</b>	Fixed Page Length Setting
<b>DAPLS</b>	Duration Adopted Page Length Setting
<b>PLB</b>	Pencil Lead Break
<b>SNR</b>	Signal to Noise Ratio
<b>DIC</b>	Digital Image Correlation
<b>VDR</b>	Voltage Distribution Range
<b>DWT</b>	Discrete Wavelet Transform

# 1 Introduction

## 1.1 Industrial problem

Increase in world population and the prosperity of developing countries has resulted in an increase in energy demand. Natural gas is the second largest contributor as an energy source to the global energy needs, currently it accounts for 22% of the global energy consumption [1]. Natural gas produces considerably less pollutant than many fossil fuel (e.g. coal and oil) and is available abundantly. As a result, the contribution of natural gas is rapidly increasing in global energy consumption [2] [3]. Qatar and Australia are the dominant exporters, while Japan, China and South Korea are the dominant importers of natural gas, accounting for almost 50% of the annual natural gas trade [4]. International trade of natural gas usually requires long distance transportation through oceans using supersized tankships. In order to store large amounts of natural gas in tankships for transportation, it is first cooled (down to  $-162\text{ }^{\circ}\text{C}$ ) to liquid state called the Liquefied Natural Gas (LNG) [5]. LNG has 600 times less volume as compared to natural gas. Transportation of LNG through ocean is a mature industry, there was a total trade of 263.1 million tonnes of LNG in 2017 [4].

Tanker ships used for the transportation of LNG are called LNG vessels. There were 473 operational LNG vessels in 2017. These vessels can be categorized into two types: The membrane type and the moss type [6]. Each type of vessel has four cargo tanks. There is a growing preference by the industry for the membrane type LNG vessels because they are cheaper, require a lot less engineering maintenance work and provide a favourable ratio of the volume of cargo to size of the tank [6] [7]. There are 74% membrane type cargo tank and 24% moss type cargo tank in operation in 2017 [4]. Figure 1-1 shows a membrane type LNG vessel [8]. Cargo tanks in the membrane type LNG vessel are double walled and prismatic in shape. The primary wall is constructed from 1.2mm thick corrugated austenitic stainless steel. The primary wall contains the LNG and provides the required tightness for the cargo tank. Figure 1-2 show a cargo tank and its wall [9].



Figure 1-1: Membrane type LNG vessel [8]

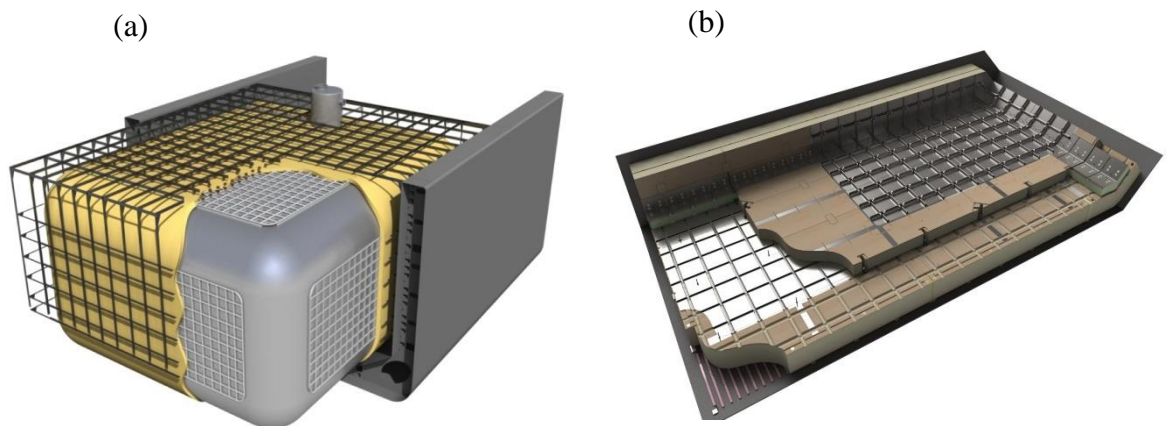


Figure 1-2: (a) Cargo tank in membrane type LNG vessel, (b) A section of the cargo tank - highlighting the wall and insulation [9]

During a voyage, the primary wall of the cargo tank in the membrane type vessel is subjected to a tremendous amount of sloshing impact from the LNG cargo [10] [11] [12]. Sloshing impact arises from violent motion of free surface of LNG cargo inside the tank [6]. Impacts become significantly dominant if the natural frequency of LNG cargo is in resonance with the ship motion [10] [13]. In a low filling condition (*e.g.* 10% to 40% of the tank height) impacts occur at the longitudinal and transverse bulkhead, whereas in a high filling condition (*e.g.* above 70% of the tank height) impacts occur at the corner of the chamfer [13]. Figure 1-3 illustrates the impact locations in the cargo tank in both low and high filling condition. Sloshing impact can sometimes lead to the localized yielding of the primary wall [13][14]. Service experience suggests that the localized yielding in the primary wall of the cargo tank is normally in the corner of the ceiling and may occasionally occur on the lower part of longitudinal and transverse bulkhead (if the vessel is often operated under partial filling condition) [13]. The localized yielding in due course can result in crack initiation, causing LNG to flow out of the primary wall [15][16]. However, if there is a further damage to the

## Introduction

secondary wall, the cryogenic fluid can potentially reach the hull of the vessel causing brittle failure (especially if the leak hole diameter is greater than 5mm) [17][18][19]. Catastrophic failure of the cargo tank can not only cause shutdown of the vessel (cost of vessel shutdown is \$60,000 a day) but also introduce a risk to the safety of life and property (LNG has the potential to cause cryogenic burns to crew members in the vessel).

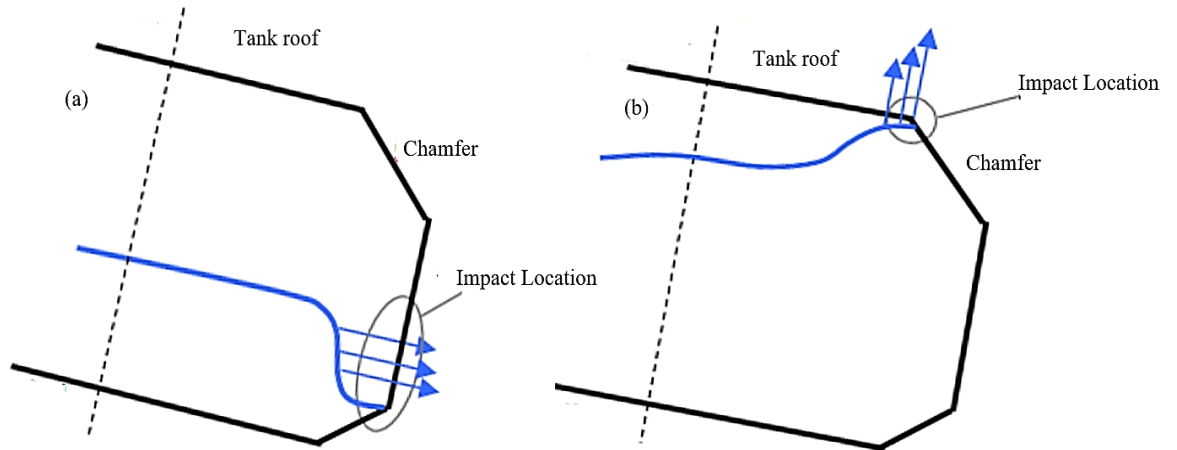


Figure 1-3: Sloshing impact location: (a) Low filling condition (b) High filling condition [13]



Figure 1-4: Permanent deformation in the primary barrier due to sloshing [21]



Figure 1-5: Failure of the primary barrier due to sloshing [22]

To reduce risk of catastrophic failure, the International Maritime Organization (IMO) has introduced regulations focusing on the safe carriage of bulk liquefied gas through the ocean [20]. According to the regulation, the entire cargo tanks in a vessel have to be inspected thoroughly after every five years by a surveyor (e.g. Lloyds Register). Despite the regulations set by IMO, there have been several damages in the primary wall of the cargo tank during voyages, reported by the French LNG carrier manufacturer [21]. Figure 1-4 shows the deformed primary barrier of a cargo tank, in a 138,000m<sup>3</sup> membrane LNG carrier known as the Catalunya Spirit [21]. A detailed investigation revealed that sloshing was the only cause of this deformation. This was the first real evidence of local deformation caused by sloshing. Figure 1-5 shows failure of the primary barrier of a cargo tank in another membrane LNG carrier. Significant sloshing impact under low filling condition was responsible for this failure [22]. In order to successfully minimize risk of catastrophic failure and increase operational availability of the LNG vessel, there is a need to replace the traditional maintenance strategy with a Condition Based Maintenance (CBM) strategy [23].

CBM is a strategy that continuously monitors the structural health condition to predict whether a maintenance is required. In contrast to the traditional maintenance, CBM helps prevent unplanned shutdown and reduces maintenance cost [24]. In cargo tanks, initial stage of damage is the localized yielding and crack initiation. If real-time information regarding the yielding and crack initiation from the primary wall can be achieved, appropriate maintenance can be carried out to avoid further failure. In order to gather real time information about the yielding, structural assessment of the primary wall of the cargo tank with a suitable Structural Health Monitoring (SHM) technique is a primary solution. Determining the severity of damage such as the yielding in a material is a challenging task. To achieve this goal, the SHM technique must be sensitive to the damage mechanism which may span several lengths of time. Considering most of the widely used SHM techniques (e.g. modal analysis, long range guided waves, vibration and Acoustic Emission), only the Acoustic Emission (AE) is capable of identifying the onset of yielding in a material. This research focuses on improving AE monitoring methodology for a better identification of the localized yielding and crack initiation. The newly developed AE monitoring aims to provide effective information regarding the condition (damage) of the primary wall so that a suitable maintenance can be carried out. CBM with AE as a SHM technique will provide more confidence to the operators in relation to safety of the LNG vessel and increase its operational availability.

## 1.2 Drawback of state of the art solution

Growing demand for supersized LNG carriers has led to concerns regarding safety of life and property [17][18]. In order to reduce risk of catastrophic failure (brittle failure of the hull), standards imposed by the IMO made a compulsory requirement for all the LNG carriers to have embedded temperature sensors and gas detection systems (methane), in the insulation between the primary and secondary wall [20][25]. The embedded temperature sensors continuously monitor the temperature changes of the insulation. When there is a leak in the primary wall, the LNG flows to the insulation panel and reduces the temperature of the region of the insulation. The formation of these cold spots are detected by the temperature sensor. The embedded temperature sensors provide warning in case of critical cold spot formation (due to leakage). The gas detection system measures concentration of gas (0 to 100% by volume) in the insulation space, between the primary and secondary wall. In the membrane type LNG carrier, an alarm is activated when the gas concentration reaches 30% Lower Flammability Limit (LFL) in air. If either of the two techniques provide warning of possible leakage, investigations and repairs are required as agreed with the classification society (e.g. Lloyds Register). Although these safety regulations provide crucial information regarding leakage, they do not provide any information of the severity of damage (localized yielding) that has resulted in the leakage. The leakages not only lead to ultimate failure of the cargo tank but can also result in loss of cargo. If information regarding the severity of damage is known, appropriate maintenance can be planned to avoid loss of cargo due to leakage. Planned maintenance would also reduce shutdown cost as compared to the unplanned repairs.

Serval efforts have been made both by the industry and academia, to predict the structural response of the primary wall as a result of sloshing. For instance, J.H Kim et al [7], proposed a damage model to predict deformation in the primary wall of the cargo containment. American Bureau of Shipping (ABS) [26], provided specific experimental guideline to predict sloshing pressure on the primary wall. According to the ABS, a modelled tank containing liquid (that resembles LNG cargo tank) can be excited with irregular motion by a motion generator and sloshing impact can be recorded with pressure sensors. In accordance with the ABS guidelines, many studies have attempted to monitor sloshing pressure on the wall of the large scale cargo tank[27][28][29]. M. Graczyk et al, studied sloshing impact pressure at different filling level (92.5% and 30%) in the wall of a modelled tank [30]. A

methodology was introduced to predict the largest sloshing pressure and structural response in the wall of the cargo tank[11]. These studies were very crucial to understand sloshing response and load distribution on the primary wall. However, sloshing response of the wall does not provide any direct information of critical damage. A numerical model such as the one in ref [7], would often be required to translate the cumulative sloshing response of the wall into its structural damage. The entire process of recording the sloshing response and translating it with a numerical model into damage, would make its application as SHM extremely difficult.

Few studies have been conducted to directly predict the structural damage of LNG cargo vessel (as a result of sloshing) for SHM purpose. These studies are based on strain measurement. M.C.Oh et al [10], measured the dynamic strain of the insulation during dry drop test (free fall of weight on the insulation to mimic sloshing). Whereas, M.H.Kim et al [31], introduced a damage identification methodology for the insulation, based on strain measurement. These studies provided promising results and have the potential to be used as a SHM technique on the insulation. For SHM on the hull of the LNG vessel, a fatigue damage management methodology based on fatigue damage sensors is proposed [32]. Like the reported successful research on the insulation and hull of LNG vessel, there is no research in the literature for SHM on the primary wall of the cargo tank (to assess the severity of damage). The only research related to damage detection of the wall in LNG cargo tank is AE in-service pressurization testing[33]. This is a test procedure where the cargo tank is pressurized (to 5-10% more pressure than that experienced by the vessel in last six months) with its cargo. The pressure from the cargo facilitates the growth of damages that has already occurred during service operation. The growth of damage generates elastic waves, which are detected by AE sensors. The presence of damage in the wall is interpreted by the intensity and rate of elastic wave captured by the AE sensor. Depending upon the sensor deployment, localization of damages is also performed. Unlike online monitoring (monitoring the structural response during service operation), AE in-service pressurization is carried out during routine maintenance by a surveyor. This technique provides information only during routine maintenance regarding damages that have occurred in service operation. In order to implement a CBM strategy of the primary wall, real-time information about critical damages are required during service operation (voyage in the sea). This is only possible if SHM is carried out in real-time, and any sign of damage is provided as a warning to the operator.

The critical damages in the primary wall include the localized yielding. At present the only SHM technique that has proven to be successful in identifying the deformation and yielding in austenitic stainless steel (material of the primary barrier) is AE [34][35][36][37][38][39]. Despite the potential of AE in identifying the deformation and yielding, it has not been adopted by the industry as an SHM technique on the primary wall. The primary reason for this could be because AE monitoring is influenced by a range of user defined settings (*e.g.* Threshold and timings) on the AE data acquisition system [40]. The secondary reason could be because AE results may be affected by the noise (*e.g.* due to sloshing). This could be avoided by understanding the nature of noise in a calibration test (*i.e.* by gathering AE data from the cargo tank during a voyage and analysing the noise content). Once the nature of noise is understood, relevant filtration technique can be used to avoid noise content in the data. In order to rule out the primary reason, the influence of user defined settings on the AE monitoring has to be minimized.

### **1.3 Aim and objectives**

The aim of this research is to improve the state of the art of the AE monitoring technique, for SHM application in the primary wall of the LNG cargo tank. The objectives are to:

1. Present a new AE monitoring technique that decreases human involvement with the acquisition settings.
2. Evaluate the qualitative performance of the presented technique, with a modelled waveform that resembles a damage source.
3. Validate the effectiveness of the presented technique, respective to the damage source in the primary wall of the LNG cargo tank, in laboratory based tests on standard specimen.

### **1.4 Summary of contribution to knowledge**

This research presents a new AE monitoring technique. The new technique is based on an AE feature calculated using quadratic Renyi's entropy, which reduces the human involvement with the acquisition settings, unlike many traditional AE features. The presented AE feature proved to be efficient in providing condition monitoring indication of damages in steel (austenitic stainless steel) and has the potential to be implemented in the

commercial AE data acquisition systems for monitoring the primary wall of the LNG cargo tank.

## **1.5 Organisation of thesis**

A schematic representation of the thesis is illustrated in figure 1.6. The introduction of the thesis is followed by a literature review in chapter 2. An in-depth review on the principles, application and damage detection capability of AE (in fatigue and tensile loading) is presented in chapter 2. Drawbacks of AE that leads to the foundation of this research are also presented in this chapter.

An AE technique that reduces the human involvement with the data acquisition setting is presented in chapter 3. The procedure employed for evaluation of the presented technique is provided in this chapter. Finally, methodology for experimental validation of the presented technique, on standard specimens, during fatigue and tensile loading is also presented in this chapter.

Results of experimental evaluation for the presented technique and the validation tests performed on standard specimen during both fatigue and tensile loading are described in chapter 4. The capability of the presented technique to identify damages is also addressed in this chapter.

Chapter 5 discusses the feasibility of new technique to be implemented in monitoring the damages on primary wall of the cargo tank as a result of sloshing impact. This chapter also discusses the advantages and challenges associated with the new technique.

Contribution made and conclusion drawn from this research is provided in chapter 6. This chapter briefly describes the future work that is required to practically implement the technique.

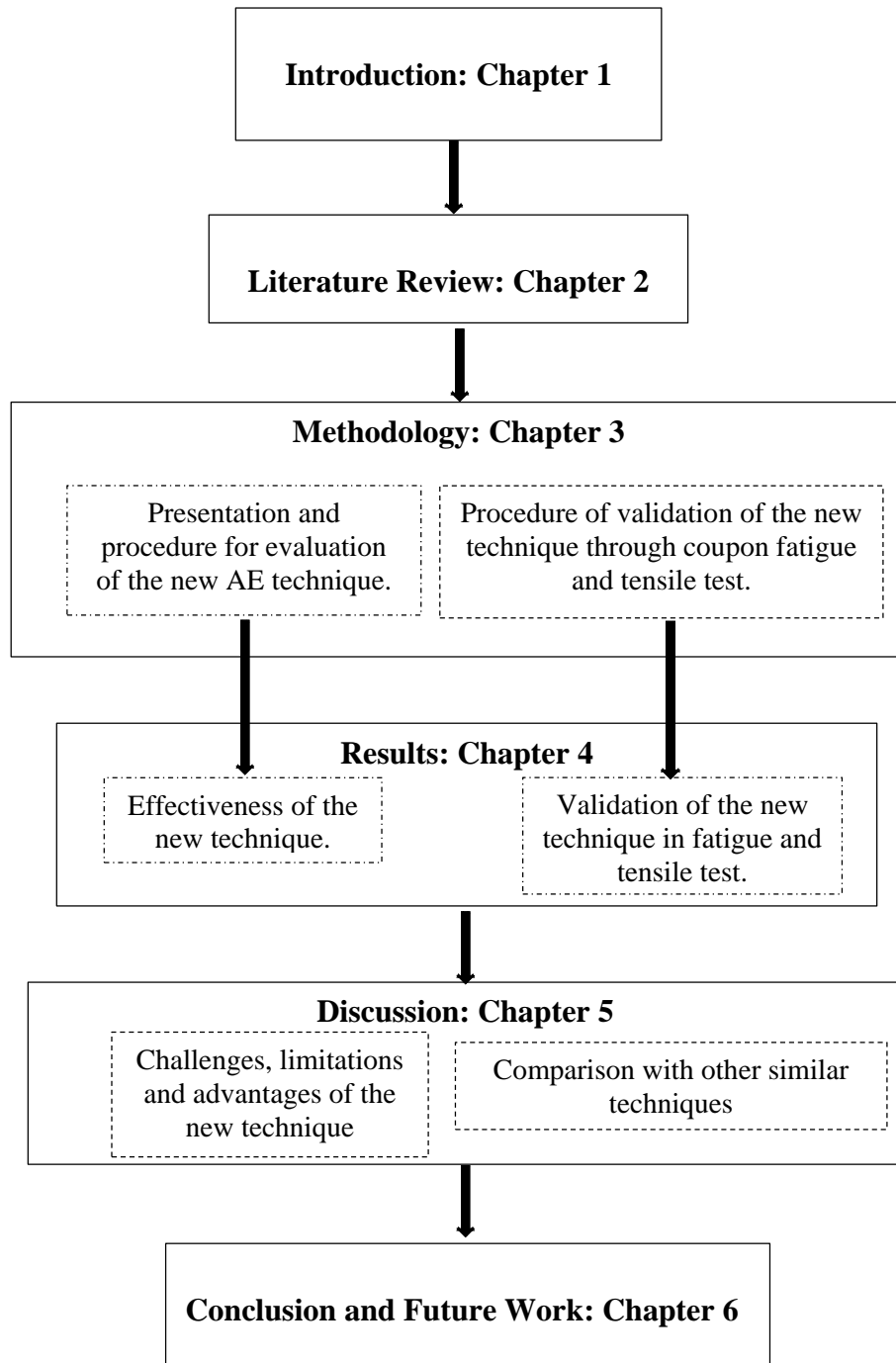


Figure 1-6: An overview of the thesis structure

## 1.6 List of publication

1. Tanvir, F., Sattar, T., Mba, D. and Edwards, G. (2018). Identification of fatigue damage evolution in 316L stainless steel using acoustic emission and digital image correlation. In: 12<sup>th</sup> international Fatigue Congress. Poitiers: MATEC Web of conference.
2. Tanvir, F., Sattar, T., Mba, D. and Edwards, G. (2018). Identification of fatigue damage evaluation using entropy of acoustic emission waveform. SN Applied Science.
3. Tanvir, F., Sattar, T., Mba, D. and Edwards, G. (2018). Validation of Acoustic Emission signal entropy as a damage identification parameter. Applied Science.

## 1.7 Chapter summary

This chapter identifies natural gas as the major contributor to the global energy needs. Natural gas is usually converted into LNG for long distance transportation through oceans, using tankship. Among the several categories of tankships available for the transportation of LNG, industry often prefer a double walled membrane type vessels, which is considered to be cheaper and requires a lot less engineering maintenance work. During voyage the primary wall of the cargo tanks in a membrane type vessel are subject to extreme sloshing impact from the LNG cargo. The sloshing impact can sometimes lead to localized yielding of the primary wall. Localized yielding in due course can lead to crack initiation, as a result, the LNG can flow out from the primary wall. A further infiltration to the secondary barrier can result in the LNG to potentially reach the hull structure causing brittle failure. A catastrophic failure introduces risk to the safety of life and property. In order to reduce the risk of catastrophic failure, a maintenance strategy has been proposed by the IMO. Despite these regulations, there have been several risk of failure as a result of sloshing impact during voyage. In order to successfully reduce the risk of failure, this research highlights the need to replace the traditional maintenance with a CBM strategy, which focuses on maintenance of the cargo tank after the initial localized yielding in the primary wall. In order to gather

## Introduction

real-time information about yielding, structural assessment of the primary wall with a suitable SHM technique is a primary solution.

There have been many efforts by the academy and industries to predict the structural response as a result of sloshing. However, a numerical method is often needed to translate the structural response into critical damage, making its application extremely difficult in SHM. Presently, the only SHM technique which has proven to be successful in identifying yielding in austenitic stainless steel (*i.e.* material of the primary barrier) is AE. Despite this potential of AE, it has never been adopted or considered by the industry as a SHM technique of the primary wall. This research addresses one of the major drawback of the state of the art AE monitoring technique and improves it so that the possibility of AE to be implement for monitoring the primary wall is increased.

## 2 Review of the Acoustic Emission technique used in Condition Monitoring

### 2.1 Fundamentals of AE

#### 2.1.1 Introduction

AE is a passive Non-Destructive Testing (NDT) technique for examining the behaviour of materials under stress [40][41]. It can be defined as a mechanism where material emits elastic waves when they fail at a microscopic level.

The elastic waves are generated in the material as a result of the change in stress state where failure occurs. This change in stress state usually takes place due to application of external forces on the material. The atoms in the region where there is a change in stress state, undergoes either a positive or a negative compression [41]. As a result, this region experiences a sudden change in density. The change in density of this region is passed on to the next region by the collective movement of atoms. The density of the first region then reverses and goes past its original value by a small amount (*e.g.* if it previously experiences a positive expansion, then it readjusts to a negative compression). The fluctuations (*e.g.* vibration) in density is passed on to the next region and through the material. The failure of the material which causes the initial fluctuation in density is the origin of elastic waves. The transfer of this fluctuation in density in the material results in the propagation of elastic waves. In other words, it can also be said that elastic waves travel in the material by the movement of interacting atoms (*e.g.* vacuum does not facilitate the movement of elastic waves as there is no interacting atoms). The fluctuation in density of a region is associated with a fluctuation in direction and magnitude of strain field. Therefore, an elastic wave can also be defined as an oscillating strain field moving through the material[42]. The fundamental equation governing the propagation of an elastic wave is shown in equation 2-1.

$$p_0 \frac{\partial^2 u}{\partial t^2} = (\lambda + 2\mu)\Delta(\Delta u) - \mu\Delta \times (\Delta \times u) \quad \text{Equation 2-1}$$

Where:

$P_0$  is the density of the material.

$u=(x,y,z,t)$  is the time dependent displacement vector.

$\lambda$  and  $\mu$  are called the Lamé constant.

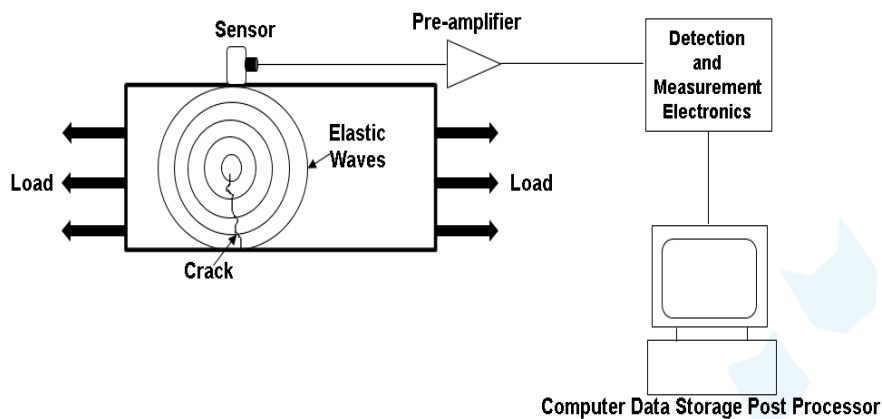


Figure 2-1: AE working principle

AE monitoring is the process of interpreting the complex elastic wave in terms of damage in a structure, component, process and machine. The origin of elastic waves is called the AE source. There are two types of AE source. In the literature they are referred to as the primary and secondary source [43]. The primary sources are generally associated with damage whereas the secondary sources are related to the friction noise. The emitted elastic waves in the material are captured as analogue signals using AE sensors. The analogue signals are fed to a data acquisition system which digitizes each signal and measures the features (*i.e.* count, energy, centroid frequency, rise-time, duration and peak amplitude). The strength of the features is representative of the nature of the AE source. The digitized waveform of the signals and their features can be stored in a computer for post processing. Figure 2-1 and 2-2 highlight the AE working principle and definitions of the features. AE monitoring has been widely used in many applications such as the identification and localization of damages in pressure vessels [44], obtaining information about leaks in pipe system and storage tanks [45], keeping track of corrosion [46], identifying in situ damages in welds [47], monitoring wind turbine blades [48] and identifying damages of protective coatings [49].

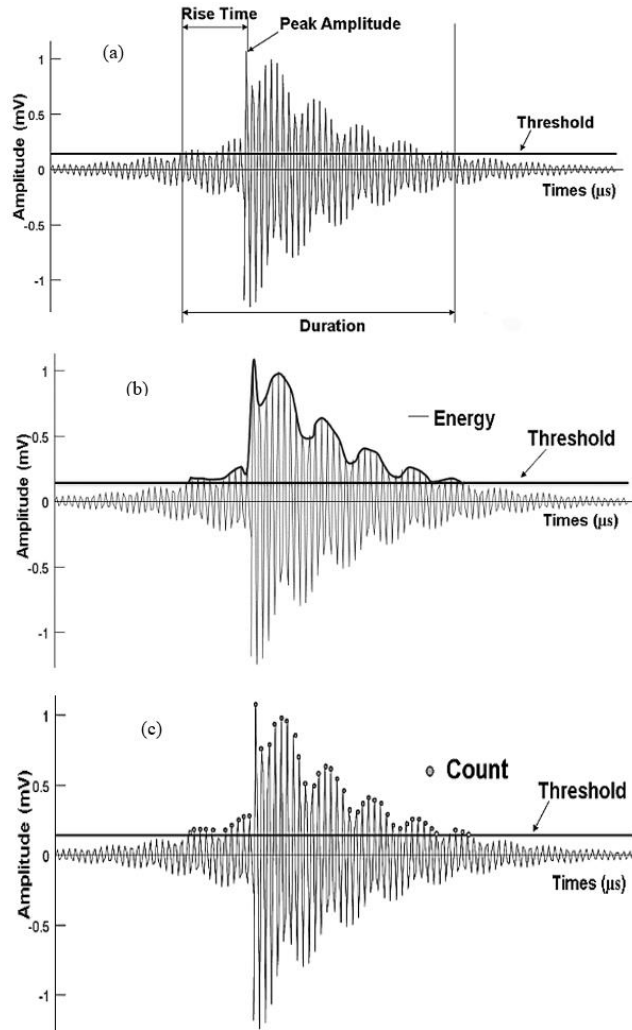


Figure 2-2: Definition of AE features: (a) Rise-time, Peak-amplitude, Duration (b) Energy (c) Count

### 2.1.2 AE source localization

AE source localization is a technique for obtaining information about the location of the AE source. In AE monitoring, elastic wave generated from an AE source can be detected on many sensors, such that each sensor captures the entire elastic wave. The principle of AE source localization is based on the Time of Arrival (TOA) of the elastic wave from the AE source to the sensor array. By comparing the TOA at the array of sensors, the location of the AE source can be extracted.

The widely used algorithms for AE source localization are called linear and planer. These algorithms are based on the following assumptions: The elastic wave velocity is constant; the material is isotropic and the wave propagation path does not have any obstacle.

### 2.1.2.1 Linear localization algorithm

The linear localization algorithm is used to locate the AE source in linear structures (e.g. pipes and narrow bars) [40][50]. In this algorithm, the 1-dimensional location (e.g. x coordinate) of the AE source is obtained using the elastic wave velocity and the difference in TOA of elastic wave between two AE sensors. The two sensors are arranged linearly and the location of the AE source of any point between these AE sensors can be obtained. The limitation of this algorithm is that it only provides 1-dimensional information about the location of the AE source, which is between the two AE sensors. The principle of the linear localization algorithm is shown in equation 2-2. Figure 2-3 illustrates some of the terms used in equation 2-2 and how it is used to extract the x-coordinate of a source along a line.

$$x = \frac{1}{2}(X - \Delta tv)$$

Equation 2-2

Where:

$X$  is the total distance between the two sensors.

$x$  is the distance of the AE source from sensor 1.

$\Delta t$  is the TOA difference between the two sensors.

$v$  is the velocity of the elastic wave.

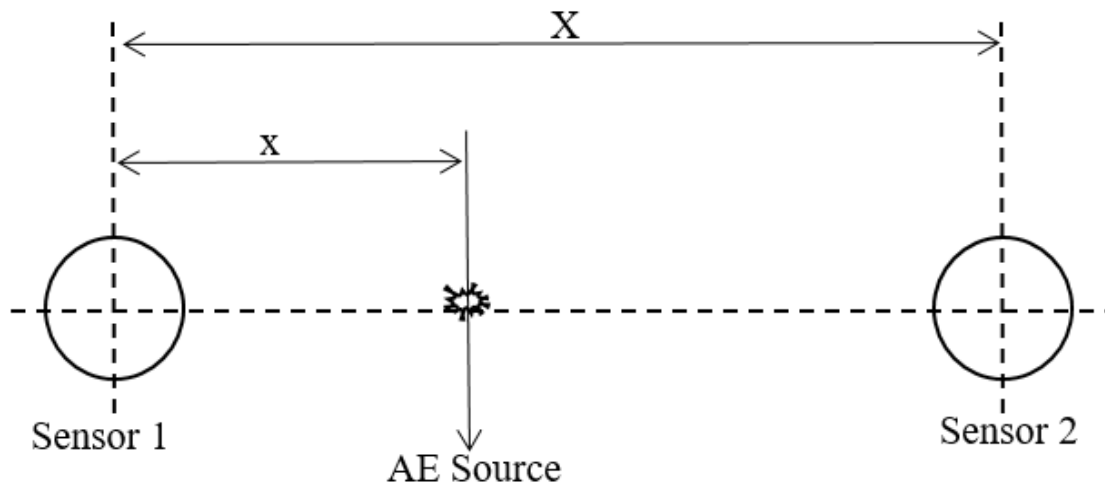


Figure 2-3: Linear localization methods

### 2.1.2.2 Planner localization algorithm

The planner localization algorithm is used to locate the AE source in 2-dimensional structures (*e.g.* a rectangular or square plate) [40][50]. This algorithm mostly uses the difference in TOA between two or three AE sensors and the elastic wave velocity to extract the 2-dimensional location (*e.g.* x and y coordinate) of the AE source. The location of the AE source can be precisely obtained when it is in between the sensor array. The limitation of this algorithm is that an AE source outside the sensor array can produce the same  $\Delta t$  as that of the one inside the sensor array. As a result, an AE source outside the sensor array can be ambiguously mapped inside the sensor array. The principle of planner localization algorithm is shown in equation 2-3, 2-4 and 2-5. Figure 2-4 shows the terms used in the equation 2-3.

Planner localization using two sensors does not provide an accurate information about the location of the AE source [51]. However, this problem can be avoided by adding another sensor to the array (*e.g.* a third sensor) and repeating the process with three sensor pairs (*e.g.* 1-2 sensor pair, 2-3 sensor pair and 1-3 sensor pair). With the three sensor pairs it is possible to generate three hyperbolae and the intersection of these hyperbolae indicates the location

$$R_2 = \frac{1}{2} \left( \frac{D^2 - \Delta t_{1,2}^2 v^2}{\Delta t_{1,2} v + D \cos \theta} \right) \quad \text{Equation 2-3}$$

$$x = R_2 \cos \theta \quad \text{Equation 2-4}$$

$$y = R_2 \sin \theta \quad \text{Equation 2-5}$$

Where:

$D$  is the distance between two sensors.

$\Delta t_{1,2}$  is the time TOA difference between the two sensors.

$R_1$  is the distance of the AE source from sensor 1.

$R_2$  is the distance of the AE source from sensor 2.

$\theta$  is the angle between  $R_2$  and  $D$ .

$v$  is the wave velocity.

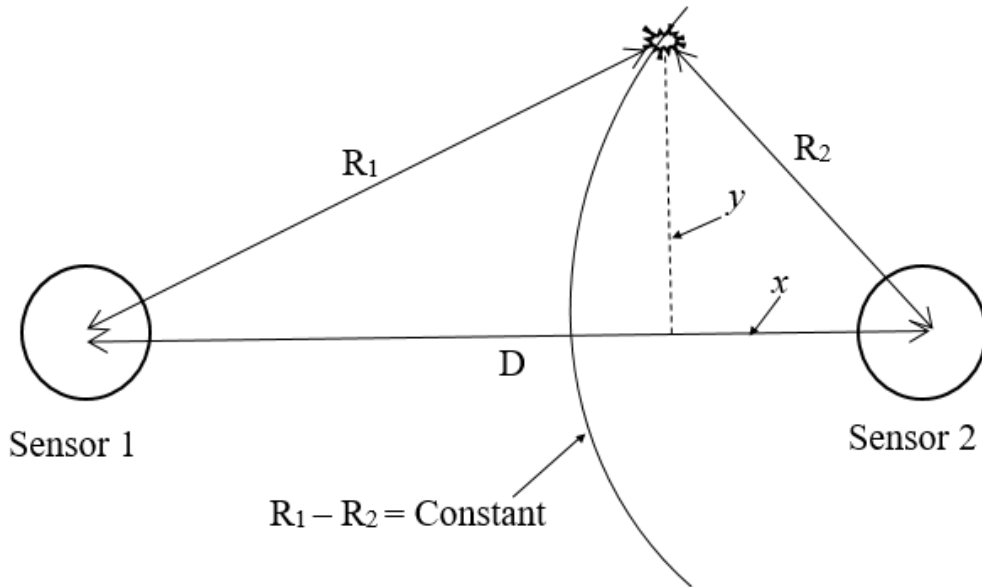


Figure 2-4: Planner localization methods with two AE sensor

of the AE source [51][52]. The principle governing planner localization algorithm using the three AE sensor is shown in equation 2-6. Figure 2-5 shows the terms used in equation 2-6 [52].

In order to improve the AE source localization technique, there have been many studies performed in the literature. For instance, Dirk Alject et al [53], introduced a new localization algorithm, using three sensors, to capture the location information of AE sources outside the sensor array. Daniel Gagor et al [54], introduced a threshold independent technique for detection of the onset (*e.g.* arrival) of an elastic wave for 1-dimensional localization. V. Salinas et al [55] improved the localization technique, by performing an iterative study where the threshold for capturing the elastic wave in each sensor was changed, until the velocity of the elastic wave in all the sensor converged. Despite the successful conclusions drawn from this research, they are yet to be implemented in commercial AE data acquisition systems.

$$x^2 + y^2 = r^2$$

$$(x - x_1)^2 + (y - y_1)^2 = (r + \delta_1)^2$$

$$(x - x_2)^2 + (y - y_2)^2 = (r + \delta_2)^2$$

Equation 2-6

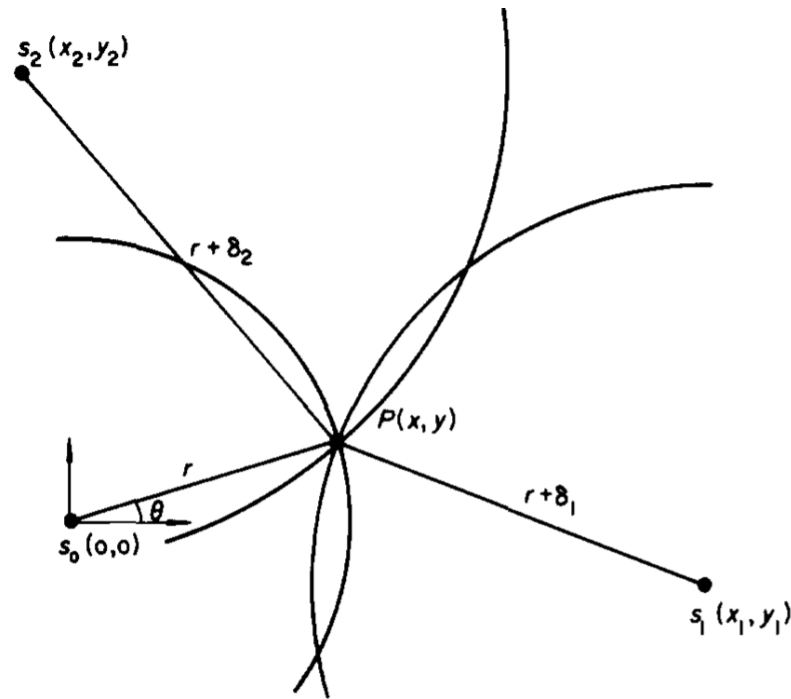


Figure 2-5: Planner localization methods using three sensors

### 2.1.3 Wave Modes

Elastic waves only travel through solid structures. Depending on the type of propagating media, they can be in the form of bulk waves, surface waves (*e.g.* Rayleigh wave) and Lamb waves.

#### 2.1.3.1 Waves in infinite media

In infinite media (*e.g.* which has a dimension significantly larger than elastic wave lengths), elastic waves propagate in the bulk of the material and are referred to as bulk waves [43]. There are two types of bulk waves, termed as longitudinal (compression) and transverse (shear) waves [43][56]. The longitudinal wave propagates as a result of the successive compression and rarefaction of the atoms in the medium. The direction of the propagation of this wave mode is parallel to the direction of the movement of the atoms in the medium. Unlike the longitudinal wave, the transverse wave propagates by the sharing motion of the atoms in the medium and the direction of the propagation of this wave is perpendicular to the movement of atoms. An illustration of the longitudinal and transverse wave mode is shown in figure 2-6 and 2-7 respectively [57]. The velocity of these wave modes are independent of the frequency, however they depend on the material properties of the propagating medium. The equations governing the velocities of longitudinal and transverse waves are shown in equation 2-7 and 2-8 respectively.

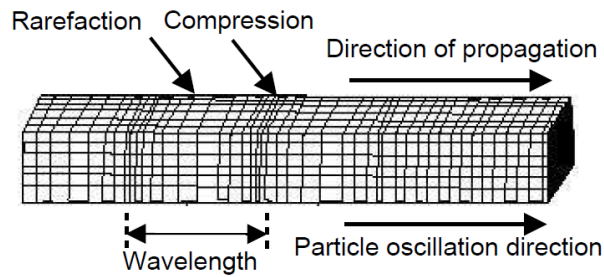


Figure 2-6: A propagating longitudinal [57]

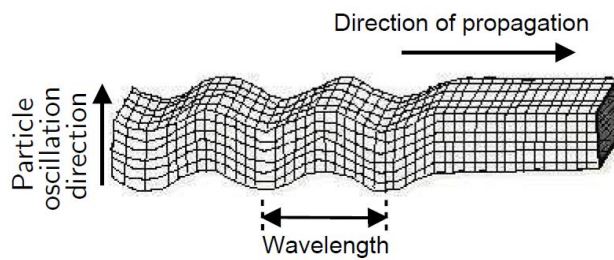


Figure 2-7: A propagating transverse wave [57]

$$C_L = \sqrt{\frac{E(1-j)}{\rho(1+j)(1-2j)}}$$

Equation 2-7

$$C_T = \sqrt{\frac{E}{2\rho(1+j)}}$$

Equation 2-8

Where:

$C_L$  represents the longitudinal wave velocity.

$C_T$  represents the transverse wave velocity.

$E$  represents the Young's Modulus of the material.

$\rho$  represents the density of the material.

$j$  represents the poisson's ratio of the material.

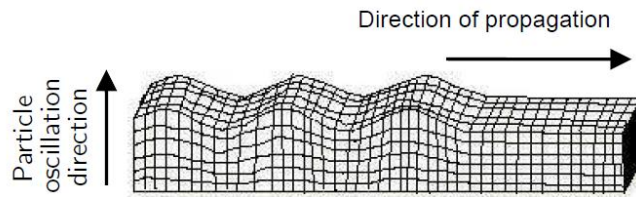


Figure 2-8: Rayleigh Wave [57]

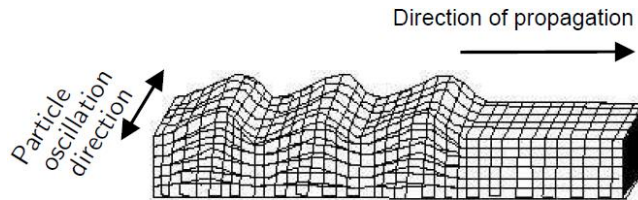


Figure 2-9: Love Wave [57]

### 2.1.3.2 Waves in semi finite media

The interaction between the atoms at the surface of a bounded solid results in another group of waves called the surface waves. The amplitude of a surface wave is maximum at the surface of a bounded solid and it decreases as the distance from the surface is reduced [41]. There are two types surface waves, they are known as the Rayleigh and Love waves. The movement of the atomic particles in Rayleigh waves are perpendicular to the plane of the surface. Whereas, in Love waves, the movement of atomic particles is in the plane of the surface. In both the waves the movement of atomic particles is perpendicular the direction of its propagation. An illustration of the Rayleigh and Love wave is shown in figure 2-8 and 2-9 respectively.

### 2.1.3.3 Waves in finite media

Waves in finite media (*e.g.* thin plates, where the wavelength of the elastic wave is similar to or in the order of the plate thickness) are referred to as Lamb waves [43][56]. There are two types of fundamental Lamb wave modes, they are commonly known as the symmetric ( $S_0$ ) and the antisymmetric ( $A_0$ ) mode. An illustration of the symmetric and antisymmetric wave modes is shown in figure 2-10 and 2-11 respectively [50]. The Lamb wave modes can be generated at every excitation frequency. When the value of excitation frequency exceeds a cut off frequency (material dependent parameter), there can exist many higher order symmetric (*e.g.*  $S_1$   $S_2$   $S_3$ ) and antisymmetric (*e.g.*  $A_1$   $A_2$   $A_3$ ) modes, which can convert into one another when they are reflected form a discontinuity [58][59]. These wave modes differ from one another by their velocity, which depend on the product of the frequency and the thickness of the propagating medium. This results in dispersion of the wave packet as it

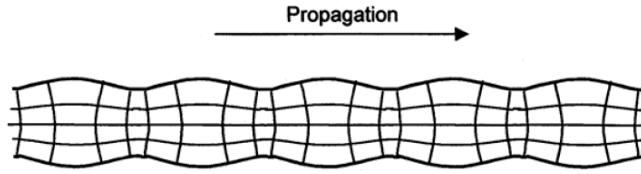


Figure 2-10: Symmetric wave mode [50].

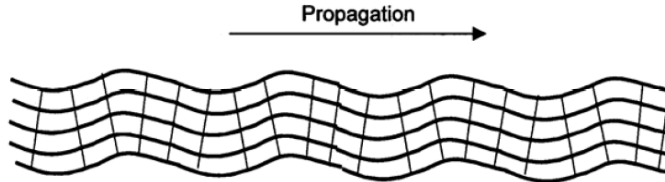


Figure 2-11: Antisymmetric wave mode [50]

travels through the medium. The speed with which the phase of the wave propagates is termed as the phase velocity, whereas the speed with which the envelop of the wave propagates is termed as the group velocity[59]. In the absence of dispersion, the group velocity of a wave mode is same as that of its phase velocity (in this case the temporal frequency is directly proportional to the spatial frequency). Real bounded solids are dispersive in nature, where the group velocity is less than phase velocity [41]. The equation governing the phase and group velocity is shown in equation 2-9 and 2-10 respectively. In the higher product of frequency and thickness, the phase velocity of the lamb wave modes converges to the surface wave velocity [58][60]. This is because with the increase in the frequency of the wave and/or thickness of the plate, the ratio of the wavelength to the plate thickness decreases, as a result the lamb wave mode is not able to reach the bottom of the plate, like the surface waves. The characteristics of Lamb wave propagation is represented in the form of dispersion curves. An illustration of the dispersion curve of aluminium (Al 202426) plate is shown in figure 2-12 and 2-13 [59].

$$v_p = \frac{\omega}{k} \quad \text{Equation 2-9}$$

$$v_g = \frac{\partial \omega}{\partial k} \quad \text{Equation 2-10}$$

Where:

$v_p$  is the phase velocity.

$v_g$  is the group velocity.

$\omega$  is the temporal frequency.

$k$  is the spatial frequency, also known as the wave number.

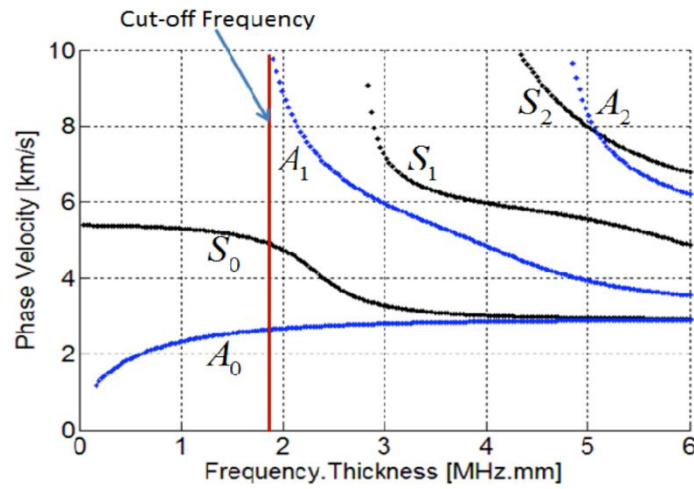


Figure 2-12: Phase velocity of Aluminium [50]

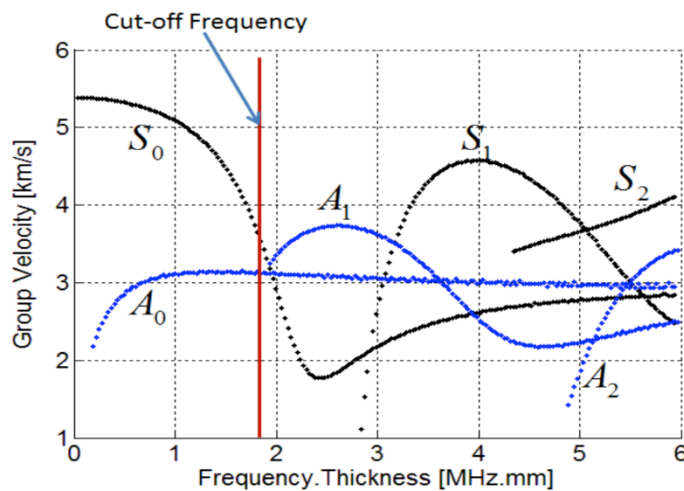


Figure 2-13: Group velocity of Aluminium [50]

### 2.1.4 Attenuation

Attenuation is the exponential decay of an elastic wave with distance travelled in a medium [41]. There are many factors responsible for attenuation, such as geometric spreading, dispersion, scattering and transmission in adjacent medium. Attenuation due to geometric spreading is caused by the distribution of the elastic wave's finite energy over a wider area with distance travelled [57]. This is because, the localized elastic wave from the source is free to travel in all the directions. Attenuation due to dispersion is as the result of decrease in the energy per unit area of the wave front. This decrease occurs due to expansion of the wave packet (as a result of different velocity of the wave trains making up the wave packet)

as it travels through the medium [57]. The decrease in amplitude of the wave front when it encounters some discontinuities in the medium is termed as scattering of the elastic waves. Dissipation of elastic waves, when it meets the interface between two surfaces can result in the decrease of its amplitude. This phenomenon is known as attenuation due to transmission of elastic waves. The transmission of elastic waves from one medium to another is maximum when there is a similar acoustic impedance between the two mediums [41].

## **2.2 Damage Monitoring with AE**

Research with AE for damage monitoring started in the 1960's [61], however there was no sharp growth in the contribution to knowledge during that time. Instead, it increased steadily with the development of electronics and computing. At the moment the commercial AE data acquisition system is able to detect AE waveforms across the entire frequency spectrum. Accumulation of the research effort from beginning until now, led to a vast literature in damage monitoring using AE. As a result, this technology is successfully implemented to monitor damages in many structures (*e.g.* civil, pressure vessel, aerospace pipe lines, etc) [62][63].

Before implementing AE to monitor damages in a structure, several factors are needed to be considered. One of these factors is the attenuation. Information regarding the attenuation is important as it influences the sensor arrangement in structures. A clear understanding about the attenuation for an optimum sensor arrangement can be obtained by performing the attenuation test as per the standard ASTM E1930/ E1930M [64]. Another factor is understanding the propagation of wave modes and their velocities in structures for a successful source localization. Information about this can be gained by generating elastic waves in the structure with a simulated AE source and capturing it with AE sensors (AE sensors with known distance from the source). Fundamentally, information about the wave modes and their velocities can be gained from the dispersion curves. Another important factor is to understand the feature of AE waveform recorded from damages in the structure. The features recorded from damages are representation of the nature of AE source. For instance, the brittle failure will generate a strong AE waveform (*e.g.* with a high energy) compared to that of the ductile failure [65]. Failure of materials is dependent on its micro-structure, as a result every material has a different failure mechanism. The only method to understand the features of the AE waveform from damages in the structure is to test the standard specimen, constructed from the same material of the structure and characterize its

failure mechanism with the AE features. Owing to this reason, the primary stage in majority of the research, where AE has been investigated to monitor structures and components, is based on simple standard specimens[57].

This research proposes and validates an alternative AE feature which has merit over the traditional ones and can be implemented to monitor the primary wall of the LNG cargo tank. The validation of the alternative AE feature is performed on the simple standard specimen. As a result, the following chapters (*e.g.* 2.2.1 and 2.2.2) provide a review of the research performed with AE on a standard specimen. These chapter provides a brief over view of what has been achieved in this field. However, to gain further understanding readers are encouraged to refer to the references.

### 2.2.1 Application of AE in Fatigue Analysis

Fatigue is the process where the damage accumulation occurs in materials due to repetitive application of the load which is less than the value that causes failure from single load application [66]. Understanding this process is considered to be very important in design of structures as the single load analysis may lead to assumption of safety, however in reality that may not exists. The fatigue process can either begin from discontinuities (*e.g.* a notch in standard specimens) or form the internal and external surface of materials (*e.g.* in the un-notched specimen) [66][67]. AE has been widely used alongside testing both for the standard notched and un-notched specimen.

Fatigue studies of notched specimen is often based on analysing the crack growth rate against the stress intensity factor  $K$  (stress state near the crack tip). A typical behaviour of the crack growth rate against stress intensity factor is shown in figure 2-14. The stable increase in the crack growth rate can be represented by equation 2-11, this is known as the Paris law [68]. When the  $K$  reaches a specific value  $K_{IC}$  a crack propagates very rapidly up to fracture.

$$\frac{da}{dN} = A\Delta k^m$$

Equation 2-11

Where:

$\frac{da}{dN}$  is the crack extension per unit cycle.

$A$  and  $m$  is material constant.

$\Delta k$  is the stress intensity factor range.

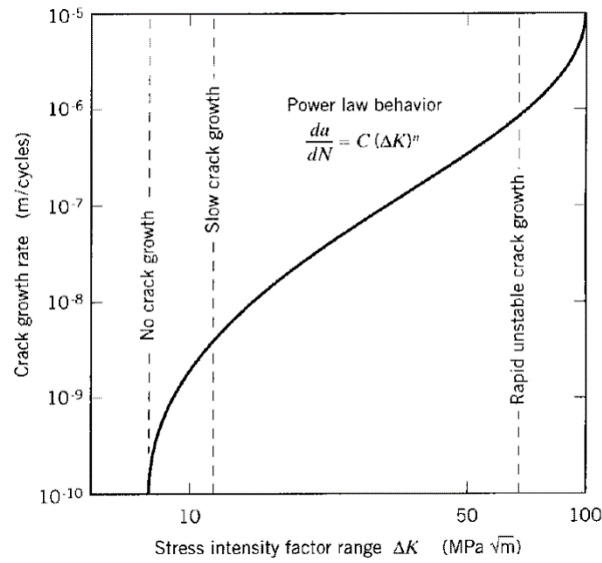


Figure 2-14: A typical plot of crack growth rate against stress intensity factor range [50]

Using the Paris law, engineers are able to estimate the crack propagation rate and the remaining life of structures subjected to fatigue loading.

Several studies were conducted to correlate the AE monitoring with stable fatigue crack propagation (linear region in figure 2-14) [69][70] [71][72][73][74]. In these studies, an equation similar to the one in 2-11 has been proposed that relates AE feature generated from the specimen (subjected to fatigue loading) to the stress intensity factor range, i.e.:

$$\frac{dn}{dN} = B\Delta k^p \tag{Equation 2-12}$$

$\frac{dn}{dN}$  is the Count per unit cycle

$B$  and  $p$  is material constant

$\Delta k$  is the stress intensity factor range

For instance, T.M Robert et al, showed a linear relationship between the AE count rate and stress intensity factor range, in the stable crack propagation region, of the standard S275JR steel and weld specimen [69]. They suggested short term AE monitoring can be used to predict the crack propagation rate and the remaining fatigue life of steel structures. In another study, they proved that it is indeed possible to predict the crack propagation rate and the remaining fatigue life through short term AE monitoring [70]. Z. Han et al [71][72], suggested that there has to be a clear understanding about the trend in AE activity from a material before equation 2-12 can be used to predict its crack propagation rate and remaining

fatigue life. Although AE activity from the stable crack propagation is mostly from the plastic zone ahead of the crack tip, the origin of few AE activities are micro structure dependent. This can result in a completely different AE trend in stable crack propagation region among materials. Figure 2-15 shows the AE count rate against crack propagation rate of weld, base and tempered (200° and 600°) specimen of Q345 steels. It is evident from this figure that for the same crack propagation rate, there is a noticeably different AE count rate for specimens. In fact, other AE features (*e.g.* Rise-time and Amplitude) from these specimens were also noticeably different during both the stable and unstable crack propagation. AE count rate in the 200° tempered specimen was significantly higher in the stable crack propagation region, this was attributed to the cleavage failure mechanism of this specimen which is considered to be a strong AE source. The 600° tempered and welded specimen produced a higher count rate than the base metal in the stable and unstable crack propagation region. This is because deboning of inclusion and precipitate with the matrix produced a higher AE activity than the base metal.

If the characteristic trend in AE feature from a material can be understood, AE can be more suitable than the linear elastic fracture mechanics approach ( $da/dN$  vs  $\Delta K$  plots) in identifying the transition from the stable to unstable crack propagation region. An illustration of the transition is shown in figure 2-16. The information regarding this transition is important as it can provide warning of catastrophic failure. It is reported in [73][74] that AE is also able to determine the transition within the stable crack propagation region in 316L stainless steel, which is not possible with the linear elastic fracture mechanics approach. This transition was attributed to the change in stress state from plain strain to plain stress.

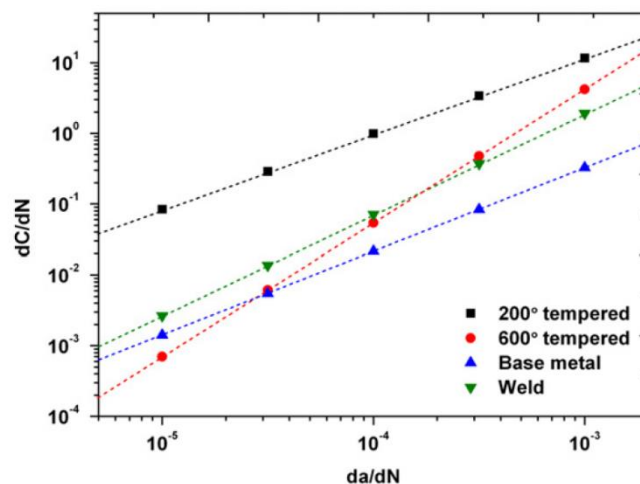


Figure 2-15: AE count rate against the crack propagation rate of different specimen [72]

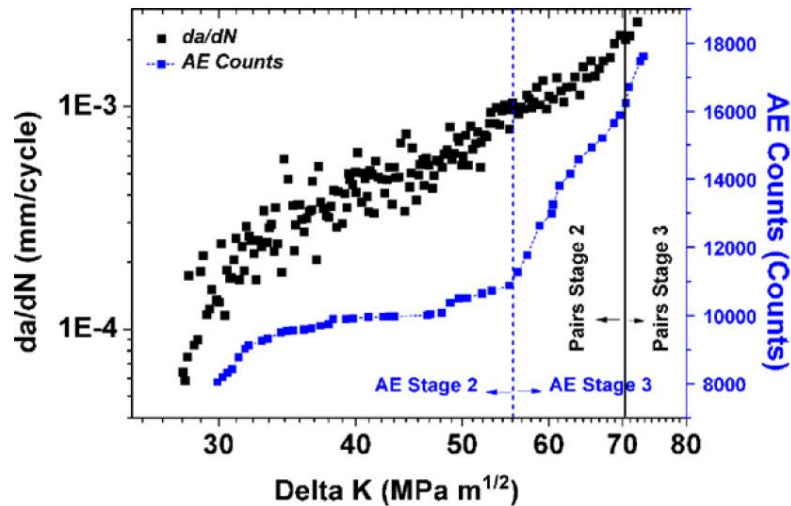


Figure 2-16: A comparison between AE and linear elastic fracture mechanics transition [71]

Fatigue studies on the un-notched specimens of a material is mostly represented by an S-N curve [66]. The S-N curve is a plot of the constant cyclic stress amplitude subjected to a specimen against the number of cycle it takes for failure. An illustration of the S-N curve is shown in figure 2-17. The S-N curve of some materials eventually flattens out, the stress amplitude at this point is termed as the endurance limit of a material. At stress amplitudes below the endurance limit, the failure of the material does not occur regardless of the number of cycles it is subjected to. Some materials do not pose a well-defined endurance limit, in these case a fatigue strength at a certain number of cycles is specified [75]. Failure of specimens below  $10^4$  cycle of loading is termed as low cycle fatigue whereas between  $10^4$  to  $10^7$  cycles is termed as high cycle fatigue [67].

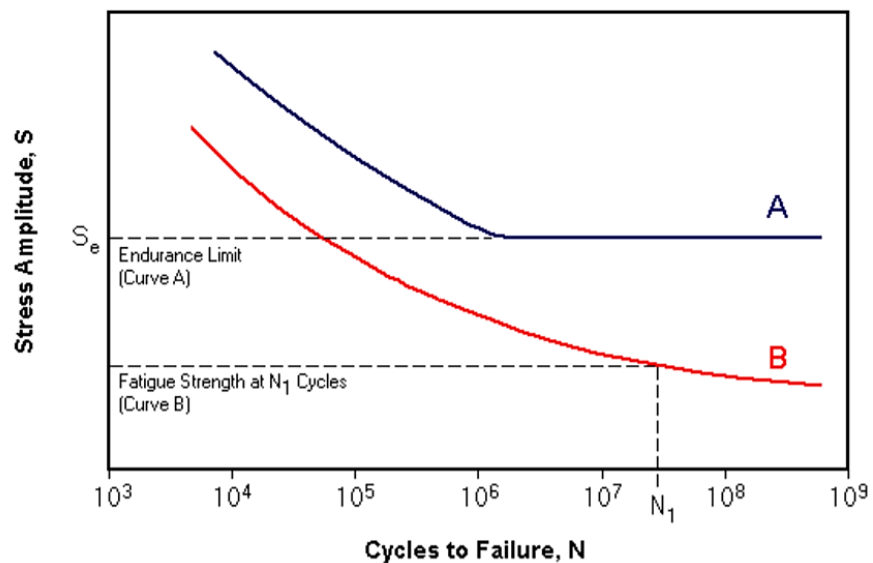


Figure 2-17: An illustration of the S-N curve [75]

AE monitoring is able to recognise three damage stages of an un-notched specimen subjected to fatigue loading [76][77][78]. The first stage corresponds to the initial loading, AE events in this stage increase with the load of the first cycle as a result of dislocation movement and multiplication. The number and strength of AE activity in this stage depends on the rate and magnitude of the load in the first cycle. The low cycle fatigue causes higher number and strength of AE activity compared to high cycle fatigue (at the same loading rate) in this stage due to higher stress amplitude. Following the first cycle there can be a slight increase in AE activity up to 20% of the fatigue life. This can be regarded to the increase in strain amplitude as a result of cyclic softening. The second stage corresponds to the crack nucleation stage. In a majority of this stage AE activity is very low due to dynamic balance between dislocation multiplication and annihilation. At the end of this stage AE activity is noticeably high due to creation and coalescence micro voids. The final stage represents the crack propagation and ultimate fracture of the specimen. AE activity of this stage is largest. Some of the main AE sources in these stages are plastic zone ahead of crack tip, de-cohesion or fracture of inclusion and crack propagation. The end of this stage is associated with the fracture of the specimen, which produces AE events with significantly higher strength.

Fatigue analysis of the un-notched specimen has been mostly based on the cumulative analysis of the AE feature. It has been shown by A.O. Amer et al [77], that the cumulative energy of AE events in austenitic stainless steel increases significantly in the third stage of fatigue. They proved that the significantly higher AE activity in the third stage resembled a burst type waveform generated due to crack propagation. An illustration of the trend in cumulative energy against the number of cycle in their studies is shown in figure 2-18.

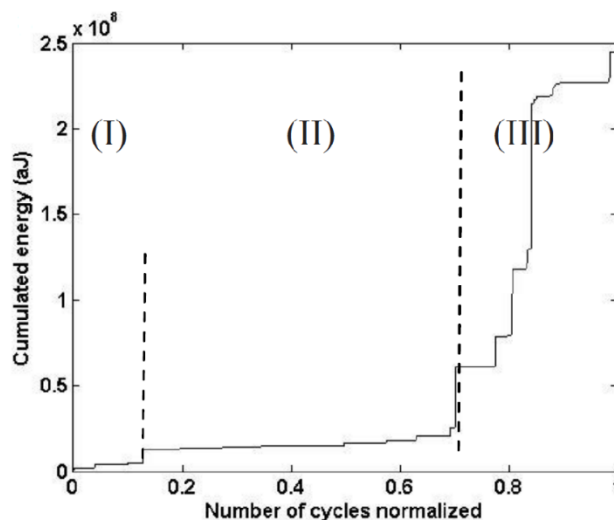


Figure 2-18: Cumulative energy against the number of cycles generated from fatigue of un-notched austenitic stainless steel [78].

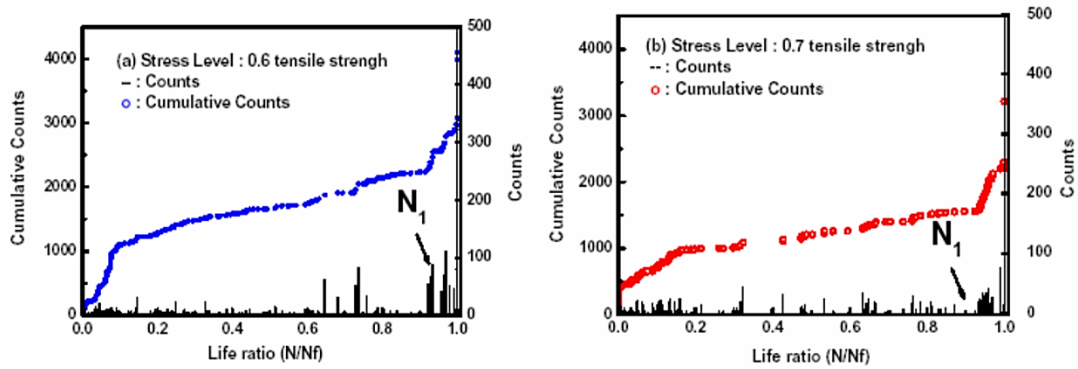


Figure 2-19: Cumulative count against the number of cycles generated from fatigue of un-notched austenitic stainless steel [79]

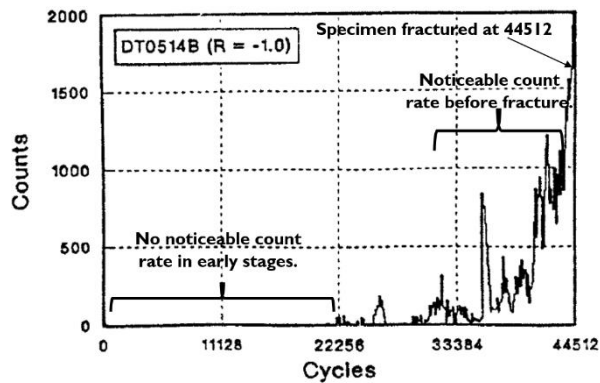


Figure 2-20: Count rate against the number of cycles generated from fatigue of un-notched Incoloy 901 [77]

K. H. Han et al [78], showed that the rate (e.g. count/time) and cumulative count both increased near the fracture period (e.g. the third stage of fatigue) of un-notched specimen, constructed from austenitic stainless steel. The crack initiation in their study was accompanied by a significantly higher count rate, indicated by  $N_1$  in figure 2-19. D. Fang et al [76][79] showed that the count rate (e.g. count/cycle) increased noticeably near the fracture period of Incoloy 901. An illustration of the trend in count rate against the number of cycle, for one of the specimen in their studies (subjected to stress range of 860 MPa and loading ratio of -1) is shown in figure 2-20.

### 2.2.2 Application of AE in Tensile Analysis

Tensile testing is the process where a tensile load is applied to the specimen until it fractures [80]. During this test, the tensile load and its corresponding elongation until fracture is recorded, from which the engineering stress and strain is calculated by equation 2-13 and 2-14 respectively. Finally, the material properties are extracted from the plot of engineering stress and strain. Figure 2-21 shows a typical stress strain curve and the material properties for a ductile material. Where the yield strength is the stress at which plastic deformation begins, this phenomenon is referred to as yielding, the tensile strength is the maximum stress

the specimen can support from the onset of loading until fracture and the stress at fracture is referred to as the fracture strength. The material property provides information to engineers about how the material behaves under the application of tensile load.

$$\delta = \frac{P}{A} \tag{Equation 2-13}$$

Where:

$\delta$  is the engineering stress

$P$  is the load

$A$  is the cross section of the specimen

$$\varepsilon = \frac{L_e - L}{L} \tag{Equation 2-14}$$

Where:

$\varepsilon$  is the engineering strain

$L_e$  is the length of the specimen after elongation

$L$  is the original length of the specimen

It has been shown in [34][37][81][82][83] [84][85][86][87][88] that AE is effective in identifying yielding and fracture during tensile deformation of standard specimens constructed from many materials. An illustration of the most recent reported trend in AE activity during the tensile deformation of austenitic stainless steel is shown in figure 2-22 [34]. According to this trend, significant amount of AE activity is generated up to approximately 0.2 strain, which is in the region before, during and just after yielding. As the strain increased beyond 0.2, no noticeable AE activity was observed until fracture of the specimen at 0.7 strain. At fracture, significant amount of AE activity is observed.

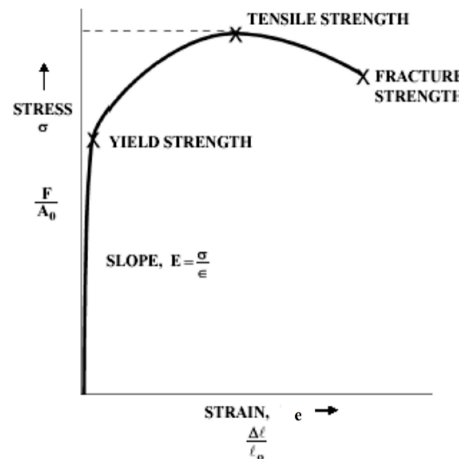


Figure 2-21: Typical stress strain curve for a ductile material [82]

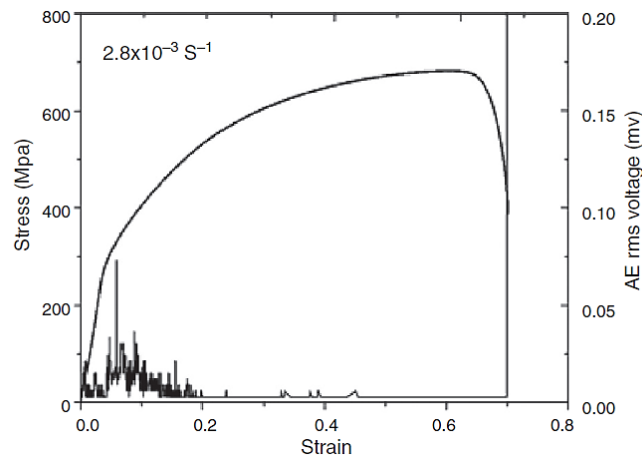


Figure 2-22: Trend in AE activity during tensile deformation of austenitic stainless steel [82]

One of the earliest pioneering work with AE and austenitic stainless was performed by Moorthy et al [81]. They showed that the peak in AE count rate occurred before the onset of macro yielding and attributed this phenomenon to the dislocation generation from the Frank-Reed source (*i.e.* dislocation multiplication by a process in which a dislocation segment within a slip plane forms dislocation loops as a result of a critical shear stress). Since then many studies have been performed in this field. For instance, AE count during and after yielding has been well understood for both nuclear and commercial grade austenitic stainless steel [82][83][84]. These studies suggest that significant increase in AE count during yielding of nuclear grade austenitic stainless steel is due to dislocation activity. Whereas, in commercial grade austenitic stainless steel, major source of high AE count during yielding is inclusion de-cohesion. Higher AE count is generated during yielding of notched specimen (compared to un-notched specimen) made from nuclear grade austenitic stainless steel, due to the increase in dislocation movement from the plastic zone [82][83]. Exactly the opposite behaviour was observed in the specimen made from commercial grade austenitic stainless steel, due to reduction of the material in the notch [82]. AE (Root Mean Square) RMS voltage and count, during yielding and fracture was observed to increase with notch depth in nuclear grade austenitic stainless steel. The increase was as a result of growth in the plastic zone size during yielding and failure by crack propagation at fracture [83][84]. With the increase in pre-strain, AE count during yielding in austenitic stainless steel was shown to decrease [85]. The reduction was as a result of reduced martensite transformation. AE RMS voltage and count during yielding of austenitic stainless steel depends on the level of work hardening [86]. Slight increase of the cold work (*i.e.* the process of adding strength to a metal by changing its shape without any heat treatment) increases the AE activity. Whereas,

increasing the cold work beyond 20% decreases the AE activity significantly. AE RMS voltage and count, during yielding in austenitic stainless steel has been shown to increase with strain rate [37]. This observation was explained as a result of increase in source activation. AE peak amplitude and count, at low temperature (223K) during yielding of austenitic stainless steel increased significantly, as a result of increase in martensite formation [87]. AE count has also been successful at determining the onset of yielding whereas Risetime and duration was able to distinguish between the different damage mechanism modes in austenitic stainless steel at supercritical water environment (550°C and 250bar) [88].

Apart from austenitic stainless steel, AE has been shown to be sensitive to tensile deformation in many other materials, such as C-Mn steel [89], Aluminium [90] and  $\alpha$ -brass [91] among others.

### **2.2.3 Low Temperature AE**

AE has also been used extensively in the low temperatures (*i.e.* upto -296 °C) to identify damages, in a range of materials such as metals, concrete and composites. For instance, I. Palmer [92], studied the effect of low temperature (*i.e.* 153°K and 208°K) on the yielding of C/Mn pressure vessel steel. A typical trend obtained in his study is shown in figure 2-23. The specimen deformed at 153°K showed very brittle behaviour and there was a little rise in emission rate prior to failure. The observed trend in AE activity was due to a small amount of yielding in the material. The test conducted at 208°K showed a monotonic increase in the AE rate similar to the one observed at room temperature. However, the failure of the specimens both at 153°K and 208°K were accompanied by high amplitude signals compared to the room temperature. V. Smirnov et al [93], showed that it is possible to use AE in a fracture toughness test of titanium alloy, at cryogenic temperature (*i.e.* 77 °K). In fact, they showed that AE identifies the onset of fracture much earlier than that of the traditional technique. As a result, the fracture toughness recorded by the AE was always lower in all their test. Fracture toughness recorded by AE and the traditional technique in their study is shown in figure 2-24. The same conclusion was drawn by Y. Shindo et al [94], for the fracture toughness of GFRP woven laminate at cryogenic temperature. In order to determine the physical properties of concrete at cryogenic temperature, R. Kogbara et al [95], investigated the changes in its micro-structure with different aggregate type, using AE, due

to cryogenic freezing. AE proved to be a useful tool in their study to understand the development of micro-crack. Figure 2-25 shows the effect of cryogenic freezing on the cumulative AE energy. There was a very little rise in the cumulative energy as a result of cryogenic freezing, in the case of limestone and trap rock mix. On the other hand, the lightweight and sandstone mixture showed distinct rise in the cumulative energy towards the end of cryogenic freezing. The observed increase in the cumulative energy was as a result of the micro-crack formation, the presence of which was validated by increase in water and chloride permeability of the mixtures.

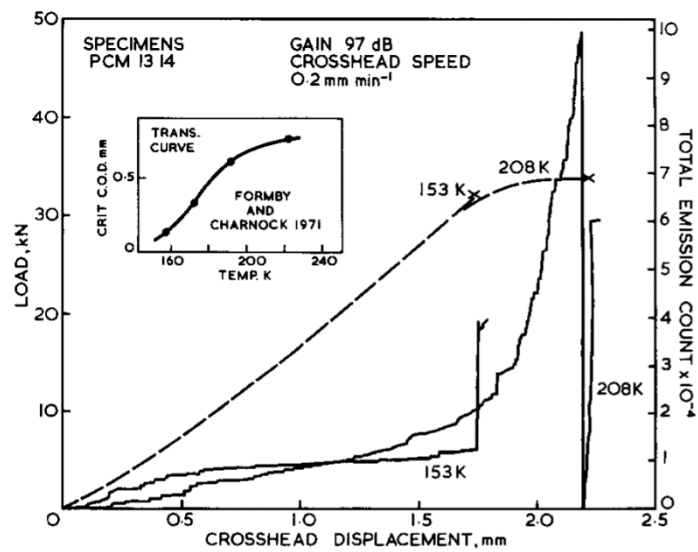


Figure 2-23: AE activity and load for specimen strained at low temperature

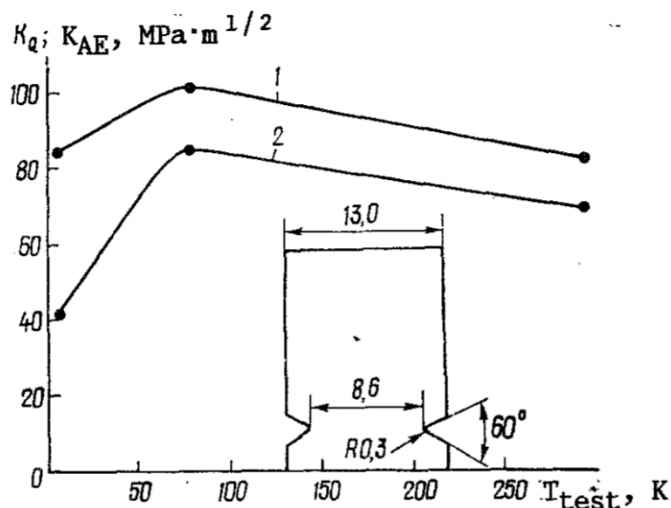


Figure 2-24: Relationship of fracture toughness with temperature recorded with: (1) GOST 25.506-85 and (2) AE

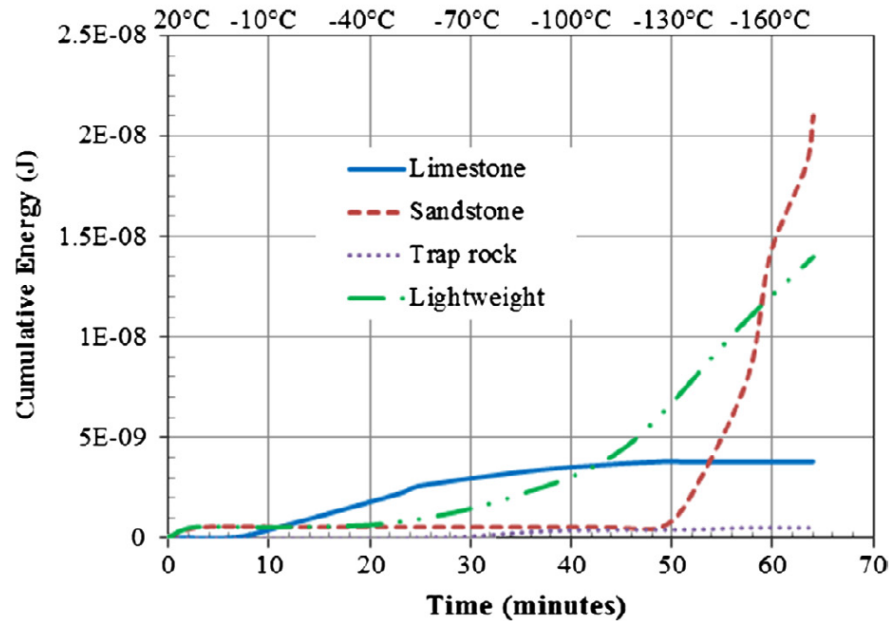


Figure 2-25: Cumulative energy released by concrete mixtures due to cryogenic cooling

#### 2.2.4 Noise Filtration using AE

During AE monitoring of standard sample, several unwanted signals originating from loading train mask the useful signal and make the interpretation of the results difficult. This often happens in specimen subjected to fatigue loading. Therefore, data filtration is an important step in AE monitoring. Several AE filtration techniques have been proposed in the literature during fatigue tests. It has been suggested in [69][70][96] that signals originating near the maximum of the load cycle are from material damage, therefore signals in the lower load range are considered to be noise and hence filtered out. J.A Pascoe et al [97], suggested damage in the material occurs neither at maximum load nor at minimum load in a cycle, but occurs in a segment of the cycle which is above certain load threshold value. The load threshold value depends on the load history and test frequency, it is not a material constant. Therefore, effectiveness of the peak load filtration technique remains questionable. Work performed in [98], used two filtration techniques. Firstly, a frequency filter eliminated all the transient signals of frequencies below 25 kHz from the data set. Secondly, a count filter eliminated all the transient signals with counts of less than 10. Although these filtration techniques were highly effective, some noisy long duration (10ms) signals remained in the data set, which were manually removed. The work performed in [71][73][99], used localization filtration technique to filter out unwanted signals and ensured the signals were received only from the area of interest. This filtration technique was very efficient in

removing the unwanted signals from the data set as a clear trend in AE activity that reflects the damage mechanism was obtained.

### **2.3 Drawback of traditional Acoustic Emission Monitoring**

Representation and classification of AE a waveform, generated from different damage modes, in terms of AE features is the most important factor and has been the basis of AE monitoring. Despite the reported success of AE, damage representation and classification is still challenging because the current method of analysis in AE monitoring is based on traditional AE features and many of them depend on the user defined acquisition settings. AE features calculated due to inaccurate user defined acquisition settings will be misleading. This can make the damage detection and classification difficult.

In order to represent and classify AE features with respect to the damage modes, an accurate information from the waveform should be extracted and the feature extraction process has to be unambiguous. A compromise in the process can mask important information in the waveform, arising from critical damage. To extract an accurate information of the waveform, the components influencing the process has to be eliminated. Currently, the primary components influencing the process are the Hit Definition Time (HDT) and threshold, which are commonly known as the acquisition settings. Acquisition settings are user defined parameters, which has to be manually set in the AE data acquisition system every time it is used in SHM. As a result, the extraction of the AE features depends on the human involvement with the data acquisition system. The following two bullet points provide a brief description of the primary acquisition settings.

- HDT has been adopted in the feature extraction process to separate the first sub waveform within a large waveform. During this process, features are extracted only from the first sub waveform and the later part of the waveform is discarded. If information regarding damages are contained in the later part of the waveform, it may be completely lost during this feature extraction process. HDT can also influence the length of the first sub waveform. Therefore, the same waveform sampled with a range of different HDT can result in different extracted feature. There is no method in the literature to theoretical estimate a suitable HDT. Most widely used values for HDT in the literature are from 50 to 400 $\mu$ s.

- Threshold is the cut-off amplitude set in the AE data acquisition system. It is an important parameter to minimize background noise during AE monitoring and also plays a significant part in the feature extraction process. If the AE data acquisition system detects at least one of the peak or trough of the signal (i.e. amplified signal from the sensor) which crosses the threshold, it begins to record the signal as a waveform from the onset of threshold crossing until certain duration. The recorded waveform includes the peaks and troughs which are both within and outside the threshold. However, features are extracted only from part of the waveform above the threshold. Therefore, the same waveform can have a range of features if it is acquired with a range of threshold (as different threshold can result in different amount of waveform above them).

There have been few studies that focus on minimising the influence of the primary acquisition settings for the feature extraction process [54][74][100][101]. For instance, a threshold independent technique to trigger an AE waveform (*i.e.* detect the onset of an AE waveform) has been introduced in [54]. Whereas in [74][100][101] an alternative AE feature is presented that is independent of the primary acquisition settings. Although the new techniques in these studies produced satisfactory result, they haven't been implemented in the commercial AE data acquisition system. This suggests that a further research is required to present an AE feature that not only excludes the human judgement for extracting it but also focuses on improving the alternative AE features presented in [74][100][101].

## **2.4 Chapter summary**

This chapter begins by highlighting the fundamentals of AE monitoring technology, where a detail explanation on the state of the art working principle, damage localization, wave mode and attenuation of AE are presented. The working principle of AE includes explanation about the source and the methods of interpretation of the elastic wave, which is considered to be a foundation of AE monitoring. The damage localization using AE includes a detailed discussion about different localization algorithm used in AE monitoring along with their advantages and disadvantages. For the elastic wave modes, the fundamentals of the propagation of different elastic waves, including their illustration is presented. The attenuation discusses the factors influencing decay and types of elastic waves.

The second part of the chapter highlights the damage monitoring using AE. This chapter identifies three main areas which are need to be explore before AE can be implemented to monitor damages in a structure. One of the factor is understanding the features of AE waveforms generated from damages in the material of the structure. This can only be achieved if standard specimen constructed from the material of the structure is tested (*i.e.* loaded to introduce failure/damages) and the damage mechanism is characterized with AE features. This part of the chapter also discusses the reported studies of the correlation of AE with standard specimen subjected to fatigue and tensile loading. The reported methods of the filtration of unwanted AE events are also presented in this part of the chapter.

The third part of the chapter address one of the major drawback of the current method of analysis in AE monitoring. This drawback of AE is due to its feature extraction process which heavily depend of the acquisition settings (*i.e.* threshold and HDT). AE features are strongly related to the damage sources and if calculated due to inaccurate user defined acquisition settings, it can result in inaccurately classified damage sources. This part of the chapter identifies the need for an AE feature, that reduces the human involvement with the acquisition settings, in measuring the feature of the waveform.

## 3 Methodology

### 3.1 First step of proposing a new AE feature

#### 3.1.1 Exploration of independent waveform feature

An accurate and reliable information (feature) from the waveform can be extracted, by reducing the influence of acquisition settings on the feature extraction process. The two primary parameters that affect the feature extraction process are HDT and threshold.

An AE waveform is made up of discrete voltage values. The number of discrete voltage values in a waveform depends on its page length and sampling frequency. The theoretical frequency in a AE waveform generated from yielding in austenitic stainless steel is 133kHz, whereas the experimentally recorded value is 190 to 270kHz at strain rate  $1.4 \times 10^{-3}$  and  $1.4 \times 10^{-2}$  respectively [34][39]. The crack initiation and propagation was reported to have a frequency response between 120 and 130kHz respectively for strain rate  $1.4 \times 10^{-3}$  and  $1.4 \times 10^{-2}$  [34]. Therefore, a sampling frequency of 5MHZ should provide a sufficient resolution in the AE waveform captured both during yielding and cracking. There are two type of page length settings: Duration Adopted Page Length Settings (DAPLS) and Fixed Page Length Settings (FPLS). In both type of page length settings, traditional AE features of the waveform are calculated from the start of the waveform until HDT has expired. In DAPLS, the page length for the waveform varies depending on the HDT and threshold. Whereas in FPLS, the page length for the waveform are fixed (*e.g.* 2500  $\mu$ s). Since, the number of discrete voltage values in the waveform depends on the page length, in FPLS it should be constant for all the recorded waveform. Hence, in FPLS, discrete voltage values of the waveform should also contain components which are well below the threshold and outside HDT. In other words, provided a FPLS is used, the number of discrete voltage values in a waveform is independent of HDT and threshold. In order to investigate this concept, an AE waveform that resembles crack initiation was analysed. The AE waveform for this

## Methodology

analysis was generated through Pencil Lead Break (PLB) tests [102]. In this test, a lead of a pencil consisting of 0.5mm in diameter and 3mm in length, was broken by pressing it on an austenitic stainless plate (120 in length, 12m in width and 5mm in thickness). The fracture of the pencil lead generated intense elastic wave on the metal plate. The frequency response of this elastic wave was not known prior to the experiment. A Vallen-VS900 AE sensor, placed 400mm away from the pencil lead break, captured the elastic wave as an analogue signal. This sensor was chosen as it was sensitive to a wide range of frequency and can successfully capture the true nature of the elastic wave. Figure 3-1 shows the sensor and its frequency sensitivity spectrum. The analogue signal from the sensor was then passed to an ASMY-6 (16 channel AE data acquisition system). Figure 3-2 shows an image of the ASMY-6 system used for this test. Table 1 shows the acquisition settings used in ASMY-6.

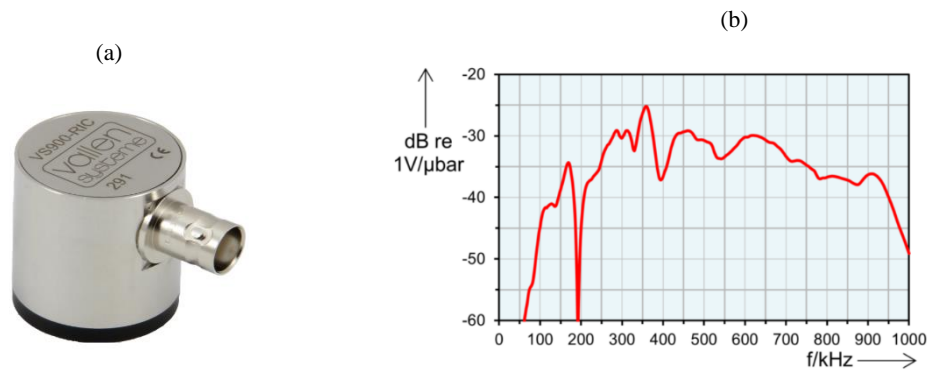


Figure 3-1: (a) VS-900 AE sensor (b) Frequency sensitivity spectrum of the sensor

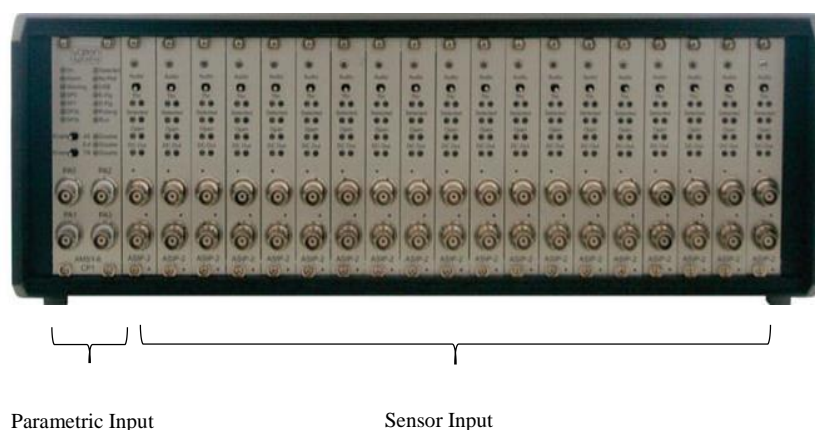


Figure 3-2: ASMY-6 AE data acquisition system

## Methodology

Table 1: Acquisition Settings for PLB Tests

Hit Definition Time (HDT)	80 $\mu$ s
Re-Arm Time	1ms
Sampling Frequency	5MHz
Max duration TR page length	820 $\mu$ s
Frequency Filter	95kHz – 850kHz
Threshold	60dB

Page length of the waveform generated from yielding in austenitic stainless steel is approximately 2600 $\mu$ s under HDT of 400 $\mu$ s[77]. This experiment was conducted under FPLS of 820 $\mu$ s. Damages in the primary wall occurs during the risetime of a typical sloshing load. Therefore, page length of the waveform equal to the risetime should be sufficient in capturing the waveforms from damages, initiated due to sloshing. In this investigation a small value of FPLS was chosen as it is comparable to the risetime of a typical sloshing load. A small FPLS also allows a closer investigation of the effect of threshold and HDT in calculating the feature of the waveform. A threshold of 60dB was chosen because it is often higher than the external noise, during online AE monitoring in a real environment. A range of HDT values from 50 $\mu$ s to 400 $\mu$ s is used in the literature [77][103][98]. In this test, a small value of HDT (*e.g.* 80 $\mu$ s) was chosen due to limited size of FPLS.

The analogue signal from the sensor was stored as a digitised waveform in AMSY-6 for post analysis. Figure 3-3 and 3-4 show the experimental setup and the waveform generated from PLB respectively. It can be observed in figure 3-4 that the waveform contains parts which are well below the threshold and outside HDT. Hence, the spreadsheet of discrete voltage value from this waveform must also contain components which are well below the threshold and outside HDT. In FPLS, the page length of the waveform is predefined and remains fixed for all the captured waveform. In other words, in a FPLS, the page length of the waveform does not vary with the HDT, unlike the DAPLS. Therefore, it can be concluded that if FPLS is used the discrete voltage values in a waveform are not dependent on the HDT and threshold. This led to the idea that if a feature can be extracted from the discrete voltage values, it will be independent of HDT and threshold, provided a FPLS is used. Discrete voltage values are representation of the size of the waveform. Therefore, the size of the waveform is also independent of HDT and threshold. The Size of the waveform is the amount of space its discrete voltage values take for storage in a hard-disk. The size of the waveform

## Methodology

was initially considered as an alternative and independent feature to AE analysis. This idea was not taken forward, because it is not able to distinguish a uniqueness of the waveform with respect to the other, despite being independent of HDT and threshold.

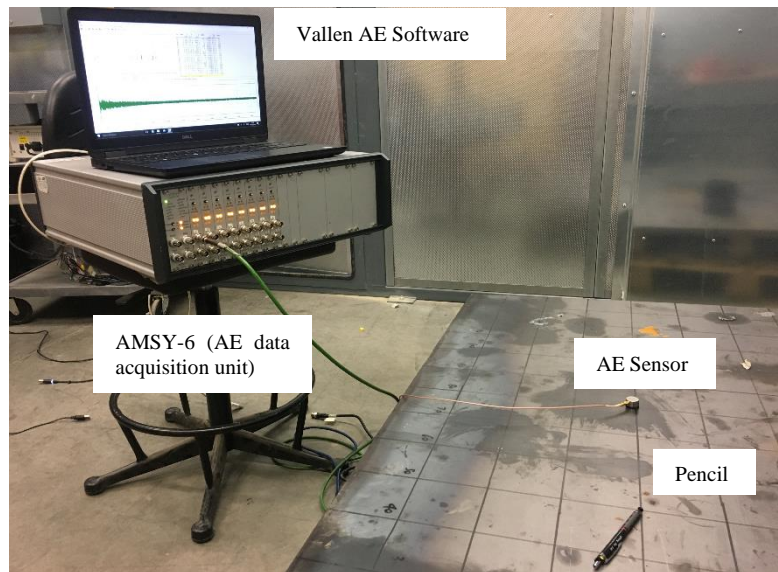


Figure 3-3: Experimental Setup : Pencil Lead Break test - Exploration of alternative feature

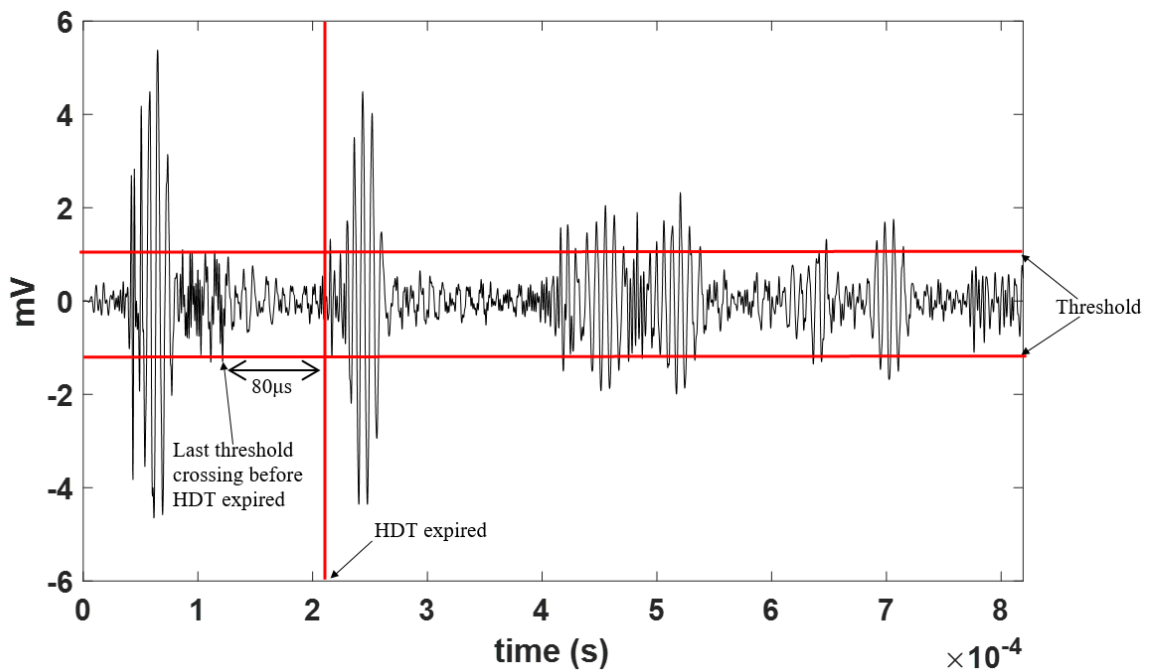


Figure 3-4: Waveform generated from PLB

The uniqueness of a waveform with respect to the other can be distinguished by comparing the disorderness in its discrete voltage values. In the theory of communication, the measure of disorderness in the discrete voltage values of the waveform is termed as its Information. A feature that quantifies the amount of disorderness in the discrete voltage values, can be

employed to extract meaningful representation about the waveform and will also be independent of HDT and threshold (since it is directly derived from the discrete voltage values). If this feature can provide valuable indication of damages in austenitic stainless steel, it has the potential to be implemented in commercial AE data acquisition system, for monitoring the primary wall of the LNG cargo tank. In order to investigate the effectiveness of the proposed idea, a detailed evaluation and validation was carried out in this research.

### 3.1.2 Disorderliness of the waveform as a new feature

In physics and mathematics, the term used for the measure of disorderliness in the waveform is Information or Entropy [104]. Several attempts have been made in the past to successfully measure the disorderliness in a waveform. Hartley [105], proposed a mathematical model to calculate the total disorderliness in a waveform, which was later known as max entropy. Shannon [106], extended Hartley's theory by introducing a weighting function in the calculation, which is recognized as Shannon's entropy. Alfred Renyi [107], pointed out that Shannon's entropy restricts the additivity of independent event in a waveform to the first (linear) functional class and there exists a second functional class that could also be used. He developed a continuous family of methods to measure the disorderliness in a waveform, by introducing a second (exponential) functional class in the additivity of events, contained in the waveform. This computation was regarded as a flexible form of disorderliness measure [104] and was later known as Renyi's entropy. Renyi's entropy of a waveform having a discrete voltage distribution  $\{x_1, x_2, x_3, \dots, x_n\}$  can be calculated using equation 3-1 as:

$$H_a(x) = \frac{1}{1-a} \log \left( \sum_{k=1}^m (P(x_k))^a \right) \quad \text{Equation 3-1}$$

1

$P(x_k)$  in equation 3-1 is the discrete probability distribution of the discrete voltage values, with  $K^{\text{th}}$  number of bin and  $m$  represents the total number of bins.

The term 'a' in equation 3-1 represents the order of the entropy. The most interesting property of Renyi's entropy is its generality because of the choice of 'a'. As 'a' increases more weight is provided to the events with larger probability [108]. A study performed in ref [109] suggests more weight is given to the events with larger probability when  $a > 1$ ,

whereas more weight is given to the events with smaller probability when  $a < 1$ . Depending on the choice of ‘a’ Renyi’s entropy defines many other forms of entropy, such as:

- When ‘a’ approaches 0 it becomes Hartley’s entropy or max entropy. The calculation of this entropy is accomplished by equation 3-2.

$$H_0(x) = \log n \quad \text{Equation 1-2}$$

- When ‘a’ approaches 1, the limiting value of  $H(x_k)$  yields Shannon’s entropy [110]. The calculation of this entropy is accomplished by equation 3-3

$$\lim_{a \rightarrow 1} H_a(x) = \sum_{k=1}^n P(x_k) \log(P(x_k)) \quad \text{Equation 3-3}$$

- When ‘a’ approaches 2, it becomes quadratic Renyi’s entropy. The calculation of this entropy is accomplished by equation 3-4

$$H_2(x) = \log \left( \sum_{k=1}^n (P(x_k))^a \right) \quad \text{Equation 3-4}$$

4

- When ‘a’ approaches infinity, it yields min entropy. The calculation of this entropy is accomplished by equation 3-5

$$H_{\text{inf}}(x) = -\log \left( \max_k P(x_k) \right) \quad \text{Equation 3-5}$$

In this research we have chosen quadratic Renyi’s entropy ( $a=2$ , shown in equation 3-4) for measuring the disorderness in a AE waveform because of two reasons. Firstly, the contribution of events with large probabilities are higher in entropy computation than that of events with smaller probability. Therefore, it becomes reasonable to emphasize more on the events with larger probabilities by choosing  $a > 1$ . On the other hand, choosing a higher value of ‘a’ would significantly weaken the contribution of events with smaller probability. Considering this trade off,  $a=2$  provides an optimum solution because it provides more weight to the events with larger probability and it is close to Shannon’s entropy (close to 1) thus contains information on all probability events. Secondly, quadratic Renyi’s entropy has significant computational advantage compared to any other measures of entropy. By using Prazen window and kernel it can be estimated directly from the discrete volatge distribution, bypassing the need to accurately measure the probability distribution [111] [112][113]. This may reduce the computation time of disorderness if Parzen window and kernel density is

implemented in a AE data acquisition system. In order to measure the waveform disorderness in bits, the base of the log in equation 3-4 was chosen to be 2.

Like equation 3-1,  $P(x_k)$  in equation 3-4 also represents the discrete probability distribution of the voltage values, with  $K^{\text{th}}$  number of bin. There are a few methods to generate the discrete probability distribution [114] [115] [116]. In [117] [118], discrete probability distribution was generated by considering the original spectrum of the waveform. Discrete probability distribution in the research performed in [100] [74] was based on the frequency of occurrence with a bin width. A comparison between these two techniques in Ref. [115] suggests the probability distribution with frequency of occurrence and a bin width to be more reliable in the disorderness computation. The choice of bin width is an important factor in probability distribution generation. For ideal entropy computation, the bin width range should be set close to the data acquisition systems resolution. The AE system used in this research was a 16 bit AMSY-6, which has a resolution of 0.00305 mV. Therefore, bin width of 0.00305 mV was chosen for this research.

This research will refer to quadratic Renyi's entropy of AE waveform as AE entropy. The following steps demonstrate the AE entropy calculation procedure adopted in this research.

**Step 1:** Discrete voltage values of the AE waveform recorded by AMSY-6 data acquisition system are copied in a spreadsheet.

**Step 2:** The spreadsheet containing the discrete voltage values are imported into MATLAB<sup>TM</sup>. Discrete probability distribution of the voltage sequence is then generated using a bin width of 0.00305 mV.

**Step 3:** From the discrete probability distribution, calculation of AE entropy is accomplished by equation 4.

### **3.1.3 Evaluation of the new feature**

#### **3.1.3.1 Performance against Threshold**

In order to investigate the influence of threshold on AE entropy, two different type of evaluation technique were adopted. Firstly, the performance of AE entropy was evaluated with some modelled waveform from a signal generator. Secondly, a more realistic waveform (that resembles crack initiation) from PLB was used to evaluate the performance of AE entropy.

### 3.1.3.1.1 Influence of threshold on Modelled Waveform

In the first evaluation approach, burst waveforms were pulsed from a signal generator (4045B - B&K Precision), as a damage source, to the AE data acquisition system (Vallen – AMSY-6). Figure 3-5 illustrates the experimental setup used for these tests. Burst waveforms were chosen because it approximately resembles the one generated from yielding in austenitic stainless steel [77][73]. An appropriate frequency (*i.e.* of burst waveform) for this investigation would be the one that matches the frequency of waveform during yielding. The experimentally observed frequency during yielding is in the range of 190-270kHz [34][39]. In this research a frequency of 200kHz was chosen as it falls in the range of experimentally observed frequency (any frequency other than 200kHz that falls in the experimentally observed range could have also been used for an appropriate analysis). Figure 3-6 illustrates the nature of the burst waveform, pulsed form the signal generator. Equation governing these waveforms are shown in Appendix A.1. Each of the waveform in figure 3-6 were scaled to 80.7db in the signal generator and pulsed nine times to the AE data acquisition system. The nine waveform pulsed from the signal generator were acquired with nine different threshold settings. Table 2 shows these acquisition thresholds. The rest of the settings, shown in table 3, were constant among all the nine acquired waveform. It can be observed form table 3 that the acquisition settings used for this test is almost similar to the one in table 1, except FPLS and HDT. In this test, a higher FPLS is used, which is equivalent to the waveform length generated from damages in austenitic stainless [77]. The HDT value for calculating the traditional feature in this test is chosen as the same as the one used in ref [77]. Traditional features for all the waveforms, acquired during each pulsing, were calculated by the AE data acquisition system. AE entropy for all the waveform, acquired during each pulsing, was calculated from the discrete voltage values in MATLAB™ script. Finally, the influence of threshold on the AE entropy was evaluated and compared with the traditional features.

Table 2: Acquisition Threshold

Acquisition	Threshold (dB)
1	40
2	45
3	50
4	55
5	60
6	65
7	70
8	75
9	80

Table 3: Acquisition Settings for modelled waveform - threshold

Sampling Freq	5MZ
HDT	400us
Ream -time	1ms
Freq filter	95kHz – 850kHz
Duration per page	2,600µs
Threshold	40dB to 80dB

## Methodology

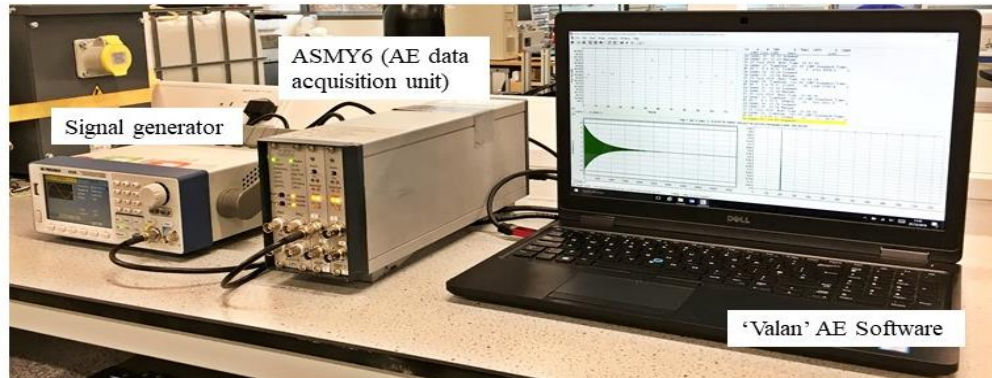


Figure 3-3: Experimental setup for model waveform test

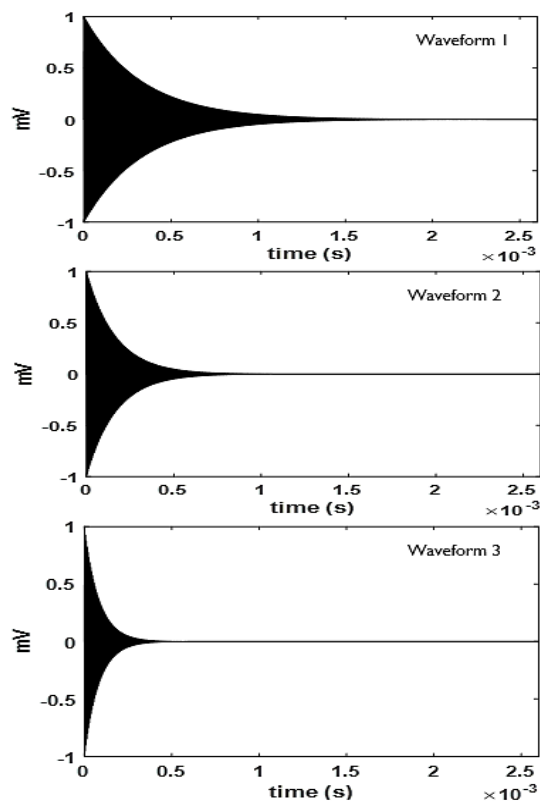


Figure 3-4: Nature of the waveform pulsed from signal generator to AMSY-6 system

### 3.1.3.1.2 Influence of threshold on Pencil Lead Break test

In the second approach, the performance of AE entropy was evaluated against a realistic waveform, that resembles crack initiation in metal. The realistic waveform was generated through PLB. In this test, a pencil lead consisting of 0.5mm in diameter and 3mm in length was broken by pressing it on a metal plate (12m in length, 12m in width and 5mm in thickness). Fracture of the lead resulted in generation of elastic wave in the metal plate. The frequency response of this elastic wave was not known prior to the test. Therefore, in order

## Methodology

to successfully capture the true nature of this elastic wave, an AE sensor (VS-900) sensitive to a wide range of frequency was chosen for this test. The AE sensor and its frequency sensitivity spectrum is shown in figure 3-1. The AE sensor was placed approximately 400mm away from the point where the pencil lead was broken. Figure 3-7 shows the experimental setup for this test. The experimental setup for this test was similar to the one in figure 3-3. The only difference was that the elastic wave captured by the AE sensor in this test, was passed to six different channel in ASMY-6 (AE data acquisition system). Each channel acquired the signal with a different acquisition threshold than the other. All the other acquisition settings, apart from threshold, were identical among the six channels. The threshold used for each channel is shown in table 4. The rest of the acquisition settings used for each channel is the same as the one in table 1. Traditional features for the waveform in each channel were calculated by the AE data acquisition system. AE entropy for the waveform in each channel was calculated from discrete voltage values. Finally, like the previous test, influence of threshold on AE entropy was evaluated and compared with the traditional features.

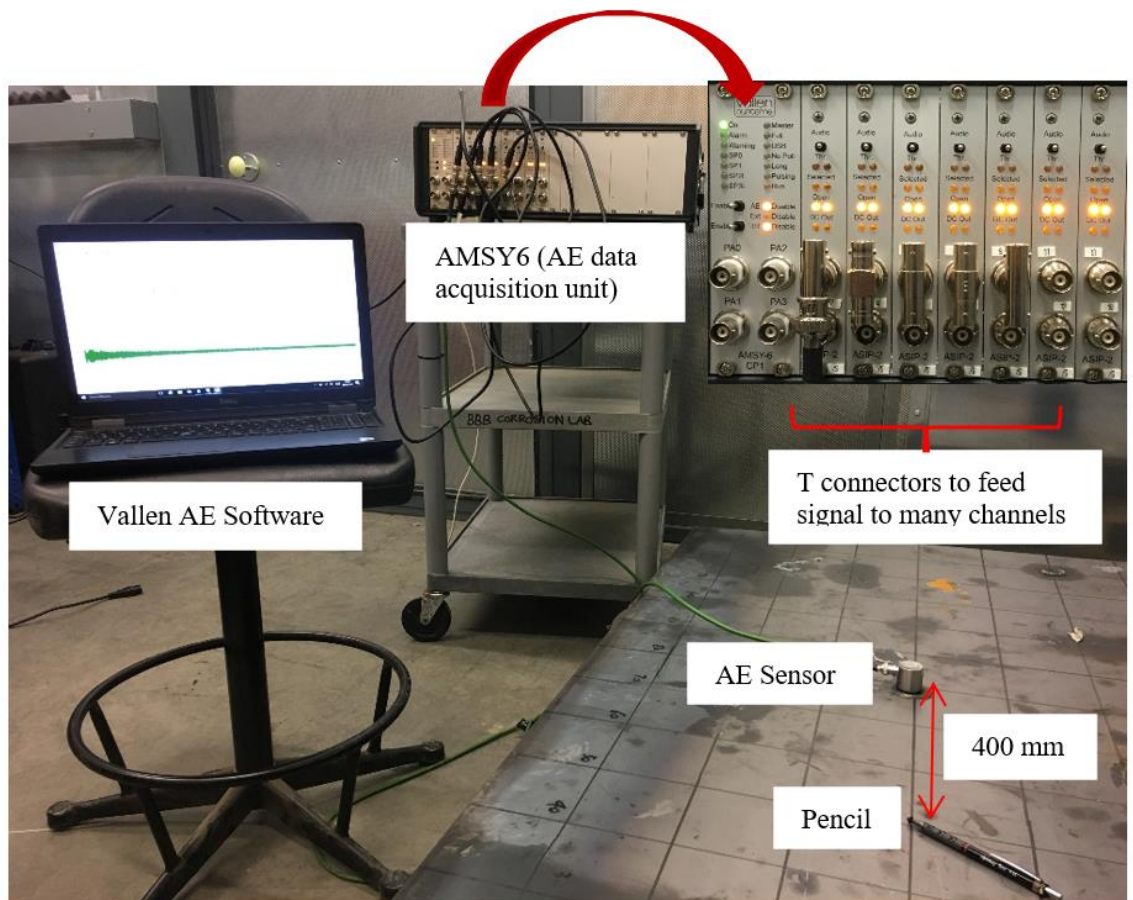


Figure 3-5: Experimental setup for pencil lead break test

## Methodology

Table 4: Threshold for each Channel

Channel	Threshold (dB)
1	45
2	50
3	55
4	60
5	65
6	70

### 3.1.3.2 Performance against Hit Definition Time

The influence of HDT on AE entropy was investigated with two evaluation technique. Firstly, a modelled waveform was used to evaluate the performance of AE entropy. Secondly, more realistic waveform, generated by pulsing elastic wave from the AE sensor on a metal plate, was used to evaluate the performance of AE entropy.

#### 3.1.3.2.1 Influence of HDT on Modelled waveform

In this evaluation approach, a waveform each containing three sub waveforms were pulsed from a signal generator (4045B - B&K Precision), as a damage source, to the AE data acquisition system (Vallen – AMSY-6). The experimental setup for this test is same as the one used in figure 3-5. Figure 3-8 illustrates the nature of the waveform pulsed from the signal generator. Burst type waveform, with a frequency content of 200kHz was chosen for each sub waveform within the entire waveform (a burst type nature was chosen, as it resembles the waveform generated from [73][77]). Frequency of 200kHz was chosen as it is close to the frequency of the waveform generated during yielding and crack initiation in austenitic stainless steel [34][39]. The waveform in figure 3-8 were scaled to 80db in the signal generator and pulsed three times to the AE data acquisition system. The three pulsed waveforms were acquired by the AE data acquisition system with three different HDT settings. The rest of the settings were constant among all the three acquired waveform. Table 5 below shows the HDT's used for this test. The rest of the acquisition settings were chosen to be the same as the one in table 1, apart from FPLS (FPLS was chosen to be the same as the duration of crack initiation in austenitic stainless steel with HDT of 400 $\mu$ s [77]). Traditional features of the acquired waveform were calculated by the AE data acquisition system. AE entropy for all the acquired waveform were calculated form the discrete voltage value in a MATLAB<sup>TM</sup> script. Finally, the influence of HDT on AE entropy was evaluated and compared with the traditional features.

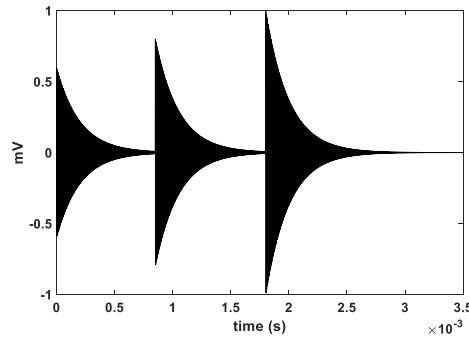


Figure 3-6: Nature of the waveform pulsed from the signal generator

Table 5: HDT for each acquisition

Acquisition	HDT
1	200 $\mu$ s
2	300 $\mu$ s
3	400 $\mu$ s

### 3.1.3.2.2 Influence of HDT on the elastic wave generated from AE sensor

A realistic AE waveform generated in metal was used to evaluate the performance of AE entropy. In this test, a metal plate (12m in length, 12m in width and 5mm in thickness) was excited with an AE sensor to generate elastic wave. A rectangular pulsing pattern shown in figure 3-9 was used as a means of excitation in the sensor.

Rectangular pulsing pattern was used to introduce precise delay between each pair of rectangular pulse. The delay was used to separate the generation of elastic wave in the plate, which supported the investigation on the influence of HDT in the recorder waveform. To vary the amplitude of the elastic wave in the plate, different heights of the rectangular pulses were chosen (height of the first and second pulse were 0.5 and 0.75 times the third pulse). The elastic wave was captured as an analogue signal, with another AE sensor attached to the metal plate. The total distance between the sensors was 13cm. Figure 3-10 illustrates the sensor arrangement used in the test. The rectangular pulse like PLB represents an impulse excitation in the plate. Therefore, the frequency response of the elastic wave in the plate was not known prior to the experiment. A Vallen VS-900 was chosen as an AE sensor, for both the pulsing and capturing of elastic wave. This sensor was chosen as it was sensitive to a wide range of frequency and can successfully capture the true nature of the elastic wave.

Figure 3-1 shows an image of the sensor and its frequency sensitivity spectrum. The analogue signal from the sensor was then passed on to three different channel in AMSY-6 (16 channel data acquisition system). Each channel acquired the signal with a different HDT than the other. The rest of the acquisition settings were same as the one in table 1. The traditional AE features for each channel were calculated by the AE data acquisition system and AE entropy was calculated from the discrete voltage value in a MATLAB™ script. Finally, the influence of HDT on AE entropy was evaluated and compared with the traditional features.

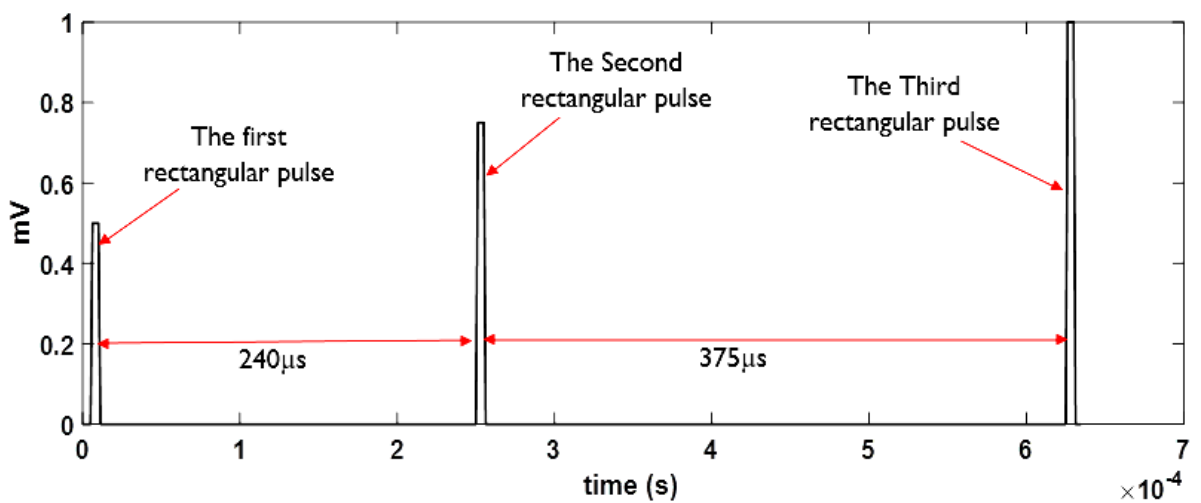


Figure 3-7: Rectangular pulsing pattern

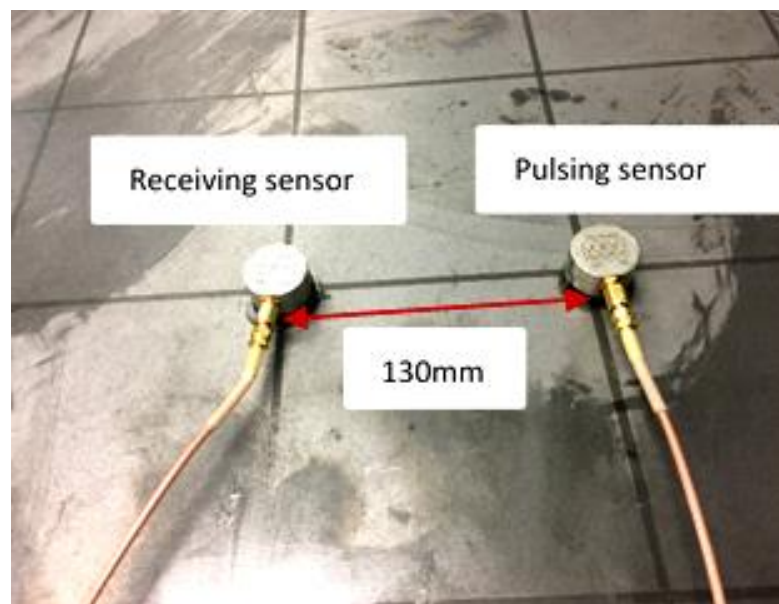


Figure 3-8: Sensor arrangement

### 3.1.3.3 Performance against disorderness

The performance of AE entropy was further evaluated by accessing its sensitivity to the disorderness. In this investigation, Signal to Noise Ratio (SNR) of 10, 20, 30 and 40 was added to each of the waveform in figure 3-6. SNR was added to these waveforms to vary the degree of disorderness in them. The waveforms after the addition of SNR is shown in figure 3-11. All these waveforms were scaled to 80.7db in the signal generator and pulsed to the AE data acquisition system. The AE entropy of these waveforms were calculated in a MATLAB<sup>TM</sup> script and its sensitivity to the disorderness was accessed.

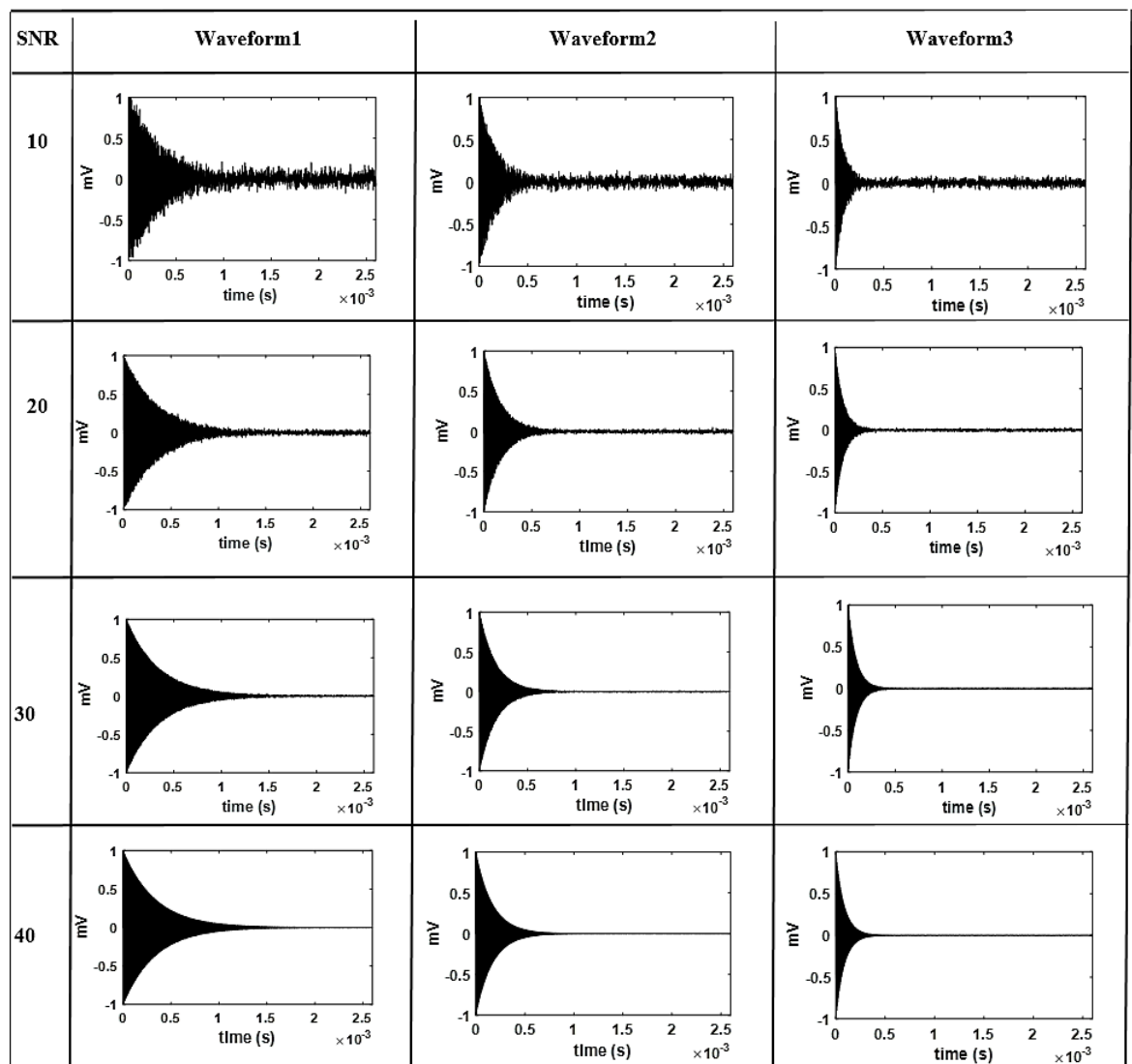


Figure 3-9: Waveforms with SNR

## 3.2 Experimental validation on standard specimen

The performance of AE entropy was validated with the elastic wave generated from damage initiation in the standard specimen. Both fatigue and tensile loading was used as an external stimulus to initiate damages in the standard specimen. The Standard specimen was designed with austenitic stainless steel, as it is used in the construction of the primary wall in LNG cargo tank.

### 3.2.1 Fatigue Test

Sloshing of LNG cargo in a tank results in structural degradation/failure of its primary wall. The initial stages of structural failures are localized yielding and crack initiation. Sloshing exhibits a fatigue loading condition on the primary wall [13][20]. In order to investigate on the possibility of AE entropy to be used in CBM (identifying initial damages so that a maintenance can be carried out), there is a need to understand its sensitiveness to identifying damage, when fatigue is an external stimulus to the material of the primary wall. The main aim of these test is to determine whether AE entropy is able to identify the fatigue damages in standard specimen, made from material (*e.g.* austenitic stainless steel) of primary wall.

#### 3.2.1.1 Materials and Specimen

The mechanical properties and chemical compositions of the austenitic stainless steel used in design of the standard specimen is shown in table 6 and 7 respectively. The values in table 6 and 7 were taken from the manufacturers data sheet. Dog-bone shaped standard fatigue specimens were designed from 6mm plate of this material. Standard E466-15 was used as a guideline to design the specimens [119]. A schematic illustration of the specimen used in the test is shown in figure 3-12. Four specimens were designed and tested in total. The direction in which the specimen would be loaded was parallel to the longitudinal direction of the parent material. Prior to the test, the gauge of all the specimens were polished with 1200 grit emery paper. This was done to reduce the stress concentration areas. There was no pre-crack machined in the specimen for this tests, because the main aim was to determine whether AE entropy is capable of identifying initial stages of failure (*e.g.* localized yielding and crack initiation).

Table 6: Mechanical Properties

Young's modulus (GPa)	193GPA
Yield Strength (MPa)	347MPA
UTS (MPa)	613MPA

## Methodology

Table 7: Chemical Composition

C	0.025
Mn	1.32
P	0.03
S	0.002
Si	0.48
Cu	0.36
Ni	10.03
Cr	16.58
Mo	2.02
Nb	0.041

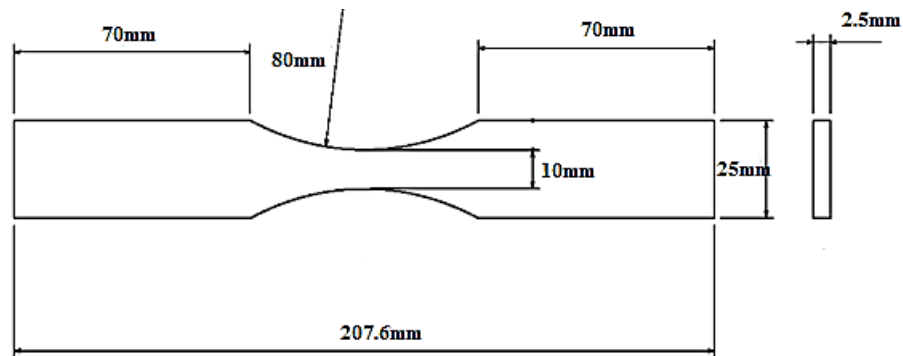


Figure 3-10: Illustration of the fatigue specimen used in the test

(a)

(b)

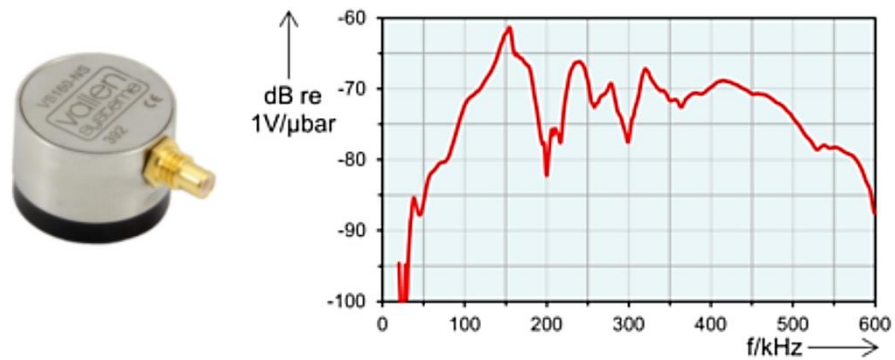


Figure 3-11: (a) VS-160 AE sensor (b) Frequency sensitivity spectrum of the sensor

### 3.2.1.2 AE Testing Procedure

The elastic waves emitted in the specimen were captured as analogue signals by a couple of Vallen VS-160 AE sensors. Figure 3-13 shows an image of this sensor and its frequency sensitivity spectrum. This sensor was chosen because it has a peak sensitivity close to the frequency of AE waveform generated during yielding and crack initiation in austenitic stainless steel [34][39]. The sensors were attached on the same side of the specimen with glue (adhesive compound), one on each loading direction, at a distance of 45mm away from

the specimen centerline. The glue provided adequate bonding between the sensor and specimen. However, the bonding was further secured with adhesive tape. The glue also provided sufficient coupling between the sensor and the specimen. Figure 3-14 shows the schematic illustration of the sensor setup in the specimen. Before the test, to ensure the sensor is functioning to its full capability, calibration test as per the ASTM E1106 standard was performed [120].

The analogue signals captured by the sensors were amplified by a 34dB Vallen AEP4H amplifier. The amplified signals were fed to the AMSY-6 data acquisition system which digitized the signals with a sampling frequency of 5MHZ. After digitization, AE signal were stored as a waveform. Features were calculated from the recorder waveform by the AMSY-6 data acquisition system. The acquisition settings for calculating the traditional features are shown in table 3. AE entropy was calculated form the discrete voltage values in MATLAB™ script.

During AE monitoring, fatigue load results in several unwanted signals, originating from the loading train [98]. In order to avoid unwanted noise, a 1D localization filtration technique was used.

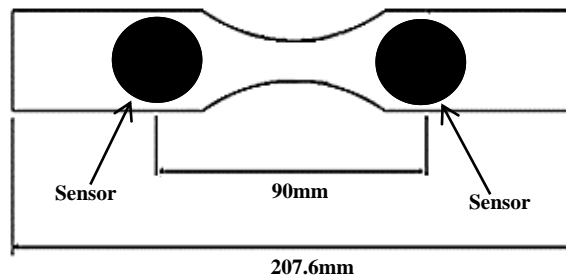


Figure 3-12: Sensor Setup in the fatigue specimen

Table 8: Acquisition settings for fatigue test

Sampling Freq	5MZ
HDT	400us
Ream -time	1ms
Freq filter	95kHz – 850kHz
Duration per page	820μs
Threshold	45dB

1D localization technique avoided reflections and noise generated at the grips (*i.e.* loading contact point). Wave velocity chosen for this technique was 5000m/s and was calculated in AMSY-6 data acquisition system by pulsing elastic waves from one sensor and receiving the signal with another sensor in the specimen. The wave velocity calculated by this method is consistent with the asymmetric (A0) wave velocity of 4873.3 to 4900m/s, below 200 kHz (the dispersion curve is shown Appendix A.2). The reliability of calculated wave velocity was checked by performing PLB on the surface of the specimen and checking the mapped accuracy (*i.e.* by comparing the mapped location in the software with the physical location where the pencil lead was broken). The localization results from the PLB test showed good agreements with the actual location in the specimen where PLB was performed. This filtration technique considered signals generated within the gauge section of the specimen to be useful and avoided unwanted signals from the grips.

### 3.2.1.3 Secondary Monitoring Technique

In order to find out the exact time instance of damages (*e.g.* localized yielding and crack initiation) in the specimen during loading, it was simultaneously monitored with Digital Image Correlation (DIC) and global strain measurement, alongside AE monitoring. The time instance of damages identified by the secondary monitoring techniques was cross validated with AE entropy. This was done to understand the trend in AE entropy during damages and gain confidence in its reliability.

#### 3.2.1.3.1 Global Strain Measurement in fatigue

In this research, the global strain of two specimens were monitored during the entire length of the fatigue test. The global strain measurement was undertaken by extracting the maximum cross head displacement of the loading jaw in a cycle. However, in order to compress the total amount of data, the maximum cross head displacement in a cycle was extracted after every 76 cycles. From the cross head displacement, the global strain was calculated according to the formula shows in equation 3-6.

$$Global \ Strain = \frac{Cross \ Head \ Displacement}{207.6mm(Specimen \ Length)} \quad \text{Equation 3-6}$$

### 3.2.1.3.2 Digital Image Correlation measurement in Fatigue

DIC is an optical method for measuring the surface displacement of a component. The principles of DIC is based on tracking the facets (blocks of pixels) in the digital images of the surface, captured during the entire range of deformation. The facets are tracked by searching the area with the same light intensity distribution. The strains are then calculated from the displacement of the coordinates between facets.

During the fatigue test of an un-notched specimen, crack initiation sites are on the surface for small and intermediate cycles to failure. However, for high cycles to failure the initiation sites may be located on the internal zone of the surface [67]. The fatigue tests conducted in these research are all low cycle, therefore, crack initiation sites are expected to be on the surface of the specimen. Cyclic loading results in plastic zone formation due to localized crack coalesce and growth. Since DIC measures the surface displacement, it has the potential to identify this plastic zone. The main aim of DIC in this research is to obtain information regarding the time of occurrence of plastic zone formation. This information will be cross validated with the behaviour of AE entropy at that time. DIC has been widely used as a secondary monitoring technique in the past to validate AE results[121][122][123].

In this research the gauge length of two fatigue specimens, opposite to the surface where the AE sensors were attached, were monitored with DIC during loading. The digital images were captured with an ARAMIS-5m DIC camera, controlled by GOM correlate software. Figure 3-15 shows the camera used for this research, (the specification of the camera is shows in the Appendix A.3). DIC measurement and AE data was synchronized by starting the DIC camera and AE data acquisition system at the same time, such that they start capturing data simultaneously.

The loading data from the loading machine was fed to the software controlling the DIC camera, this enabled the images to be taken during the peak load of the cycle. However, following the loading pattern and taking timely images limited the maximum capacity of the camera to 500 burst of images (each burst contains 10 images). The previous specimens failed at approximately 150,000 cycles during cyclic loading. The specimens tested with DIC as a secondary monitoring technique were identical to the previous specimens and were subjected to the same loading conditions. Therefore, it was assumed that these specimens

would fail at the similar number of cycles. Hence, to distribute the 500 burst of images along the entire loading range, images were taken at an interval of 300 cycles (150,000/500).

In order to improve the image texture, the entire gauge length of the specimen was sprayed with speckle pattern prior to the test. Figure 3-16 shows the gauge section of the specimen with sprayed speckle pattern. There were several images taken by the ARAMIS-5m DIC camera during the tests. One of such image during a fatigue test, just before the onset of loading is shown in figure 3-17. It can be seen in this figure that the gauge surface has been prepared (sprayed with speckle pattern) for a better image quality. Facet with pixel size of 19 were chosen in post processing of the images. The distance between adjacent facets were chosen to be 19 pixels. These values were chosen as it is recommended by GOM community. These post processing parameter has also been used in a similar investigation with good accuracy[124].

#### 3.2.1.4 Loading Condition

Uniaxial cyclic load was applied to both the cross sectional ends of the specimen, with Instron Servo-hydraulic machine, controlled by LabVIEW software. In order to effectively load the specimen (without slippage), 40mm of its length from each end was securely gripped with the loading jaw of the Instron Servo-hydraulic machine.



Figure 3-13: ARAMIS 5M DIC Camera

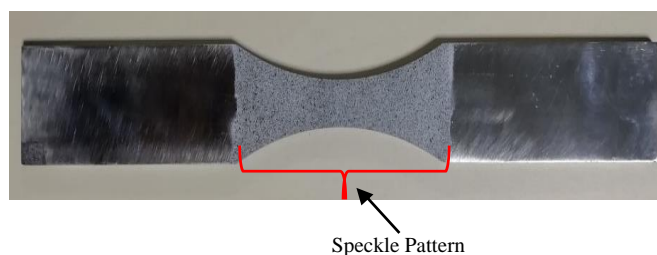


Figure 3-14: Speckle pattern in the gauge of fatigue specimen

## Methodology

Figure 3-18 shows a schematic illustration of the loading condition. The loading was sinusoidal in nature, with a frequency of 5Hz. Stress controlled loading, with a ratio of 0.1 was adopted for this test. Within every cycle, the maximum and minimum engineering stress exerted on the specimen was 480MPa and 48MPa respectively. The maximum stress was above the yield point and well below the ultimate tensile strength, the minimum stress was below the yielding point (refer to table 6 for the mechanical properties).

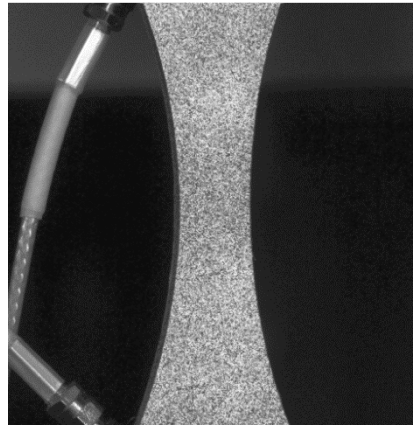


Figure 3-15: An Image taken by DIC camera, during a fatigue test

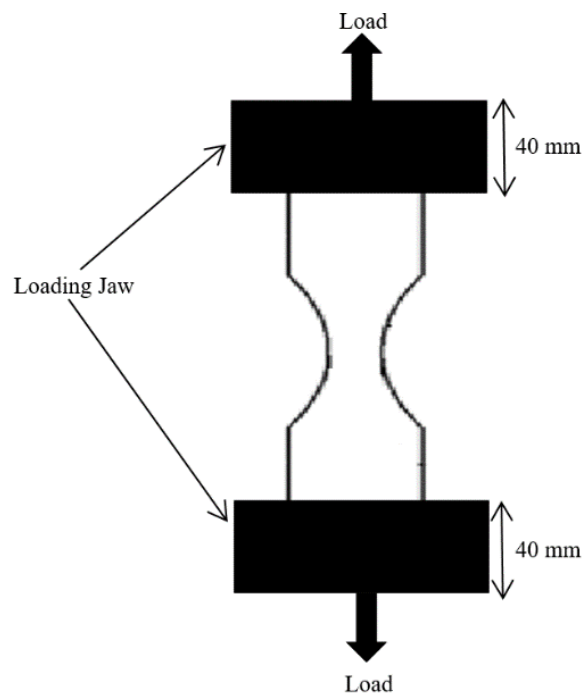


Figure 3-16: Schematic of Loading Condition in fatigue test

## Methodology

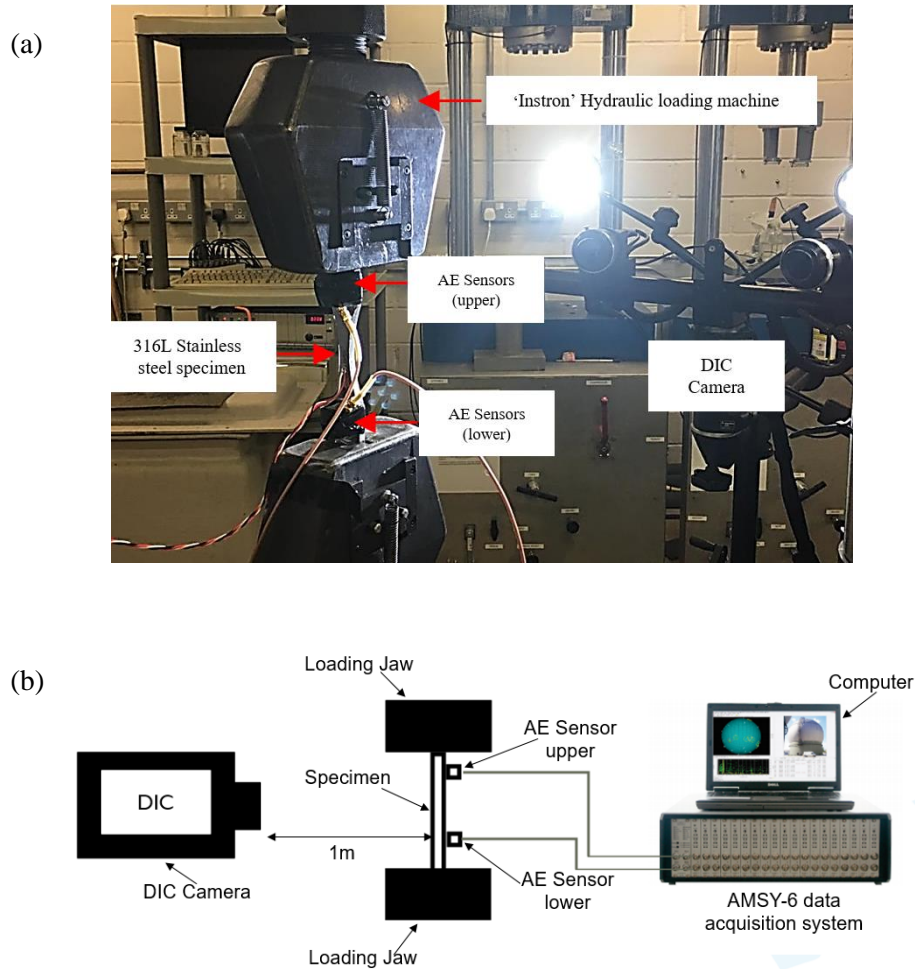


Figure 3-17: (a) The experimental Setup for fatigue test (b) The schematic of the experimental setup

### 3.2.1.5 The experimental Setup

The entire experimental setup, including specimen, AE, secondary monitoring technique and loading condition is shown in figure 3-19.

### 3.2.2 Tensile Test

Localized yielding/deformation in the primary wall of the LNG cargo tank is one of the initial stage of its failure. In order to determine the possibility of AE entropy to be implemented in the CBM of LNG cargo tank, it is necessary to understand its sensitivity towards deformation of the material of the primary wall (initial stage of failure of the cargo tank). The main aim of this test is to validate the performance of AE entropy during tensile deformation of standard specimen made from the material of the primary wall (*e.g.* austenitic stainless steel). The experimental setup for tensile test is same as the one for fatigue test.

### 3.2.2.1 Materials and Specimen

Austenitic stainless steel for the design of standard tensile specimen was same as the one used in fatigue test (mechanical properties and chemical composition of the material is shown in table 6 and 7, refer to section 3.2.1.1). ASTM standard E8/E8M-09, was used as a guideline to design the specimen. A schematic illustration of the specimen is shown in figure 3-20. Three specimen was designed and tested in total. Two of them were un-notched, identical to the one in figure 3-20. In the other one, a notch of 1mm in depth and 30° in tip radius was introduced at a side of the specimen, in the middle of the gauge, the rest of the dimensions were identical to the one in figure 3-20. The direction in which the specimen would be loaded was parallel to the longitudinal direction of the parent material. To reduce the stress concentration areas, the gauge of all four specimens was polished with 1200 grit emery paper. Like the fatigue test, there was no pre crack machined in the tensile specimen, because the main aim was to determine the effectiveness of AE entropy during deformation of the material instead of crack propagation.

### 3.2.2.2 AE Testing Procedure

The elastic waves generated in the specimen were captured as analogue signal by a Vallen VS-160 sensors. An image of this sensor and its frequency sensitivity spectrum is shown in figure 3-13. The sensor was same as the one used in fatigue test. It was chosen because of its peak sensitivity at 160 kHz, which is close to the frequency of waveform generated during yielding and crack initiation in austenitic stainless steel [34][39]. The sensor was attached to one side of the specimen, on a loading direction, in the transition between the gauge and grip region. The distance between the sensor and the centreline of the specimen was 50mm. Glue was used as a means to attaching the sensor to the specimen. Glue provided adequate bonding and acted as a coupling medium between the specimen-sensor interface. Figure 3-21 shows the sensor setup used in the test. Before the onset of loading, calibration test as per ASTM E1106 standard was carried out to check the functionality of the sensor [120].

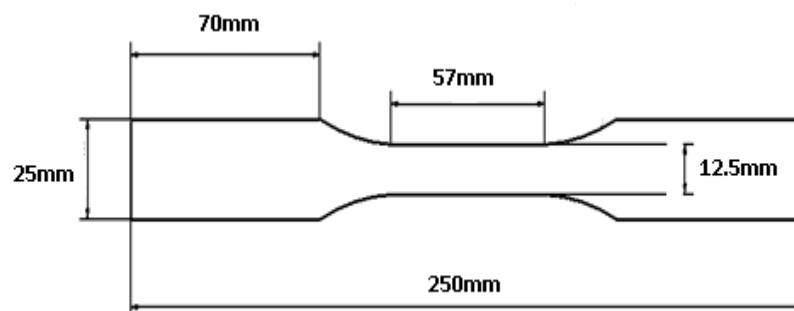


Figure 3-18: Illustration of the tensile specimen used in this test

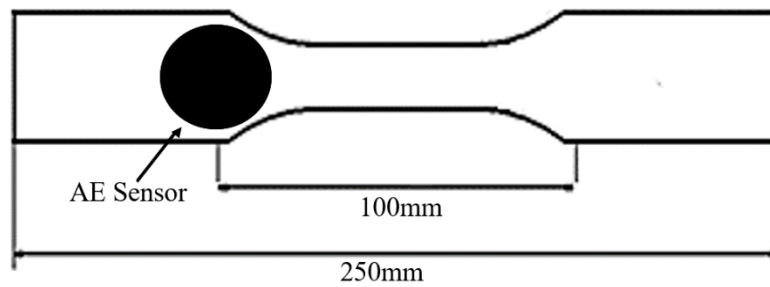


Figure 3-19: Sensor Setup in the tensile specimen

The analogue signal from the sensor were amplified by a 34dB AEP4H Vallen amplifier and passed to AMSY-6 data acquisition system. The AMSY-6 system captures the amplified signal with a sampling frequency of 5MHz. The digitized signals were stored in the computer as waveforms. The traditional features of the waveforms were calculated by the AMSY-6 system, the acquisition settings used for this test is same as the one used in fatigue test (refer to table 8 for acquisition settings). AE entropy of the waveform were calculated from its discrete voltage value in a MATLAB™ script.

During tensile test, there was no noise generated from the grip because the tensile loading was very slow and only acted in one direction, unlike fatigue loading. Therefore, there was no filtration technique used during the test.

### 3.2.2.3 Secondary Monitoring Technique

In order to validate the performance of AE entropy during deformation, there is a need to correlate it to the material behaviours such as engineering stress and strain.

The use of extensometer is a traditional method of extracting the strain in the material during tensile deformation. In this study, the deformation was expected to be quite large (twice the size of specimen length) and there was a possibility of the extensometer to scratch against the surface of the specimen during deformation. Scratching of the extensimeter on the surface of the specimen was expected to make unwanted noise in terms of AE. To avoid this, DIC and global strain measurement was used to calculate the strain in the material during the entire length of the test. Engineering stress for every strain was calculated from its corresponding load data and initial cross section of the specimen.

### 3.2.2.3.1 Digital Image Correlation measurement in Tensile Deformation

The gauge length of all three specimens (two notched and one un-notched), opposite to the surface where the sensor was attached, was monitored with DIC during the entire range of deformation. The camera used to take the digital images during deformation is same as the one used in fatigue test (refer to figure 3-15). To improve the image texture, speckle patterns were introduced in the gauge section of all the specimen before the test.

Loading data was fed to the software controlling the DIC camera. Unlike fatigue test, there is no cyclic loading in this test. There was no requirement of any images to be taken at the peak load in a cycle, like the fatigue test. As a result, there was no limitation of the number of sub images within a burst of image. The length of this test was expected to be very small compared to fatigue test. (length of fatigue test:  $150000 \text{ cycles}/5\text{Hz} = 8.3\text{hr}$ . length of tensile test: approximately 30 min, at a deformation rate of 1mm/min). Therefore, the total limit of 5000 images could be distributed along the entire length of the test, with very small interval. However, having a very small interval would significantly increase the total number of image and make the post processing lengthy. Considering a trade-off, an image was taken in every second during the entire range of deformation (60 images in a minute or 60 images in a millimetre of deformation, if the deformation rate is 1mm/min). This was assumed to provide sufficient resolution to monitor the deformation. In order to improve the image texture, the entire gauge length of the specimen was sprayed with speckle pattern prior to the test as shows in figure 3-22.

One of the images captured by the DIC camera, prior to the onset of loading, during the tensile deformation is shown in figure 3-23. Like the fatigue test, pixel size of 19 and point distance of 19 was chosen as a post processing parameter of the images for this test. In the processed image, prior to the onset of loading, two evaluation points were chosen on the gauge length. This points were in the loading direction and equal in distance from the centreline of the specimen (the total distance between the points were 10mm). Displacement data were extracted from these points for all the images taken during deformation. Finally, strain in each image (between the evaluation points) was calculated by equation 3-7. The corresponding engineering stress was calculated from the load recorded during the capture of each image and initial cross section area of the specimen gauge. Equation for calculating the engineering stress is shown in equation 3-8.

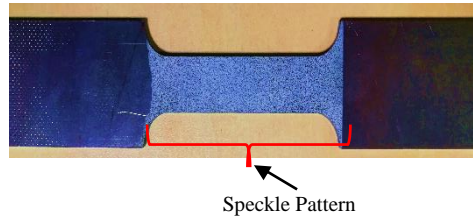


Figure 3-20: Speckle pattern in the gauge of tensile specimen

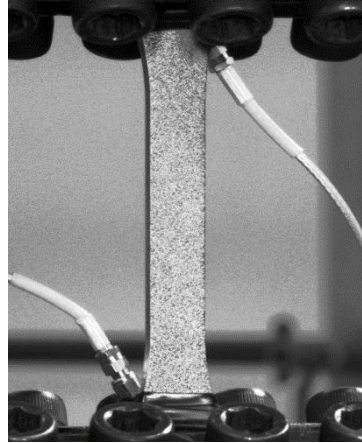


Figure 3-21: An image taken by DIC camera during tensile deformation

$$\text{Strain} = \frac{\text{Displacement point1} - \text{Displacement point2}}{\text{Distance between points}} \quad \text{Equation 3-7}$$

$$\text{Stress} = \frac{\text{Load during image}}{\text{Initial cross section area}} \quad \text{Equation 3-8}$$

### 3.2.2.3.2 Global strain measurement in tensile deformation

The global strain of all three specimens (two notched and one un-notched) was monitored during the entire range of deformation. Similar to the fatigue test, the global strain measurement was undertaken by monitoring the cross head displacement of the loading machine. From the cross head displacement, the global strain was calculated according to equation 3-9. The corresponding value of engineering stress was calculated from the load during each strain measurement and the initial cross section of the specimen gauge. The equation for calculating engineering stress is shown in equation 3-10.

$$\text{Global Strain} = \frac{\text{Cross Head Displacement}}{250\text{mm}(\text{Specimen Length})} \quad \text{Equation 3-9}$$

$$\text{Stress} = \frac{\text{Load during strain}}{\text{Initial cross section area}} \quad \text{Equation 3-10}$$

### 3.2.2.4 Loading Condition

Uniaxial tensile load was applied to both the cross sectional end of the specimen with Instron servo-hydraulic loading machine controlled by LabVIEW software. Displacement controlled loading, at a rate of 1mm per minute were applied to the specimen. Like the fatigue specimens, 40mm of the tensile specimen were gripped with the loading jaw of the Instron servo-hydraulic machine. Figure 3.24 shows a schematic illustration of the loading condition during tensile deformation.

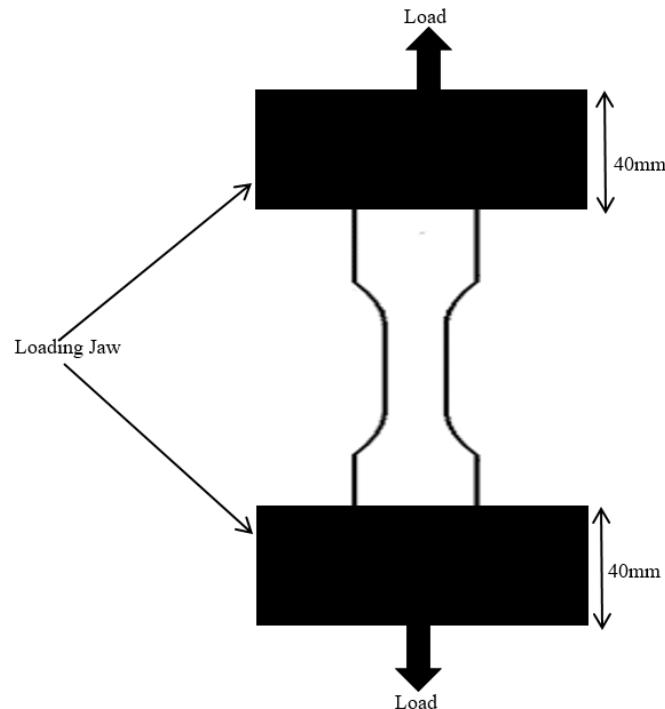


Figure 3-22: Loading Condition of tensile specimens

### 3.3 Chapter summary

This chapter begins by exploring a new feature of the waveform that is independent of the acquisition settings (*i.e.* threshold and HDT). An investigation on the AE waveform generated from PLB on a metal plate, revealed that the discrete voltage values which makes up the waveform contains component which are below the threshold and outside the HDT and provided a FPLS is used, the number of discrete voltage values are constant for all the recorded waveform. This lead to the idea that if a feature is extracted from the discrete voltage values of the waveform, it will be independent of the threshold and HDT. Amongst few ideas, measure of disorderness or uncertainty of the discrete voltage values in a waveform was adopted to represent the new feature. This was chosen because it was able to distinguish the uniqueness of a waveform with respect to the other. The disorderness of the discrete voltage values in a waveform was calculated using quadratic Renyi's entropy. The new feature was termed as AE entropy in this research.

This chapter provides two detail procedures to evaluate the performance of AE entropy against a range of threshold and HDT settings, under ideal condition. A procedure for validating the effectiveness of AE entropy with respect to identifying damages (*i.e.* critical damages in the primary wall), through a series of fatigue and tensile tests on standard specimen is also provided in this chapter. In order to cross-validate the performance of AE entropy with damage mechanism, the specimens are simultaneously monitored with global strain and DIC measurement alongside AE. These procedures include a detail discussion about the choice and justification of the experimental setup adopted for this study.

## 4 Results

### 4.1 Initial Evaluation of the new feature

#### 4.1.1 Performance against threshold

This section highlights the influence of threshold on AE entropy, during both the evaluation with modelled waveform and PLB test. The performance of both the AE entropy and traditional features against threshold is reported. The results of traditional features are included to compare their performance with AE entropy.

##### 4.1.1.1 Evaluation with the modelled waveform

Each type of waveform in figure 3-6, was acquired by the AE data acquisition system nine times, with different acquisition thresholds (refer to figure 3-5 for the experimental setup). The influence of different acquisition threshold, on the traditional features and AE entropy are is shown in figure 4-1, 4-2 and 4-3 respectively (figure 4-1 includes the results for waveform 1 in figure 3-6, figure 4-2 includes the results for waveform 2 in figure 3-6 and figure 4-3 includes the results for waveform 3 in figure 3-6).

In order to highlight the influence of threshold, a linear trend-line has been added to all the graphs in figure 4-1,4-2 and 4-3. The graph (a), (b), (c) and (d) of these figures represents the influence of acquisition threshold on Risetime, Duration, Count and Energy respectively. It can be observed in these graphs that as the acquisition threshold increases, all of these features recorded by the AE data acquisition system decreases. The decrease in Risetime, Duration and Count is very significant with threshold, whereas the decrease in energy is noticeable only at higher threshold in all the figures. The graphs (e) and (f) of the three figures represent the influence of threshold on peak-amplitude and AE entropy respectively. It is evident from these graphs that these features do not show any variance with the acquisition threshold. The feature extraction steps of these features does not take into account of the acquisition threshold as a result are independent from it.

## Results

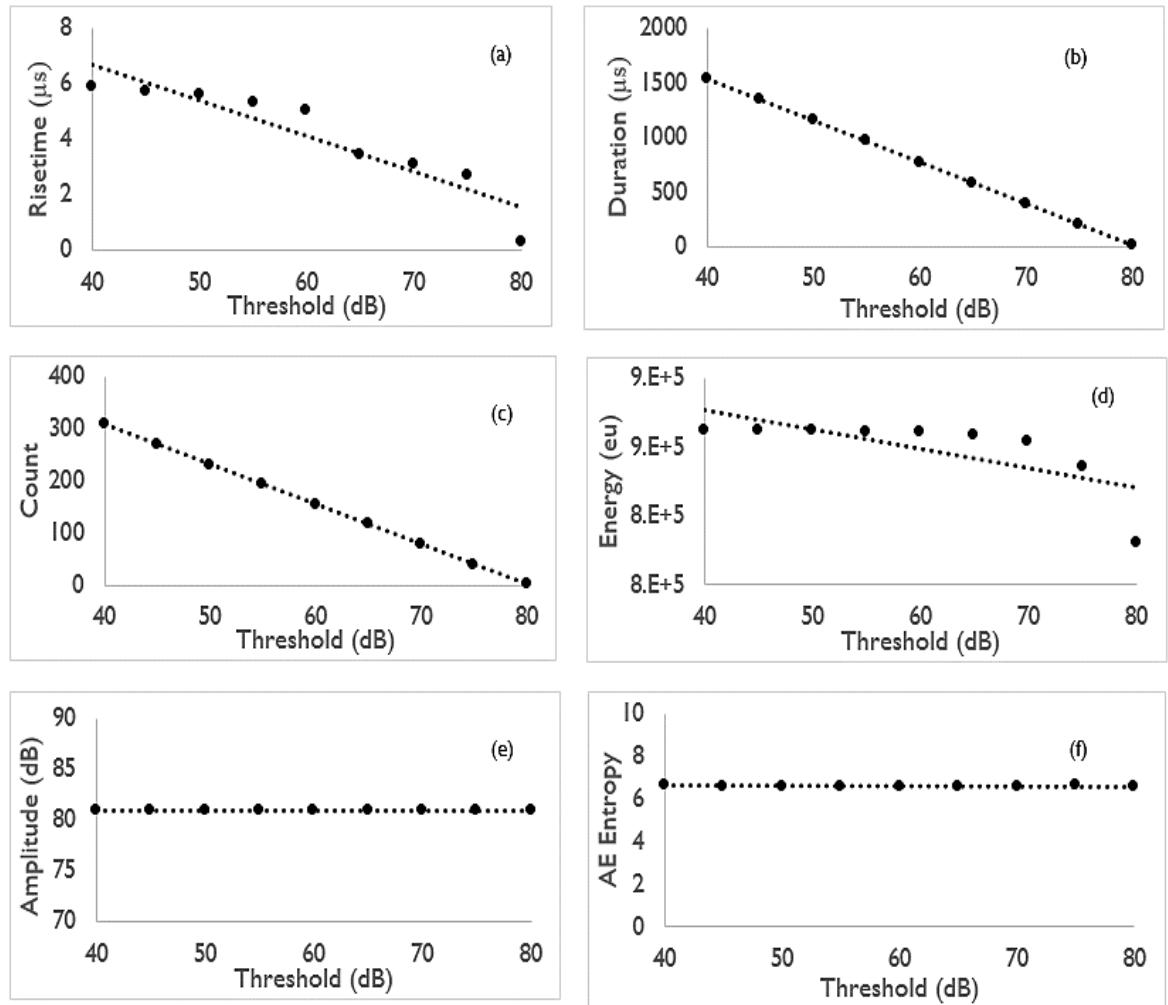


Figure 4-1: Influence of acquisition threshold on waveform I: (a) Rise-time (b)Duration (c)Count (d)Energy (e)Peak-amplitude and (f) AE entropy

In AE monitoring, the data acquisition system records a waveform along with a fixed pre-trigger (*e.g.* 40μs). AE entropy is calculated from the entire discrete voltage values in the waveform (both above and below the threshold), including those in the pre-trigger. As a result, once a waveform is recorded, AE entropy computation is independent of threshold. However, threshold influences computation of other feature (*e.g.* Count, Risetime, Duration and Energy), but not used for AE entropy calculation. Peak amplitude has actively been used in the past as an indication of critical damage. Peak-amplitude is the maximum voltage in a waveform. Although it is independent of threshold, it uses very limited information of the waveform, unlike AE entropy. During AE monitoring, movement of cable attached to the sensor can trigger waveforms with few high peaks. Although these waveforms are regarded as noise, they can all have high peak-amplitude features. As a result, these waveforms can mistakenly be interpreted as a critical damage source. In some cases, there is a need to

distinguish between different types of waveform shape in AE monitoring[125]. This will not be possible with peak-amplitude observation (since the highest peak is not a representation of the waveform shape).

The graph (e) of the three figures shows that each one of them has the same peak amplitude feature (80.7dB). Although the nature of the pulsed waveforms, shown figure 3-6 are different (different amount of decaying), all acquired waveform have the same peak amplitude feature. This is because the waveforms in figure 3-6 have all been scaled to 80.7dB before pulsing to the AE data acquisition system. Whereas, it is evident from graph (f) of the three figures that each one of them has a different AE entropy. The different value of AE entropy form one figure to another is due to the difference in nature of the pulsed waveform.

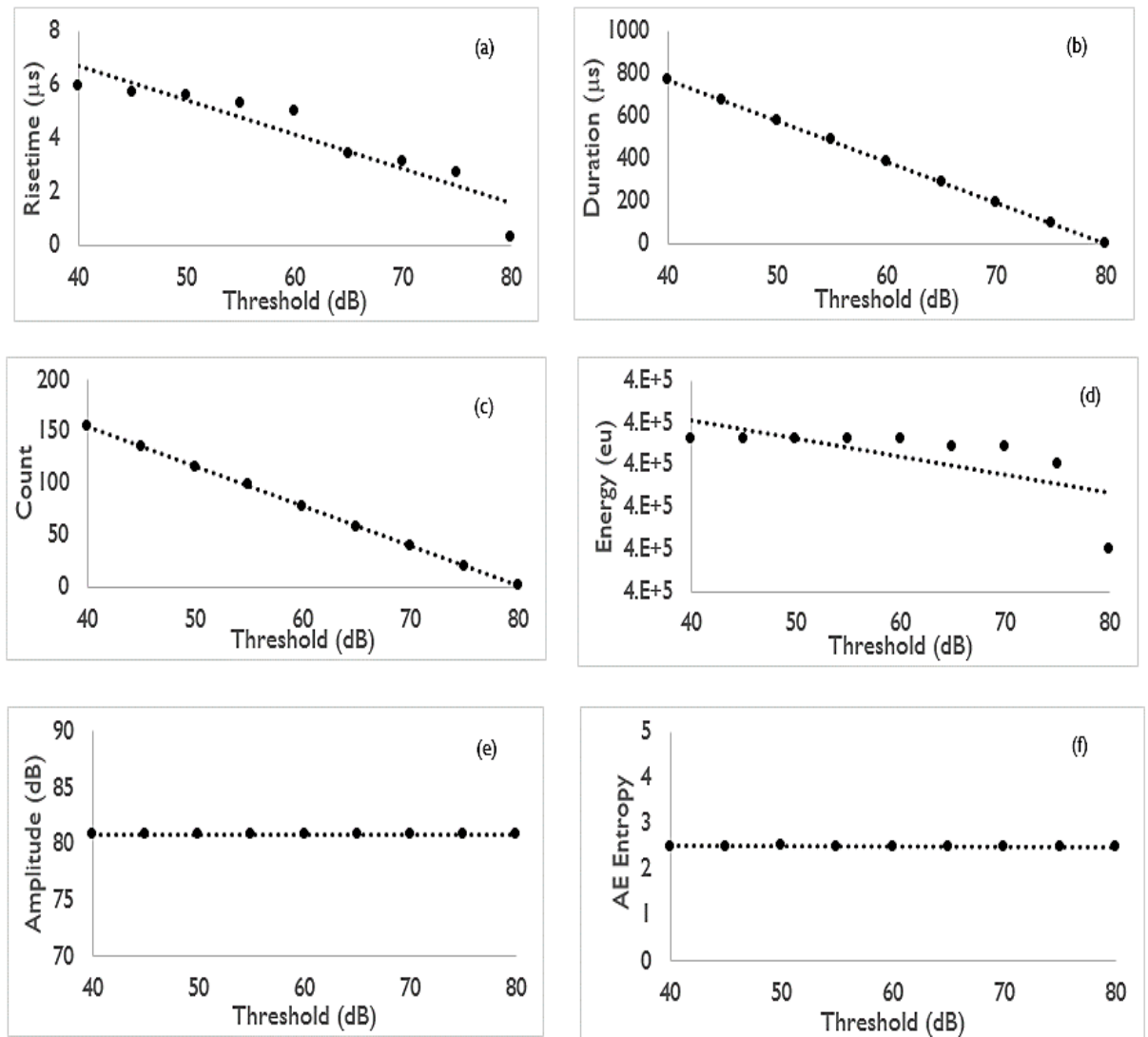


Figure 4-2: Influence of acquisition threshold on waveform 2: (a) Rise-time (b)Duration (c)Count (d)Energy (e)Peak-amplitude and (f) AE entropy

## Results

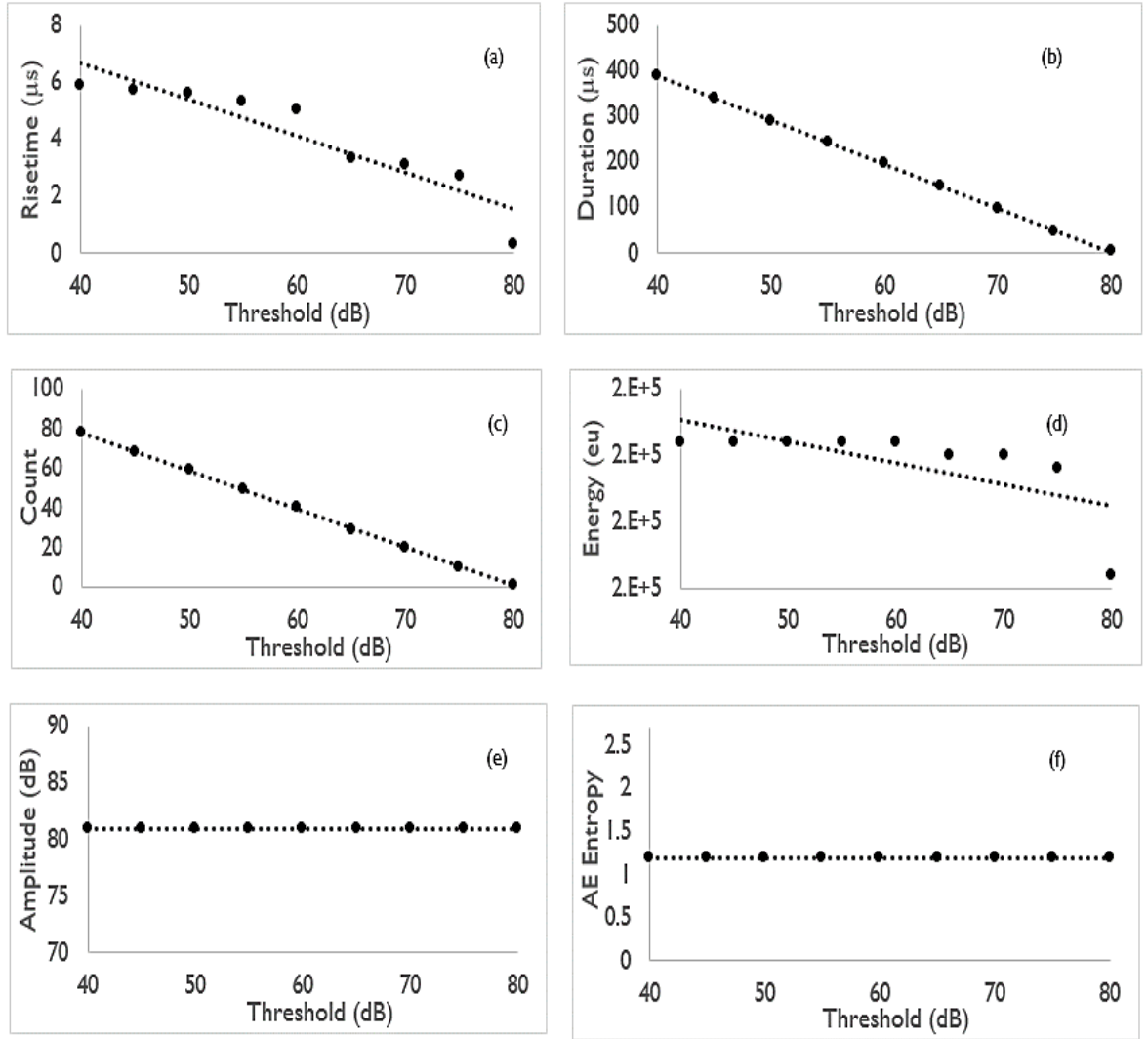


Figure 4-3: Influence of acquisition threshold on waveform 3: (a) Rise-time (b)Duration (c)Count (d)Energy (e)Peak-amplitude and (f) AE entropy

The computation of AE entropy takes into account of the amount of discrete voltage values in a waveform, that are away from the zero. Higher the number of discrete voltage values that are away from zero, higher is the AE entropy. The number of discrete voltage values in all the acquired waveforms (27 waveforms, 9 for each waveform type in figure 3-6) is the same. This is because they all have the same sampling frequency and FPLS. However, the amount of discrete voltage value that are away from zero, are different among the acquired waveform. The waveforms acquired as a result of pulsing waveform 1 in figure 3-6, have a higher number of discrete voltage values that are away from zero. Therefore, have a higher AE entropy compared to waveforms acquired by pulsing waveforms 2 and 3 in figure 3-6. Similarly, the AE entropy of the waveforms acquired as a result of pulsing waveform 2 is

greater than the AE entropy of the waveforms acquired by pulsing waveform 3 in figure 3-6. It is evident that AE entropy is independent of acquisition threshold. Despite being independent of acquisition threshold, AE entropy was able to distinguish between the nature of the exponential modelled waveform. However, at this point it cannot be suggested that AE entropy can distinguish between the nature of the waveform originating from damages in a material. The effectiveness of AE entropy in identifying the nature of the waveform from damages is addressed in section 4.2 and 4.3.

### **4.1.1.2 Evaluation with a PLB test**

The elastic wave generated as a result of PLB was acquired by six different channel (refer to figure 3-7 for the experimental setup). Each channel captured the waveform with different threshold than the other. The influence of different acquisition threshold, on the traditional features and AE entropy are shown in figure 4-4. In order to understand the influence of threshold, linear trend-line has been added in all the graphs in figure 4-4. It is evident from the graph (a), (b), (c) and (d) of this figure that as the acquisition threshold increases, traditional features (such as Risetime, Duration, Count and Energy) extracted from the same elastic wave decreases. It is also obvious from graph (e) and (f) of this figure that the peak amplitude and AE entropy does not show any variance with the acquisition threshold and are independent of it.

During AE monitoring, multiple elastic waves can be generated in a small time frame, from different damage sources. As a result, a waveform can contain information regarding many elastic waves (many damage sources) [98]. This information can occur at a different time within the waveform. With a small threshold, traditional AE features are efficient in extracting the collective information in these waveform. However, a higher threshold can compromise the feature extraction process of these waveform and can bring difficulty in AE monitoring. Voltage values collectively define the nature of the waveform, hence, its distribution is very crucial. Although peak amplitude feature is independent of threshold, it does not take into account of the collective information from the voltage values in a waveform. Therefore, it is not efficient in identifying the nature of the waveform. Whereas, AE entropy is independent of acquisition threshold and its computation takes into account of every discrete voltage values in a waveform. As a result, the collective information in a waveform can be easily interpreted with AE entropy.

In order to further demonstrate this fact, the elastic wave (generated from PLB) captured by the first channel (with 45 dB as the acquisition threshold) was explored. This waveform is shown in graph (a) of figure 4-5. Peak amplitude feature of this waveform at its maximum voltage value and is marked with a red arrow in graph (a) of figure 4-5. It can be observed in this waveform, that the maximum voltage occurs before 100 $\mu$ s. The waveform shown in graph (b) of figure 4-5, is the waveform in graph (a), multiplied by its second standard deviation (2 times the standard deviation) and with added white Gaussian noise of SNR 10. The second standard deviation has been multiplied and SNR of 10 was added to graph (a) after 100 $\mu$ s. This was done to keep the initial peak voltage constant and vary the rest of the voltage values between the two waveform, so that the collective information between them is different.

The standard deviation of the waveform in graph (a) is 0.7875 and was calculated from the discrete voltage values according to the formula in equation 4-1. Where n is equal to 4100, this is equal to the total number of discrete voltage value in this waveform (length of waveform/sampling frequency). The  $x_i$  represents the individual discrete voltage value and  $x_{mean}$  represents the average of all the discrete voltage values of the waveform. The peak amplitude feature of the waveform in graph (b) is marked with a red arrow and is same as the one in graph (a).

$$STD = \sqrt{\frac{\sum_{i=1}^n (|x_i - x_{mean}|)^2}{n-1}}$$

Equation 4-1

Both the waveform in graph (a) and (b) has 4100 discrete voltage values. However, it can be observed in graph (b) that its discrete voltage values after 100 $\mu$ s are more spread out, compared to that of graph (a). As a result, its AE entropy is also higher: graph (a) has entropy of 8 and graph (b) has entropy of 11.

It is clear from these analyses that AE entropy not only takes into account of the collective information of the waveform, but is also independent of acquisition threshold, unlike any other traditional AE feature.

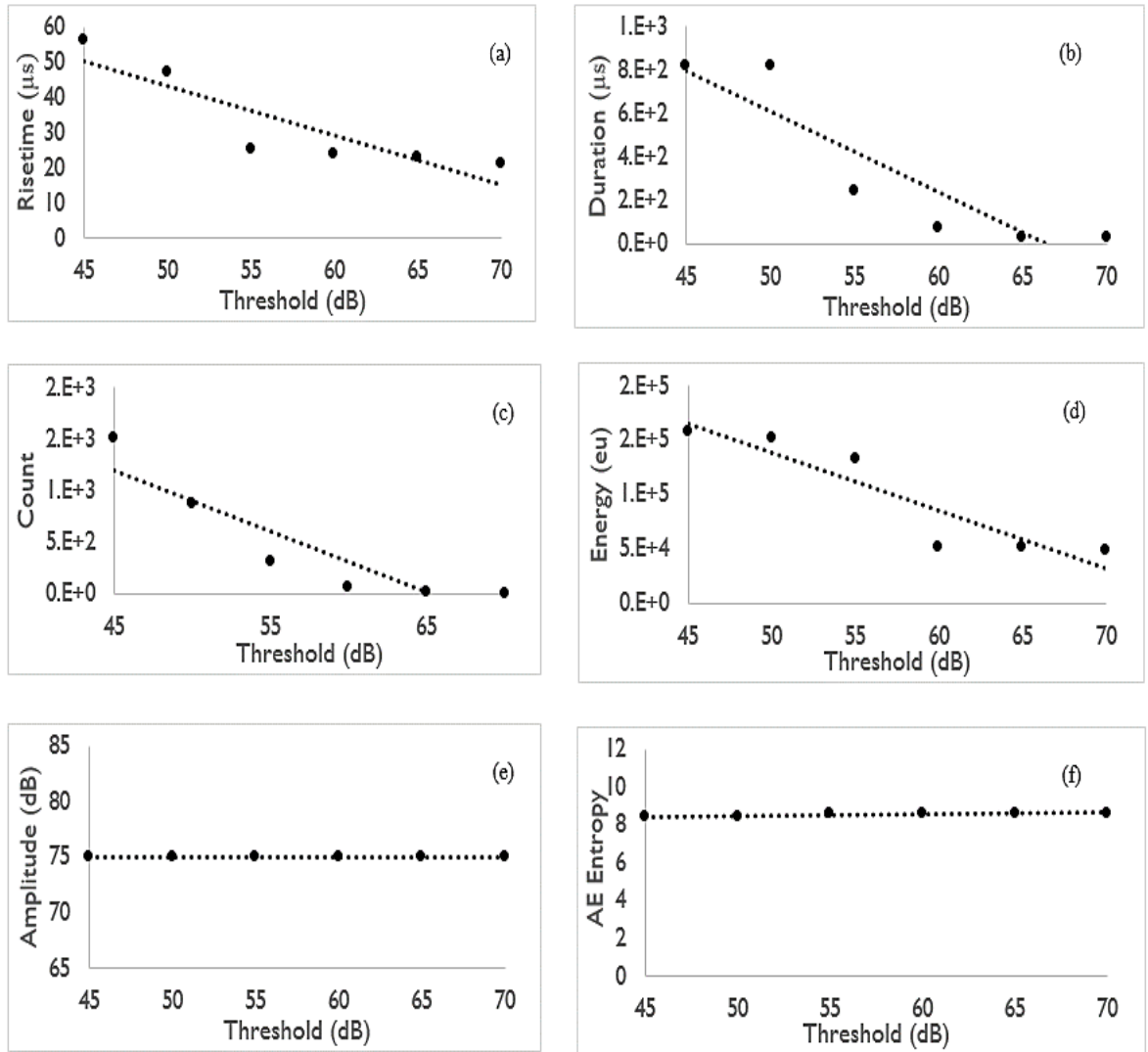


Figure 4-4: Influence of acquisition threshold on waveform generated from PLB: (a) Rise-time (b)Duration (c)Count (d)Energy (e)Peak-amplitude and (f) AE entropy

#### 4.1.2 Preformation against Hit Definition Time

This section highlights the influence of HDT on the feature extraction process of AE entropy and the traditional feature. Both modelled waveform and elastic wave generated with an AE sensor in a metal plate, has been used in this investigation.

## Results

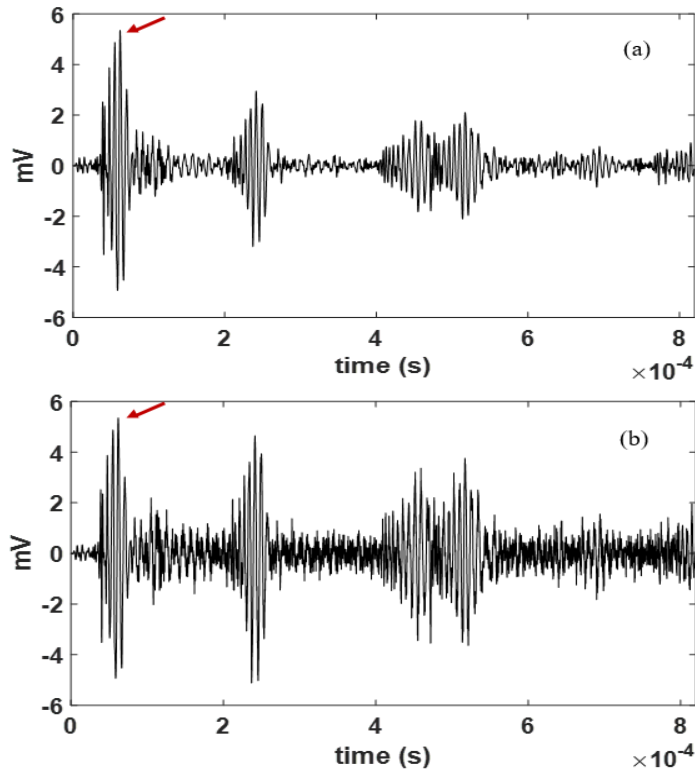


Figure 4-5: (a) Waveform recorded by the first channel (b) Waveform recorded by the first channel multiplied by 2nd standard deviation and added SNR of 10.

### 4.1.2.1 Evaluation with a modelled waveform

The waveform in figure 3-8 were acquired by the AE data acquisition system three times, with three different HDT settings. Figure 4-7 shows an acquired waveform for a HDT of  $200\mu\text{s}$ . In a FPLS, the distribution and the total number of the discrete voltage values in a waveform is not dependent on HDT. Hence, the three waveforms recorded under the three HDT's are identical. It can be observed in figure 4.6 that entire waveform has three sub waveforms. A waveform with multiple sub waveforms was chosen for this analysis, as it can appear when material emits many elastic wave in a short interval. For instance, the cyclic plastic zone extension in austenitic stainless steel can generate a waveform containing two sub waveforms[73]. An illustration of this waveform is shown in figure 4-6.

The AE entropy and the traditional AE features, for the three identical waveform acquired with three HDT's are shown in figure 4-8. A linear trend line has been added to all the graphs in this figure. The graph (a), (b), (c), (d) and (e) in this figure represents the influence of HDT on Risetime, Duration, Count, Energy and Peak amplitude of the three waveforms respectively. Although, all the three waveforms are identical, it is obvious from these graphs

that as the HDT increases, these features calculated by the AE data acquisition system also increases.

The first HDT setting has lowest values of all the recorded feature. In this setting, AE features are only calculated from the first sub waveform, from the entire acquired waveform in figure 4-6. This is because the duration from when the first sub waveform has dropped below 50dB to the onset of the second sub waveform is greater than the first HDT (200 $\mu$ s). In AE, this phenomenon is termed as the expiration of HDT. Currently in AE monitoring, features are only extracted before the expiry of HDT and the part of the waveform outside the HDT is discarded. In the second HDT setting, AE features are calculated from the first and second sub waveform. As a result, it has a higher value of Duration, Count and Energy feature. It is also evident from figure 4-8 that the Risetime and Peak Amplitude is also higher in the second HDT settings. This is because the peak voltage and its time of occurrence is calculated from within the first and second sub waveform (the second sub waveform has a higher peak voltage compared to the first one). The second HDT (300 $\mu$ s) is greater than the duration from when the first sub waveform has dropped below 50dB to the onset of the second sub waveform. However, it is smaller than the duration from when the second sub waveform has dropped below 50dB to the onset of the third sub waveform. Therefore, the second HDT has expired before the onset of the third sub waveform. Hence, the feature is extracted over a larger duration in the waveform compared to the first HDT setting. The third HDT (400 $\mu$ s) is greater than the duration between each of the pairs of waveforms (first and second, second and third). Therefore, it does not expire between the waveforms and the AE features are calculated from all three sub waveforms. As a result, the AE feature under this HDT is the largest (including the Peak amplitude and Risetime, since they are extracted from the third sub waveform which has the largest peak voltage).

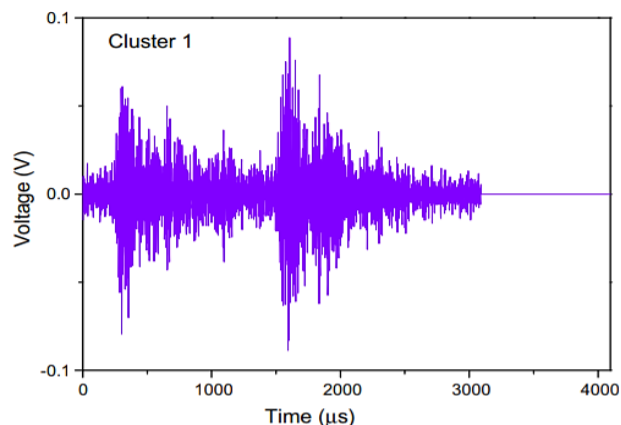


Figure 4-6: Waveform generated from cyclic plastic zone in austenitic stainless steel

## Results

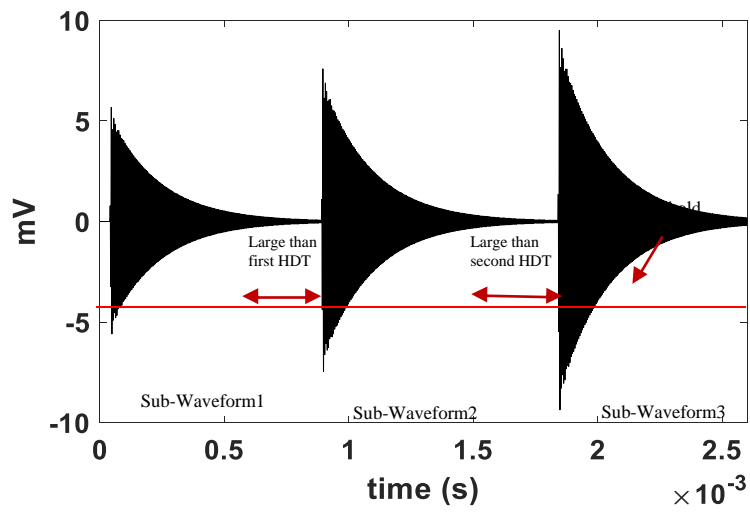


Figure 4-7: Acquired modelled waveform for HDT of 200 $\mu$ s

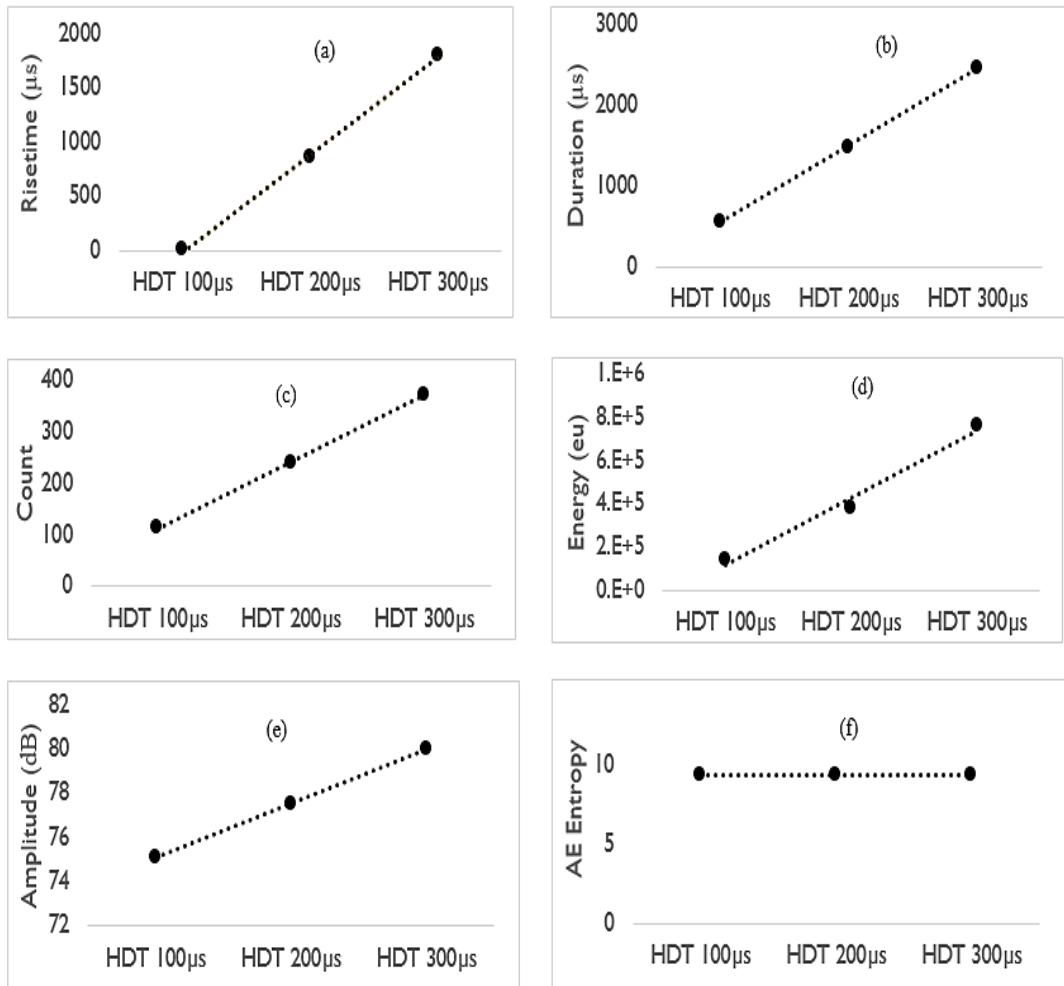


Figure 4-8: Influence of HDT on modelled waveform (a) Rise-time (b)Duration (c)Count (d)Energy (e)Peak-amplitude and (f) AE entropy

The graph (f) in figure 4-8 represents the influence of HDT on AE entropy. It can be observed from this graph that AE entropy shows no variance with HDT, unlike any other traditional AE feature. AE entropy is calculated from the distribution of the discrete voltage values. Since the distribution and the total number of discrete voltage values remains identical between the three waveforms, they all yield a same value of AE entropy.

### **4.1.2.2 Evaluation with the elastic wave generated from AE sensor**

The phenomenon in section 4.1.2.1 is investigated with an elastic wave generated in metal plate. The elastic wave was generated by exciting the metal plate with an AE sensor. The generated elastic wave was captured as analogue signal with another AE sensor attached to the metal plate (refer to figure 3-10 for the experimental setup). The analogue signal from the sensor was acquired by the AE data acquisition system three times with three different HDT settings. Figure 4-9 shows an acquired waveform for a HDT of 200 $\mu$ s. It can be observed from this figure that the peak of the first and second sub waveform is 0.5 and 0.75 times the third waveform. This corresponds well with the excitation pattern used for this test (refer to figure 3-9 for the pulsing pattern). Since, the length and nature of the waveform is not dependent of HDT, the waveform captured under all the three HDT's are identical.

The AE entropy and the traditional AE features, for the three identical waveform acquired with three HDT's are shown in figure 4-10. The graph (a), (b), (c), (d), (e) and (f) of this figure represents the influence of HDT on Risetime, Duration, Count, Energy, peak amplitude and AE entropy of the three waveforms respectively. Although the three waveforms are identical, as the HDT increases the features calculated by the AE data acquisition also increases, like in the previous section 4.1.2.1. Whereas, the AE entropy remains constant despite the change in HDT. It can also be observed from figure 4-10 (a) and (b) that the Risetime and Duration, against the three HDT's, looks identical to each other. However, the Risetime is always slightly smaller than that of the Duration for all the three HDT's. The small difference is not reflected in figure 4-10 (a) and (b).

It is clear from this analysis that AE entropy is independent of HDT. As a result, the loss of information from the sub waveforms occurring at different time interval within the waveform can be avoided with AE entropy.

### 4.1.3 Performance against disorderness

The waveform type 1, 2 and 3 in figure 3-6, each containing the SNR of 10, 20, 30 and 40 respectively, were scaled to 80.9 dB and pulsed to the AE data acquisition system. The graph (a), (b) and (c) in figure 4-11 shows the variance of AE entropy with the SNR of the acquired waveform 1, 2 and 3 respectively.

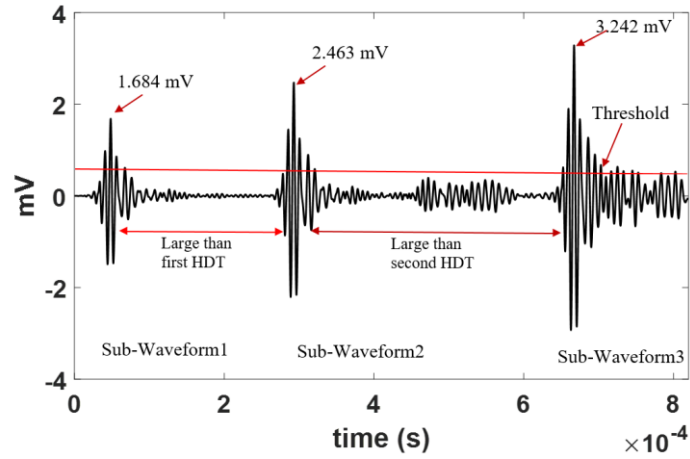


Figure 4-9: Acquired AE waveform for HDT of 200µs.

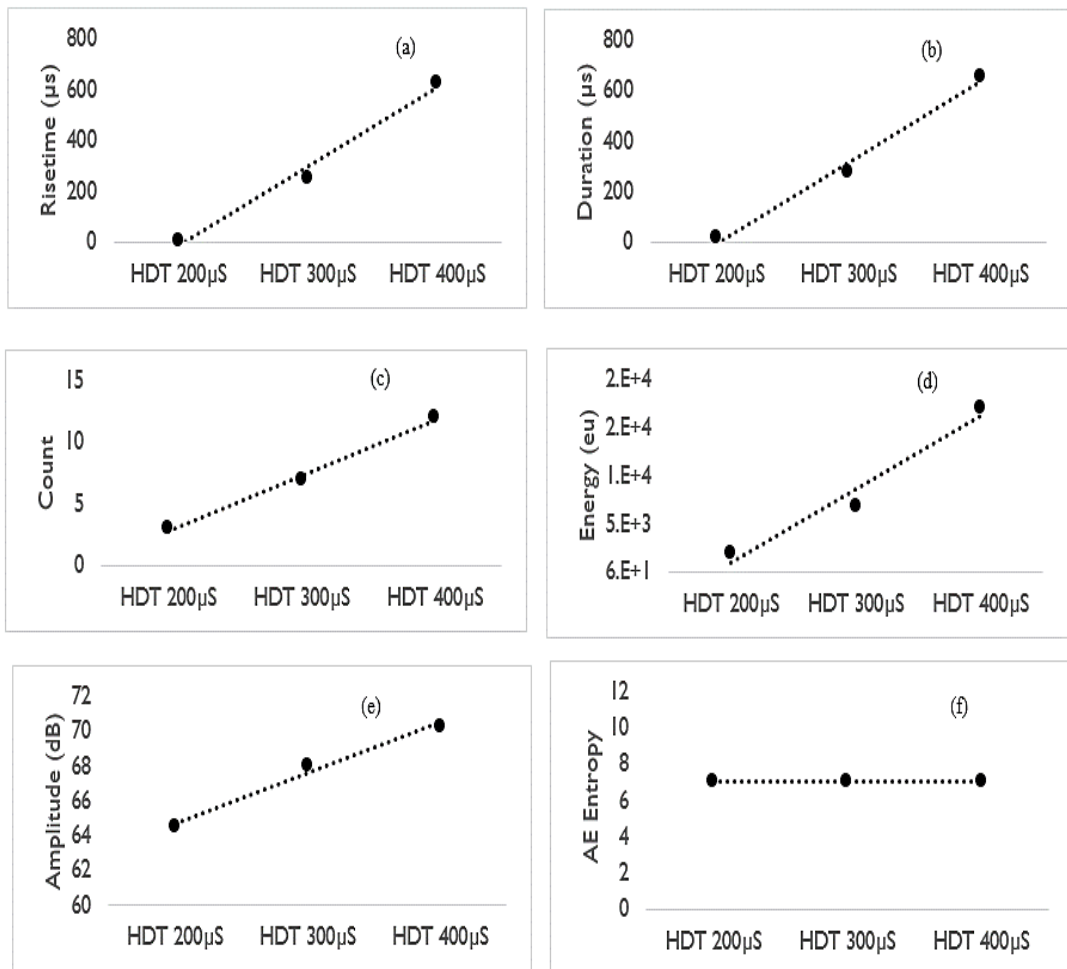


Figure 4-10: Influence of HDT on a realistic AE waveform (a) Rise-time (b)Duration (c)Count (d)Energy (e)Peak-amplitude and (f) AE entropy

## Results

A linear trend line has been added to all the graphs in this figure. It is evident from this figure that as the SNR of the acquired waveform increases, its entropy decreases. Compared to the waveform with a higher SNR, waveform with a lower SNR has a larger disorderness in its discrete voltage values. As AE entropy is a measure of disorderness in the discrete voltage values, it has a higher value when the SNR is lower.

It has been shown by Mengyu et al [100], that the waveform initiated from the damages in austenitic stainless steel is highly disordered. Since, AE entropy is sensitive to the disorderness, it has the potential to provide critical information regarding damage in austenitic stainless steel.

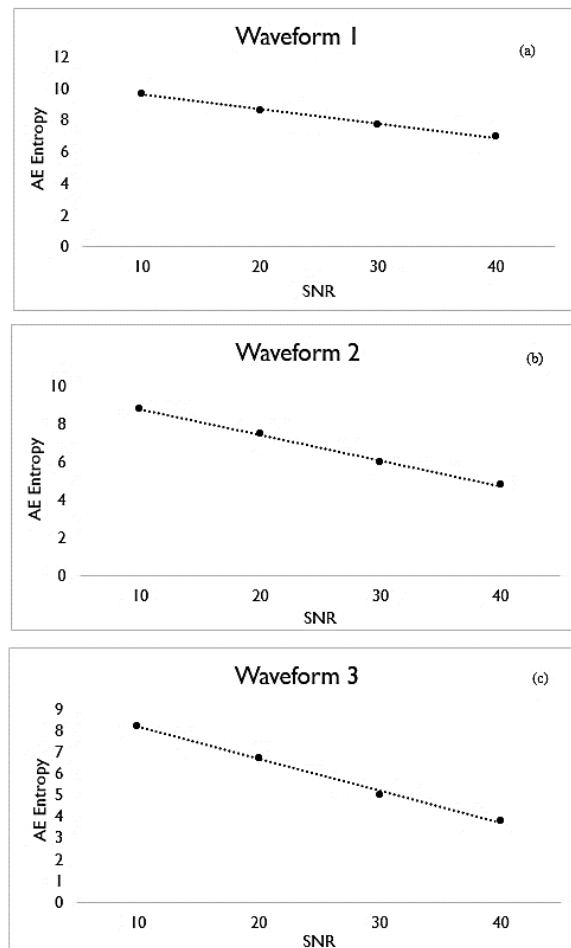


Figure 4-11: Sensitivity of AE entropy to the disorderness

## 4.2 Results of Fatigue Test

### 4.2.1 Secondary Monitoring Technique of Fatigue Test

This section highlights the information obtained regarding the time of occurrence of damages in the specimen. This information is cross validated with the AE activity that time instance.

#### 4.2.1.1 Global Strain

In this research, the global strain of the first and second specimen was monitored for the entire length of the fatigue test. Graph (a) and (b) in figure 4-12 shows the variance in the % global strain with time, from the onset of loading until failure of specimen 1 and 2 respectively. Three regions are noticeable in these graphs: a sharp increase in the % global strain at 0 second; a constant % global strain region and a sharp increase in the % global strain at the end.

The initial increase in the % global strain at around 0s in these graphs are as a result of the onset of loading. A sudden change in stress state in the specimen (0 to 480MPa), due to the onset of loading, introduces this sharp increase in % global strain at 0s in both the graphs (the initial stress is beyond the yield strength of the material, therefore, some plastic strains are also introduced in the specimen). The constant % global strain region, corresponds to the stabilization of the global strain amplitude. During this region, no changes in the specimen was visually observed. However, there may be new processes taking place in it due to continuous loading. For instance, strain could be localized (*e.g.* plastic zone) in the gauge of the specimen, towards the end of this region. The sharp increase in the % global strain at the end of these graphs are due to the ultimate failure of the specimen (separation of the specimen into two halves) and the cross head displacement after the failure of the specimen.

This secondary monitoring technique provided information regarding the onset of loading and the time of ultimate failure. However, it did not provide any information regarding the formation of plastic zone, as a result of crack initiation in the constant global strain region.

#### 4.2.1.2 Digital Image Correlation in Fatigue Test

In this research, the third and fourth specimens were monitored with DIC for the entire length of the fatigue test. There were several images taken by the DIC camera during these tests.

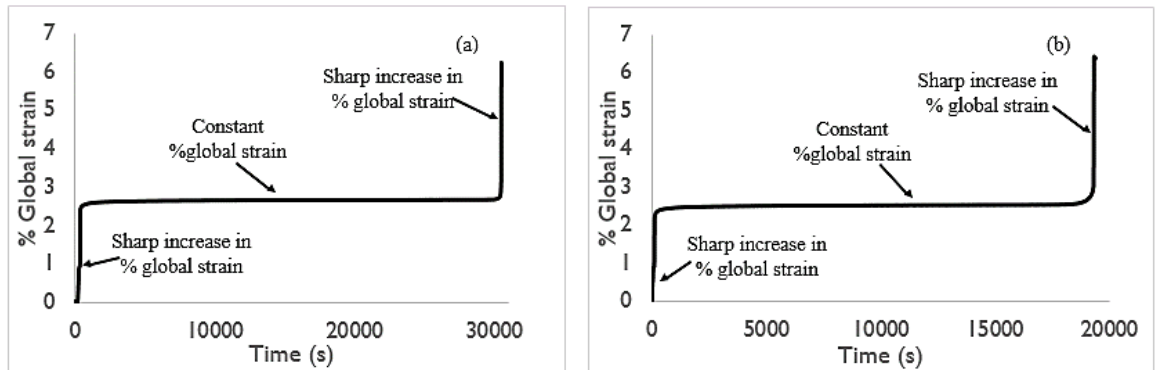


Figure 4-12: Variance of %strain with time for the entire length of fatigue test (a) specimen 1 (b) specimen 2

Figure 4-13 highlights few important DIC images of strain map ( $\epsilon_{yy}$ ) for the third specimen. Figure 4-13(a) is the reference image, this image was taken before the onset of loading. Image in figure 4-13(b) was taken at 10000s after the onset of loading, it can be observed in this image that strain maximizes at the middle of the gauge section. Image in figure 4-13(c) at 21556s does not show any difference from the image in figure 4-13(b). This suggests that the surface strain remains stable within this time. Image in figure 4-13(d) at 22911s shows that strain concentrates at the edge of the specimen forming a plastic zone (marked by a black arrow). The plastic zone at this point is likely due to significant localized formation and coalescence of micro crack. This phenomenon is explained in ref [126]. Image in figure 4-13(e) at 23250s shows an increase in the plastic zone area found at the edge of the image in figure 4-13(d) (marked by a black arrow). Image in figure 4-13(f) at 23590s shows that the plastic zone area becomes clearly highlighted (marked by a black arrow). Image in figure 4-13(g) shows a macro fatigue crack initiation from the plastic zone formed earlier (marked by a black arrow). The time instance of plastic zone localization and macro crack initiation will be cross validated with AE activity.

Figure 4-14 shows few important images of strain map ( $\epsilon_{yy}$ ) taken by DIC for specimen 4. Image in figure 4-14(a) is the reference image taken before the onset of loading. Image in figure 4-14(b) was taken 10000s after the onset of loading. Like the image in figure 4-13(b), image in figure 4-14(b) also shows strain maximization at the center of the gauge section. Image in figure 4-14(c) at 23636s does not show any difference from the image in figure 4-14(b). This suggests that there is no change in surface strain within this time. Image in figure

## Results

4-14(d) at 25084s shows slight changes in the strain map of the gauge section as compared to the image in figure 4-14(c). Image 4-14(e) at 25265s shows two strain concentrated area (*i.e.* marked by black arrows). The formation of two strain concentrated area could be a result of the plastic zone formed (by the crack initiation) on the other side of the specimen, which is not covered by the DIC camera. This is very likely because the thickness of the specimen was very small (2.5mm). A study was performed, on the damage identification from DIC measurement, during low cycle fatigue of austenitic stainless steel [127]. This study suggests that there is always a possibility for the damage to initiate on the other side of the specimen, which is not observed by the DIC camera.

The formation of two strain concentrated area becomes evident in figure 4-14(f) at 25446s (*i.e.* marked by black arrows). Image in figure 4-14(g) at 25627 shows a crack initiation from the middle of the two strain concentrated area. The time instance of the strain concentration will be cross validated with AE activity.

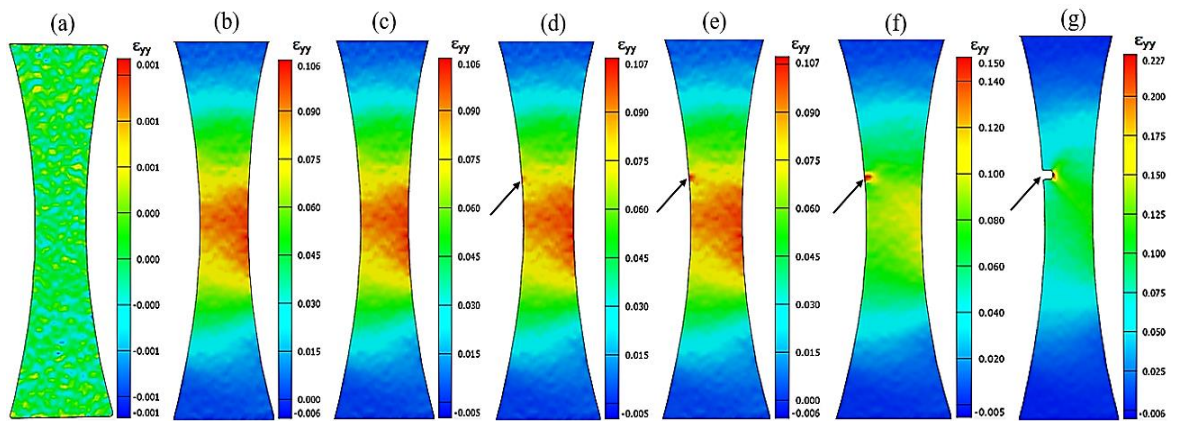


Figure 4-13: DIC Images of specimen 3: (a) Reference stage (b) at 10000s (c) at 21556s (d) at 22911s (e) at 23250s (f) at 23590s (g) at 23928s

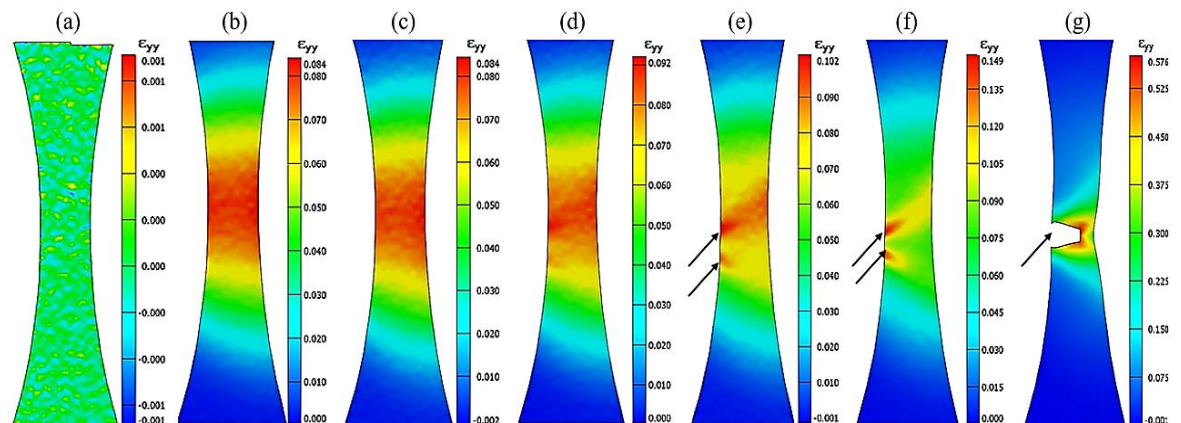


Figure 4-14: DIC Images of specimen 4: (a) Reference stage (b) at 10000s (c) at 23636s (d) at 25084s (e) at 25265s (f) at 25446s (g) at 25627s.

### 4.2.2 AE Data Filtration

Graph (a), (b), (c) and (d) in figure 4-15, shows the cumulative count of the unfiltered AE event, captured during fatigue test of specimen 1, 2, 3 and 4 respectively. It is mentioned in [76][77][78] that cumulative trend during the fatigue of standard specimen, remains stable in the early stages and increases at the later stages of loading. It can be observed in these graphs that no such trend as mentioned in [76] [77][78] can be identified. 1D linear localization filtration technique mentioned in section 3.2.1.2 were applied to these unfiltered AE events. Graph (a), (b), (c) and (d) in figure 4-16, shows the cumulative count of the filtered AE event. It can be observed in these graphs that the cumulative count remains stable in the early stages and begins to increase during the later stage of loading. The trend observed in these graphs are consistent with the findings of other researchers [76] [77][78].

It can be concluded that the filtration technique had a significant effect in de-noising the data set because the filtered event of cumulative count possesses the same trend as those mentioned in the literature. After filtration, AE entropy was computed on the remaining data set and compared with the traditional AE features.

### 4.2.3 Correlation of AE monitoring with global strain.

The global strain of the first and second specimen was monitored for the entire length of the fatigue tests, alongside AE monitoring. These tests were carried out until fracture of the specimens. Figure 4-17 shows the specimens at the end of the tests. The traditional features and AE entropy of the filtered events, captured during the test on the first and second specimens are shown in figure 14-18 and 14-19 respectively. Graph (a), (b), (c), (d), (e) and (f) of these figures represents the variance of Risetime, Duration, Count, Energy, Peak-Amplitude and AE entropy for the entire length of the test. The global strain for the first and second specimen is superimposed in each of the graphs in figure 14-18 and 14-19 respectively.

It is evident in graph (c), (d), (e) and (f) of both the figure that at the initial and final stage (*e.g.* at the beginning and end of the test), there is a significant increase in Count, Energy,

## Results

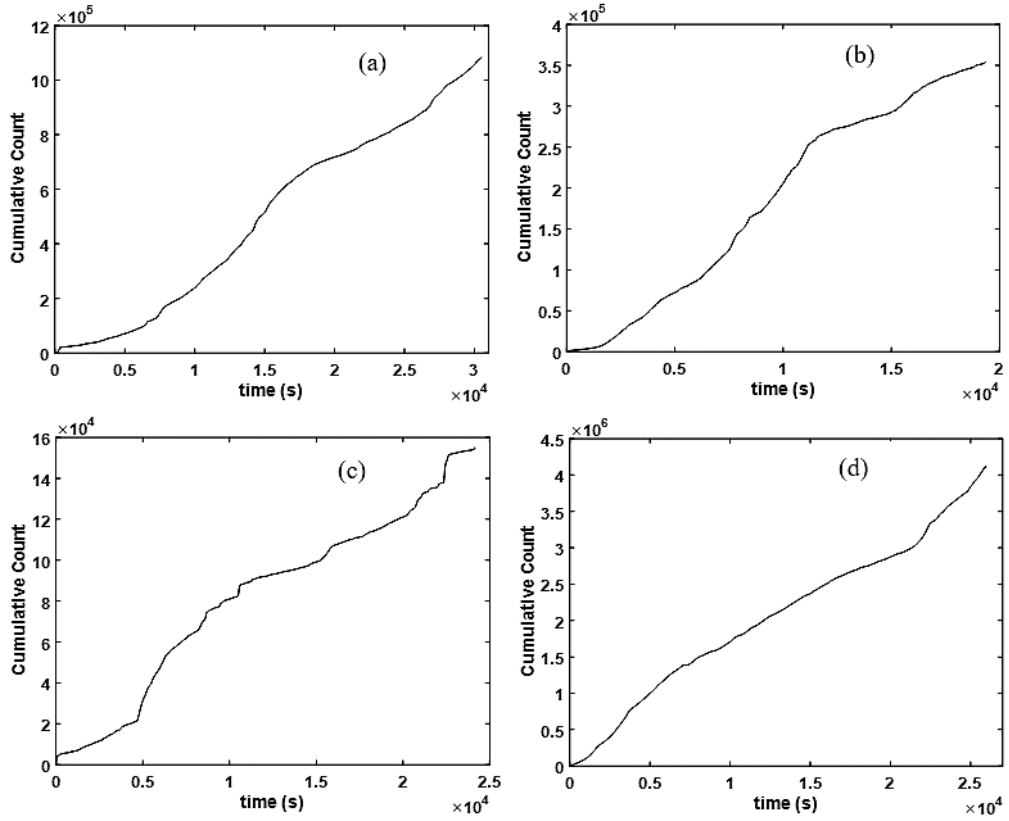


Figure 4-15: Unfiltered cumulative count of the AE event captured during fatigue test of: (a) Specimen 1, (b) Specimen 2, (c) Specimen 3 and (d) Specimen 4

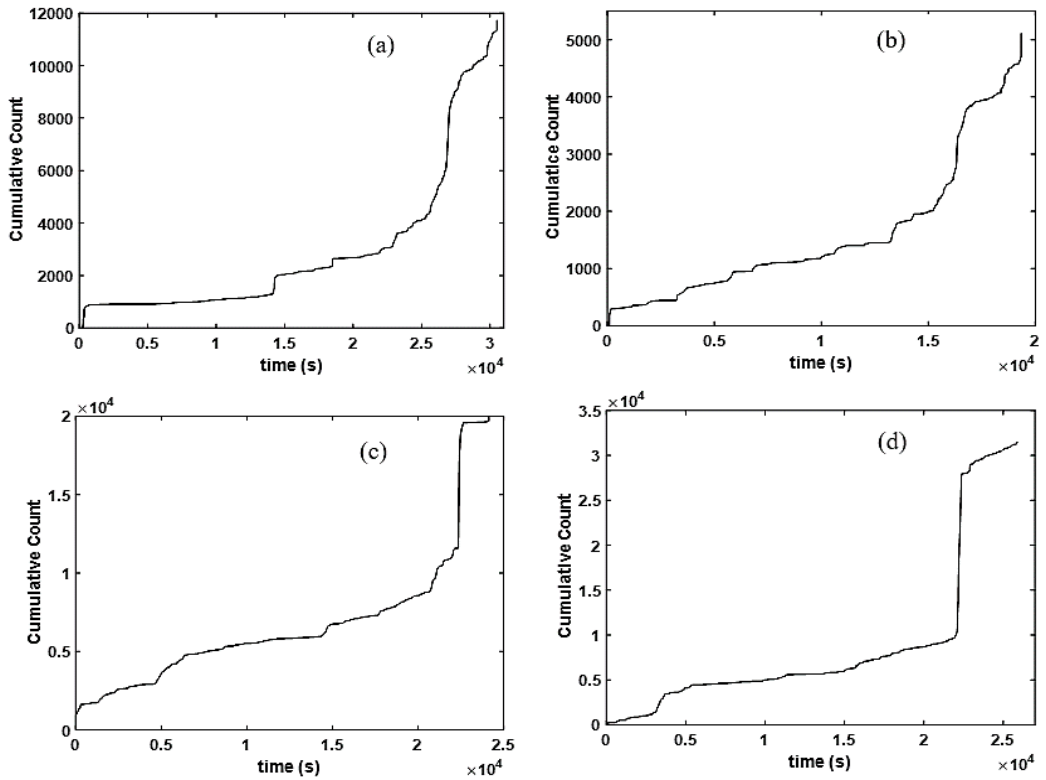


Figure 4-16: Filtered cumulative count of the AE event captured during fatigue test of: (a) Specimen 1, (b) Specimen 2, (c) Specimen 3 and (d) Specimen 4

## Results



Figure 4-17: a) First specimen at the end of test (b) Second specimen at the end of test.

Peak-amplitude and AE entropy. In both the test, the initial and final stage is accompanied with AE entropy of above 10. The initial increase in these traditional features and AE entropy is due to the rapid yielding caused by the onset of loading. The maximum engineering stress exerted on the specimen at each cycle of loading (including the first cycle) is 480MPa. This is beyond the yield stress of the material. As a result, yielding was introduced in the specimen in the first cycle of loading. Yielding in austenitic stainless steel has been reported to be accompanied by the sharp increase in some traditional AE features (e.g. count and Peak-amplitude) [39][36][37][35][34]. The increase in the traditional features and AE entropy at the final stage is due to the fracture of the specimen. The fracture of specimen has been reported to generate AE events with enhanced traditional features[98]. It is clear from these results that like the traditional features, AE entropy is also sensitive to the yielding and fracture of austenitic stainless steel. Since the specimens are subjected to fatigue loading, fatigue crack initiation leads to its fracture [128]. The secondary monitoring technique used in these tests is unable to provide any information regarding the time instant of fatigue crack initiation. It is mentioned in [76] [78], that before the fracture period (approximately 10% of the remaining life), fatigue crack starts to initiate. However, it can be observed from these graphs that apart from yielding and fracture, there is no noticeable increase in these traditional features and AE entropy for both the test. Therefore, there is a possibility that the AE entropy along with these traditional features may not be sensitive to fatigue crack initiation.

## Results

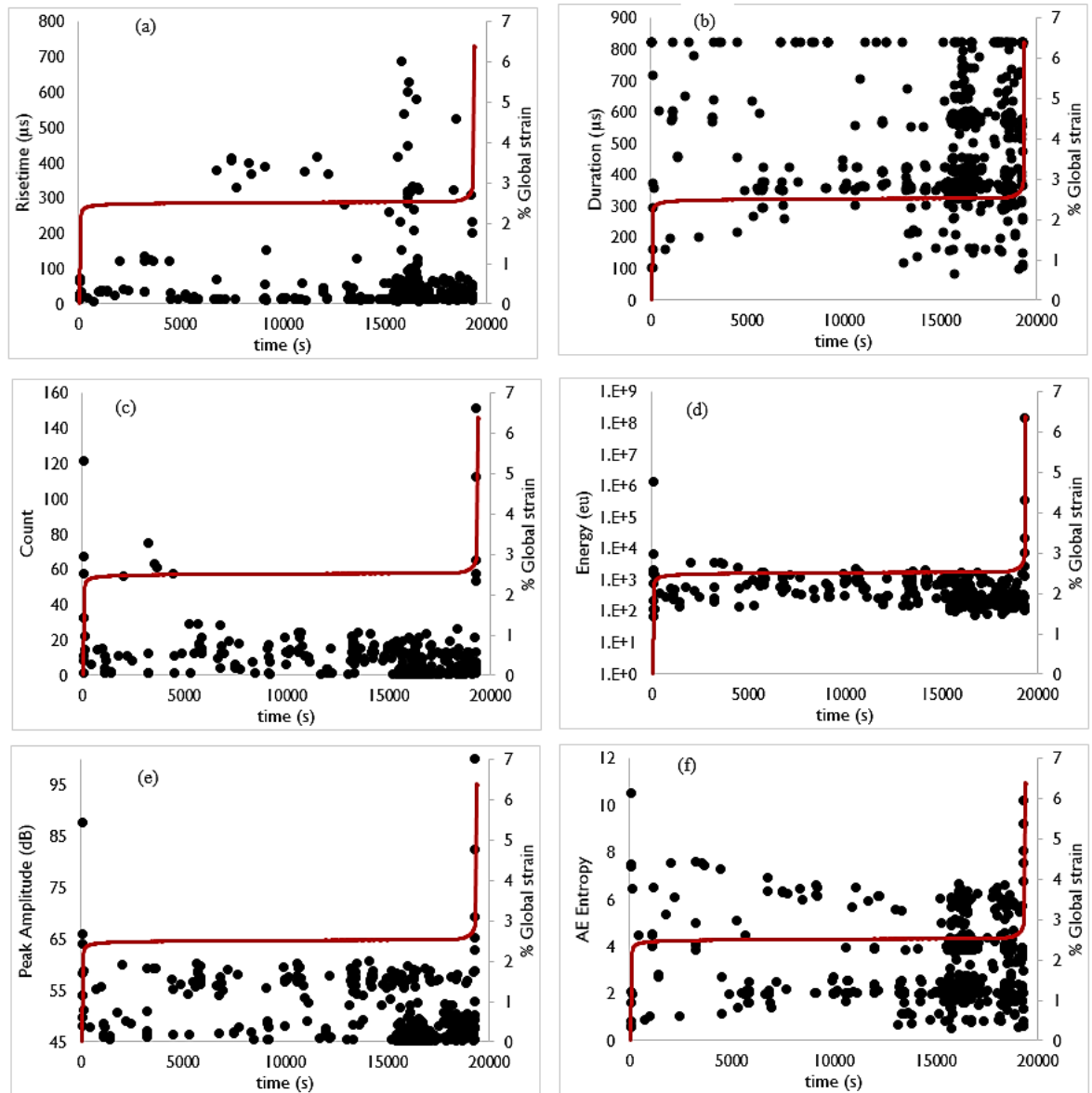


Figure 4-18: Variation of AE features with time for the first specimen (a) Rise-time (b)Duration (c)Count (d)Energy (e)Peak-amplitude and (f) AE entropy

It can be observed in graph (a) of both the figure that the Risetime of the event begins to increase towards the end of fracture on both the test. It is mentioned in [73][129] that burst type AE waveform have a shorter Risetime, whereas a continuous one has a longer Risetime. A continuous waveform is formed due to the superposition of many sub burst waveforms [130][131]. The increase in Risetime towards the end of both the tests indicate that more AE events with continuous waveforms were being recorded. The combinations of the small burst waveforms generated within a small time interval, due to growth and coalesce of micro cracks may be the origin of these continuous waveforms. However, the formation of plastic zone towards the end of fracture could also be responsible for these continuous waveforms with large Risetime [129]. It can be observed in graph (b) of both the figure that the Duration

## Results

of the events does not provide any information regarding damages. Typically, waveforms with highest Peak-amplitude has the longest duration[73]. Therefore, the Duration of the events during the initial and final stage was expected to be significantly higher (since the Peak-amplitudes are higher). However, these stages were accompanied by events which had durations identical to the whole process (*i.e.* the entire fatigue life). One of the reason for this observed trend in the variation of Duration is a small FPLS (*e.g.* 820  $\mu$ s). The small FPLS have limited the length of the waveform over with the Duration could be extracted.

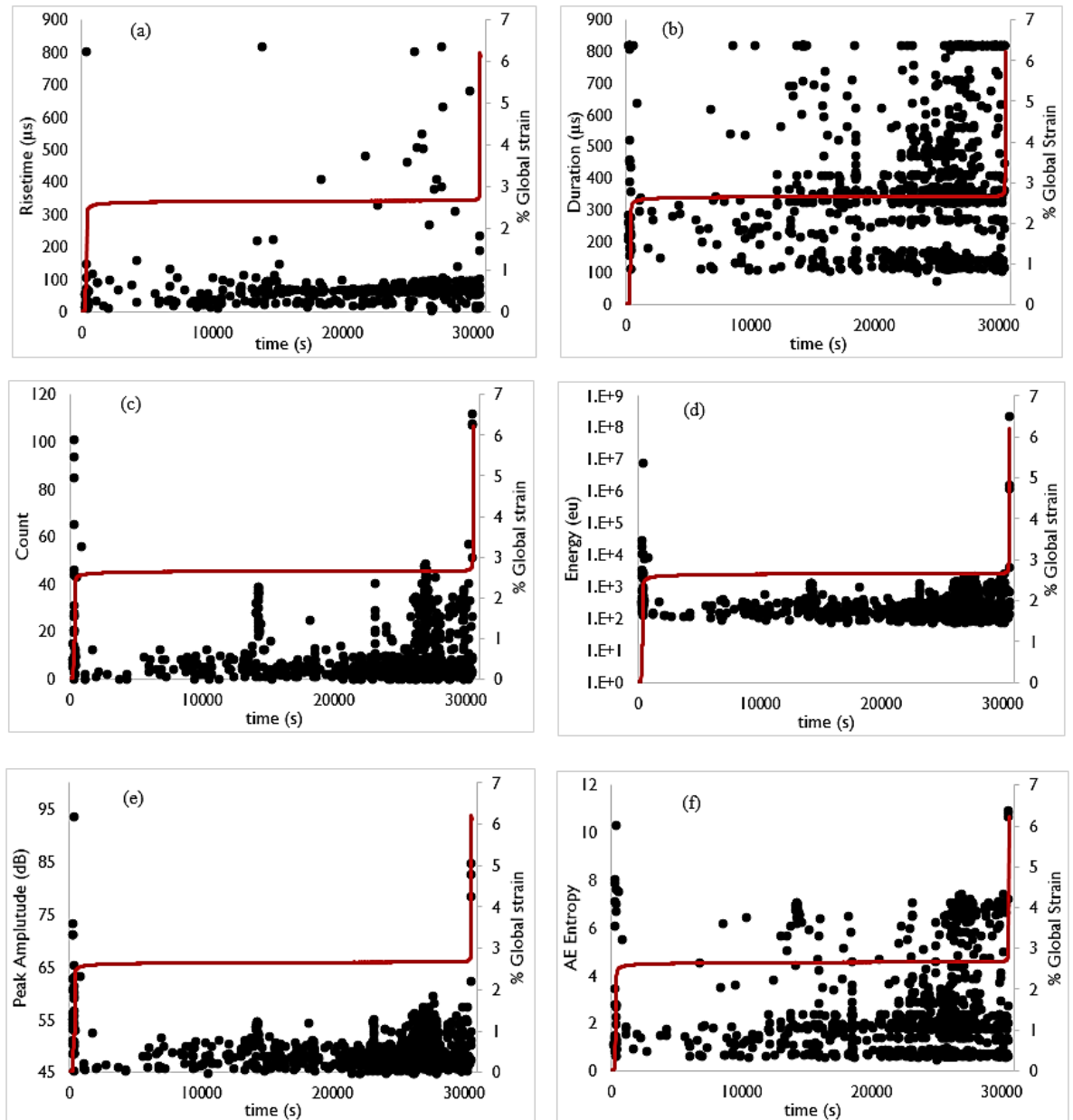


Figure 4-19: Variation of AE features with time for the second specimen (a) Rise-time (b)Duration (c)Count (d)Energy (e)Peak-amplitude and (f) AE entropy

## Results

Fatigue studies using AE are mostly based on the cumulative analysis of energy and count [76] [72] [73][77]. Therefore, the cumulative trend in AE entropy was compared with these features. Figure 4-20 and 4-21 shows the comparison of the cumulative trends for the first and second specimen respectively. The cumulative trend of the AE entropy and the traditional features in figure 4-20 and 4-21 were computed from the filtered AE events. It can be observed from these figures that the yielding there is accompanied by a small increase in the cumulative energy. Whereas, at the fracture of the specimen there is a significant increase in the cumulative energy. In the rest of the period between the yielding and fracture, there is no noticeable increase in the cumulative energy. This is because a few highly energetic waveforms generated at the fracture masks the collective cumulative trend in energies prior to the fracture. It is evident from these figures that cumulative AE entropy and count exhibit the same trend during the entire test of the first and second specimen. Unlike cumulative energy, these cumulative trends begin to increase noticeably towards the end of the test (prior to the fracture of the specimen). It has been reported in [76][77][78][79], that towards the end of fracture of an un-notched specimen subjected to fatigue loading, there is a significant increase in the count. This significant increase in count is attributed to the growth and coalesce of micro crack and plastic zone formation. Therefore, the increase in the cumulative trend in count and AE entropy towards the end of these figures could be a result of the damage mechanism mentioned in [76] [77][78][79].

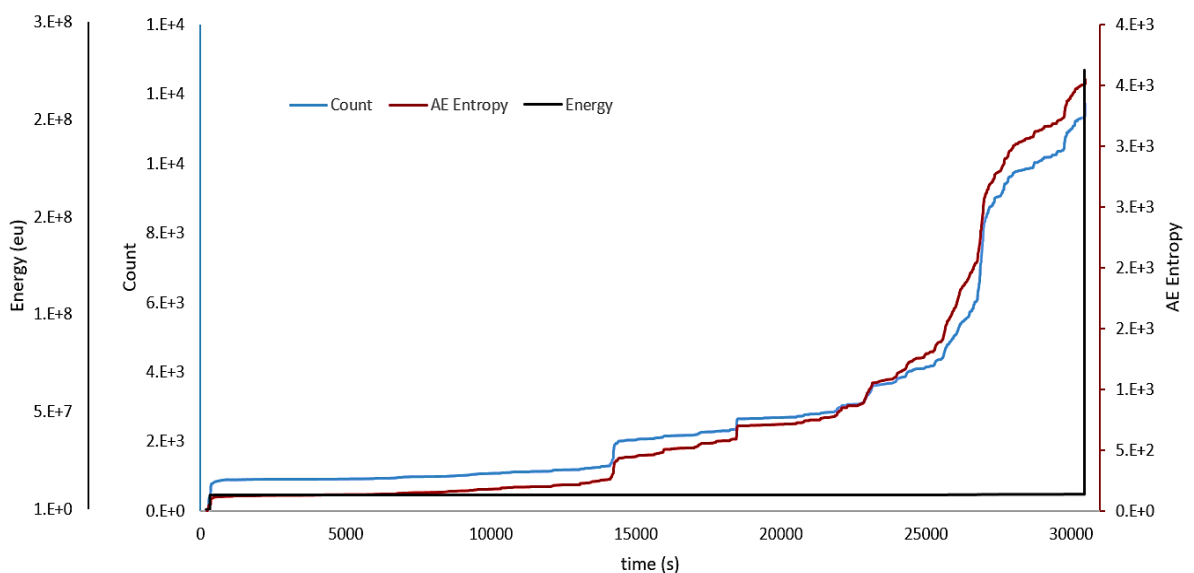


Figure 4-20: Comparison of cumulative feature for the first specimen

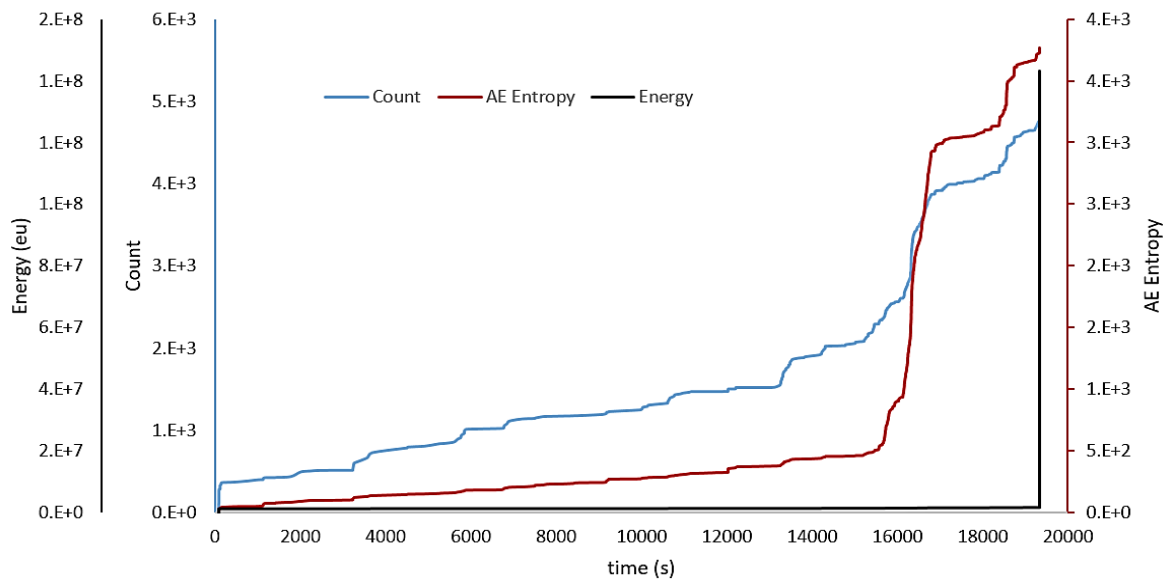


Figure 4-21: Comparison of cumulative feature for the second specimen

Based on the cumulative trend, it is evident from the first and second fatigue test that count and AE entropy is equally good indicator in identifying damages. However, AE entropy is independent of threshold and HDT, unlike the count. As a result, can identify damages at reduces human involvement with the data acquisition system. However, the secondary monitoring technique used in these tests does not provide any information of failure that precedes fracture. Therefore, the increase in the cumulative count and AE entropy towards the end, as a results of the damage sources mentioned in the literature cannot be justified. In order to successfully extract the information of failure that precedes fracture and approximate its time of occurrence, the next couple of test is carried out with simultaneous DIC monitoring.

#### 4.2.4 Correlation of AE monitoring with DIC for fatigue test

The third and fourth specimen was simultaneously monitored with DIC and AE for the entire length of the fatigue test. The third specimen was tested until fracture. Whereas the test on the fourth specimen was interrupted just before fracture (after a crack was visible towards the end of the test). This was done to investigate the behaviour of AE entropy and some traditional feature at the end of the test, when the specimen has not fractured. Figure 4-22 below shows the specimens at the end of the test. The traditional features and AE entropy of the filtered events, captured during the tests on third and fourth specimens are shown in

## Results

figure 4-23 and 4-24 respectively. Graph (a), (b), (c), (d), (e) and (f) of these figures represent the variance of Risetime, Duration, Count, Energy, Peak-Amplitude and AE entropy for the entire length of these test.



Figure 4-22: (a) Third specimen at the end of test (b) Fourth specimen at the end of test.

It is evident from graph (c), (d), (e) and (f) of both the figures that the initial stage is accompanied by a significant increase in Count, Energy, Peak-amplitude and AE entropy. This observation is consistent with the previous tests (*e.g.* first and second test) test. Like the previous test, the noticeable increase in these features are from rapid yielding as a result of the onset of loading. It can be observed in graph (c), (d), (e) and (f) of figure 4.23 that at the final stage, there is a significant increase in Count, Energy, Peak-amplitude and AE entropy. This increase, like the previous test, is associated with fracture of the specimen. It can be observed in figure 4-24, that there was no significant increase in these traditional features and AE entropy in the final stage. Unlike the first three tests, this test was interrupted before the specimen fractured, as a result it did not produce AE events with enhanced traditional features and AE entropy at the end. Therefore, these observations confirm that the significant increase in the traditional features and AE entropy at the end of the test in first, second and third specimen is from fracture. It is also justified that both the yielding and fracture of austenitic stainless steel is associated with an AE entropy of above 10.

It is a well-known fact that fatigue crack initiation leads to plastic zone formation in the specimen [76] and the crack propagates until the final fracture [128]. The DIC as a secondary

monitoring technique used in the third and fourth test was able to identify the onset of plastic zone formation (refer to figure 4-13 and 4-14). The onset of plastic zone formation in third and fourth specimen, identified by DIC, is marked with a red dashed line in each of the graph of figure 4-23 and 4-24 respectively. It can be observed in graph (c), (d), (e) and (f) of both the figure that there is no noticeable increase in Count, Energy, Peak-amplitude and AE entropy at the onset of plastic zone formation. In fact, apart from yielding and fracture, there is no noticeable increase in these traditional AE features and AE entropy. This observation is consistent with the previous two specimens.

It has been reported in [73] [77][129], that the formation of plastic zone in austenitic stainless steel is associated with AE waveforms with high Risetime. It can be observed in graph (a) of both these figures that around the onset of plastic zone formation there is a noticeable increase in the Risetime. This increase in Risetime can be regarded from the plastic zone formation. It can be observed in graph (b) of both the figures that the Duration of the events does not show any trend. The duration of events during the initial yielding and final fracture was expected to be higher (since these events had a higher Peak-amplitude). However, no distinct increase in Duration could be observed at during these stage. Like the previous tests, a small FPLS (*i.e.* 820  $\mu$ s) used for these tests, masked the performance of Duration. This behaviour in Risetime and Duration is consistent with the previous two specimens.

Figure 4-25 and 4-26 shows the comparison of the cumulative trends for the third and fourth specimen respectively. The cumulative trends in these figures are calculated from the filtered AE events captured during the test. In the fatigue test, yielding occurred in the specimen as a result of the onset of cyclic loading (as peak load in the cycle was 480Mpa, which is greater than the yield stress of the material), whereas, plastic zone is formed in the specimen towards the end, prior to the fracture, due to repeated cyclic load. In the third fatigue test the plastic zone is formed at 22911s and in the fourth fatigue test plastic zone is evident at 25265s. It can be observed in figure 4-25 that in the beginning of the test (just after 0s) there is a small increase and at the end there is a significant increase in the cumulative energy. The increase in the cumulative energy in the beginning is attributed to the yielding as a result of the onset of loading. Whereas, the significant increase in the cumulative energy at the end is due to fracture of the specimen. The plastic zone identified by DIC for this test is at 22,911 seconds. However, there was no significant change observed in the cumulative energy at that time. In fact, in the period between the yielding and fracture of the specimen there is no noticeable

## Results

increase in the cumulative energy. Few highly energetic AE events towards the end may have masked the cumulative trend in energy between yielding and fracture. It is clear from this figure that cumulative entropy and cumulative count exhibit the same trend during the entire test of the third specimen. This figure shows that at around 23000s, there is a significant jump in all the cumulative features. This time is associated with the plastic zone formation in the DIC images shown in figure 4-13. Therefore, it can be concluded that the significant jump in AE activity is an indicator of plastic zone formation. This figure also shows that cumulative features (especially count and entropy) begins to increase slightly after 15000s and noticeably after around 20000s. DIC images in figure 4-13 does not show any change in surface strain until 21556s. The noticeable increase in cumulative features from around 20000s could be as a result of growth and coalescence of micro-crack, before it manifests into plastic zone formation. Therefore, it can also be concluded that AE is more sensitive than DIC for damage identification. The merit of the sensitivity of AE over other NDT technique has been shown by other researchers [72][125].

It is clear from figure 4-26 that both the cumulative count and AE entropy exhibits the same trend during the test of the fourth specimen. This figure shows that there is a significant jump in all the cumulative features (Count, Energy and AE entropy) at around 22500s. No significant changes can be observed in the DIC images during this time in figure 4-14. In fact, no significant changes are observed in the DIC images until 25265s. At 25265s, DIC images in figure 4-14 shows two distinct strain concentration which becomes clearer at 25446s. The two distinct strain concentration could appear as a result of crack initiation on the other side of the specimen which is not observed by the DIC camera. It can be observed in image (g) of figure 4-14, that the specimen is separated (large crack is formed) from between the two distinct strain concentrated area identified by DIC. This suggests that the plastic zone and the crack was initiated between the strain concentrated area, on the other side of the specimen which is not observed by the DIC camera. A study on damage identification in austenitic stainless steel using DIC, suggested that it is not always possible to identify the exact damage initiation site using DIC. These study also suggests that a damage initiation time instant has to always be confirmed by AE. The significant jump in cumulative features at around 22500s confirms that the plastic zone formation was on the other side of the specimen which is not monitored by the DIC camera. Cumulative parameter (especially count and entropy) begins to increase noticeably from around 15000s, this could be attributed to growth and coalescence of micro-crack.

## Results

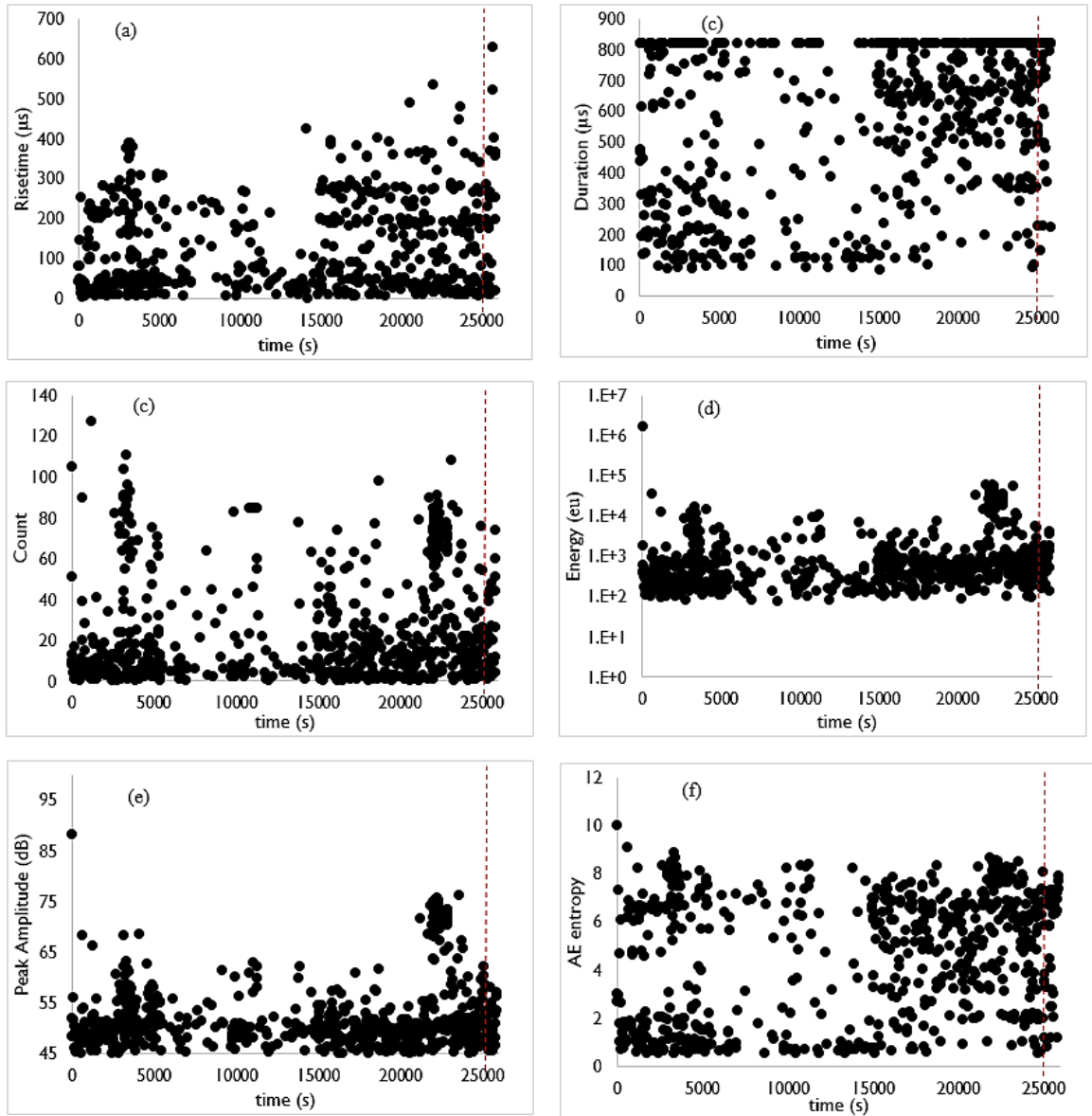


Figure 4-23: Variation of AE features with time for the third specimen: (a) Rise-time (b)Duration (c)Count (d)Energy (e)Peak-amplitude and (f) AE entropy

It is interesting to note that unlike the first, second and third specimen, there is a significant increase in the cumulative energy in the fourth specimen towards the end of the test in figure 4-26 (before it could fracture). One of the reason for this is because the fourth test was interrupted before the specimen could fracture. Therefore, the energetic AE events due to fracture, which can cause the significant jump in cumulative energy was absent from this test. The absent of significant increase in cumulative energy towards the end (due to fracture) of the test on fourth specimen, did not mask the its cumulative trend at the onset of plastic zone formation.

## Results

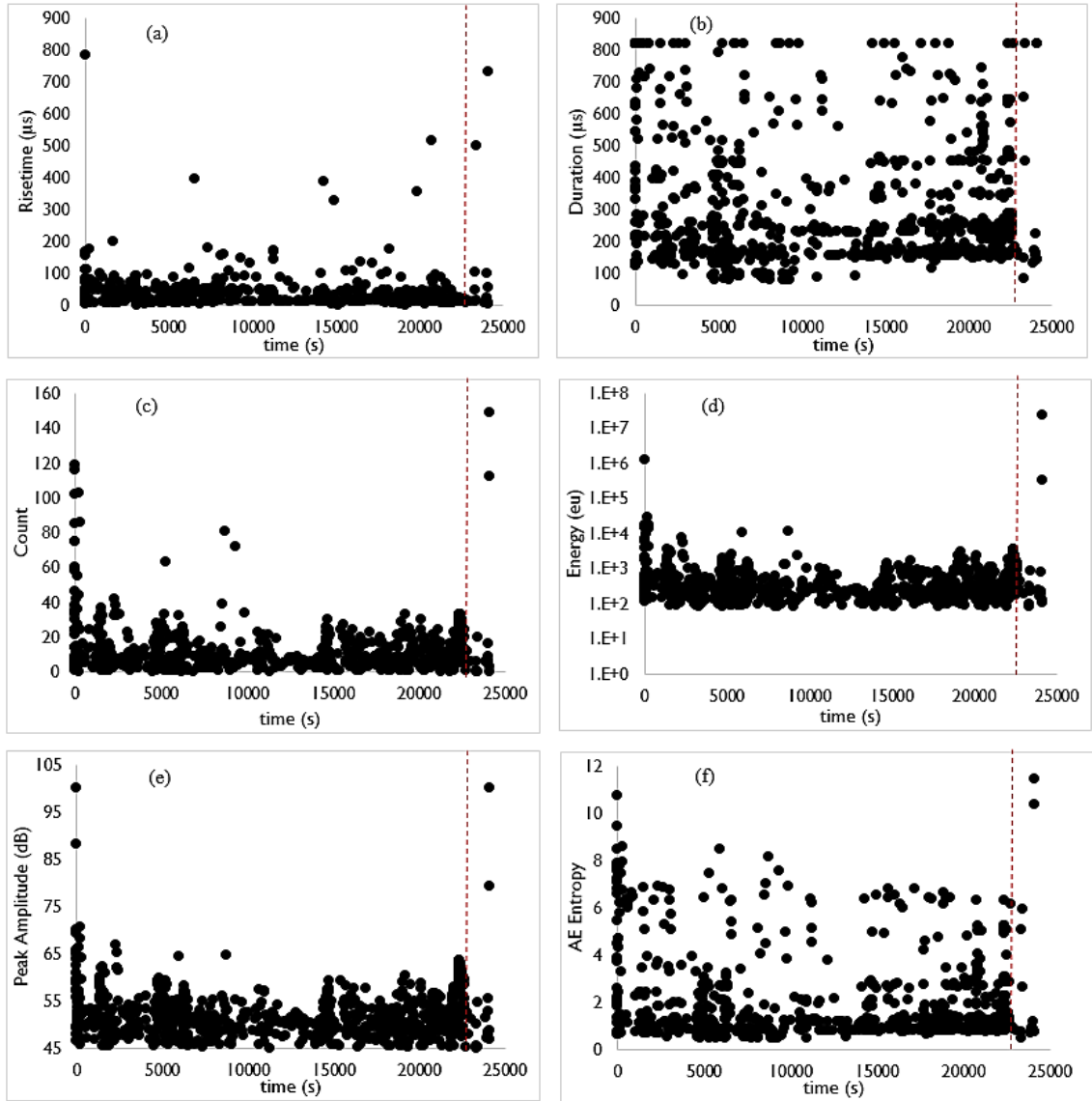


Figure 4-24: Variation of AE features with time for the fourth specimen: (a) Rise-time (b) Duration (c) Count (d) Energy (e) Peak-amplitude and (f) AE entropy

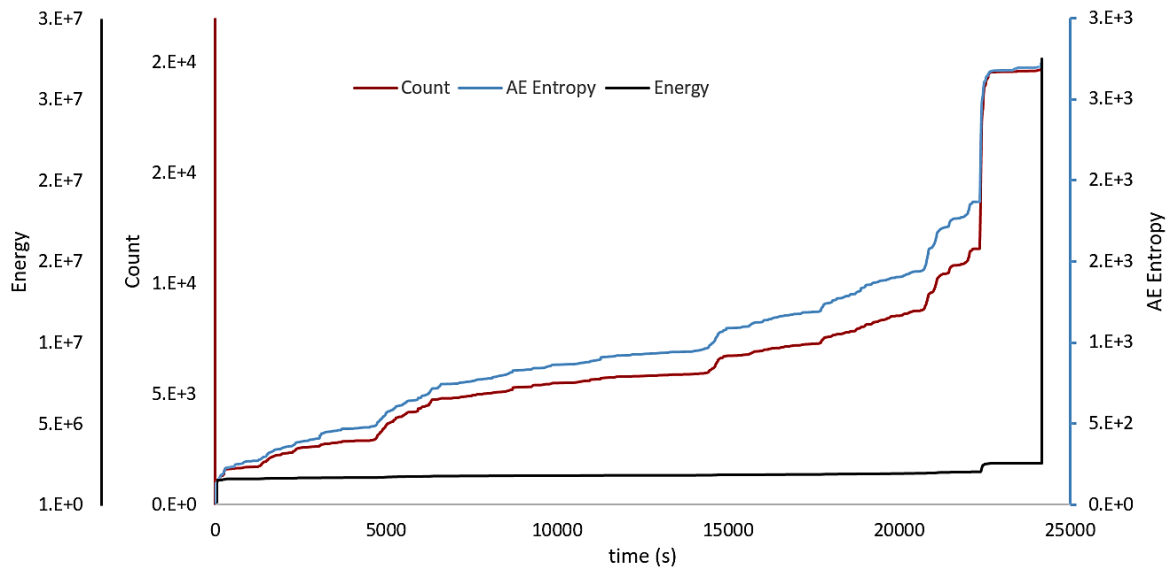


Figure 4-25: Comparison of cumulative feature for the third specimen

## Results

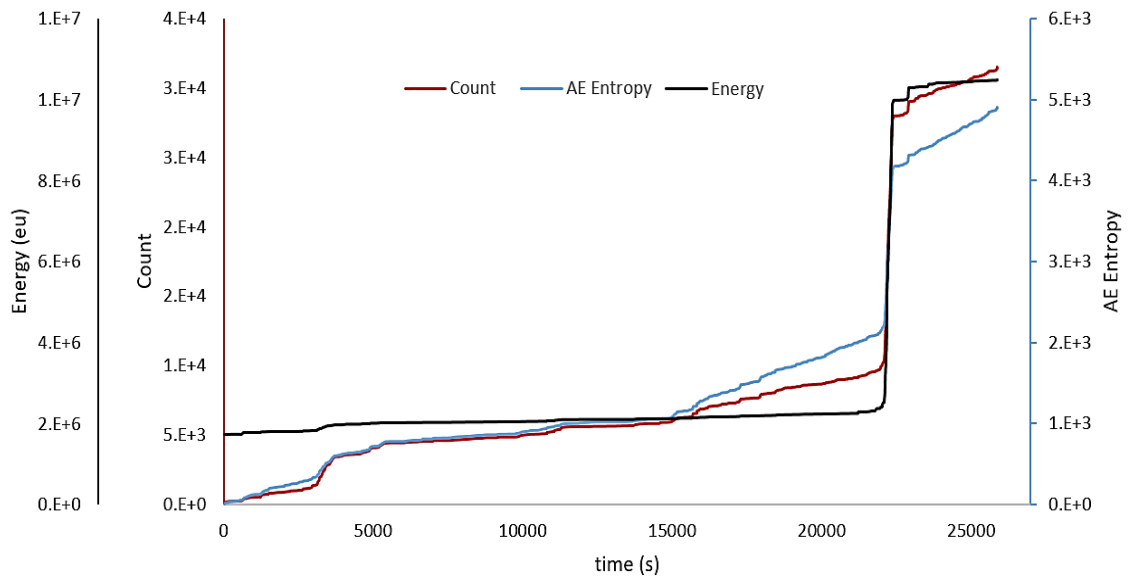


Figure 4-26: Comparison of cumulative feature for the fourth specimen

## 4.3 Results of Tensile Test

### 4.3.1 Secondary monitoring technique of tensile test

This section highlights the material behaviour as a result of loading. The material behaviour extracted from this section will be cross validated with AE activity.

#### 4.3.1.1 Strain extraction with Digital Image Correlation.

In this research the gauge length of all three tensile specimens was monitored with DIC for the entire length of the test. There were several images taken during the test. Figure 4-27 and 4-28 highlights a couple of DIC images of displacement maps for an un-notched and notched specimen respectively.

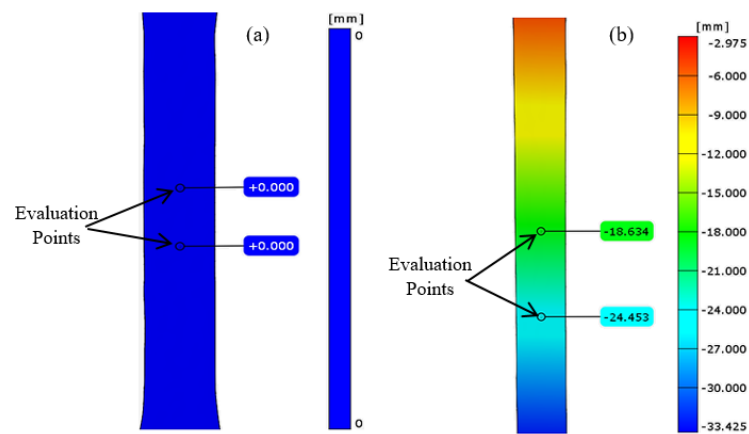


Figure 4-27: Images of displacement fields of a un-notched specimen (a) Reference stage (b) Prior to the onset of yielding

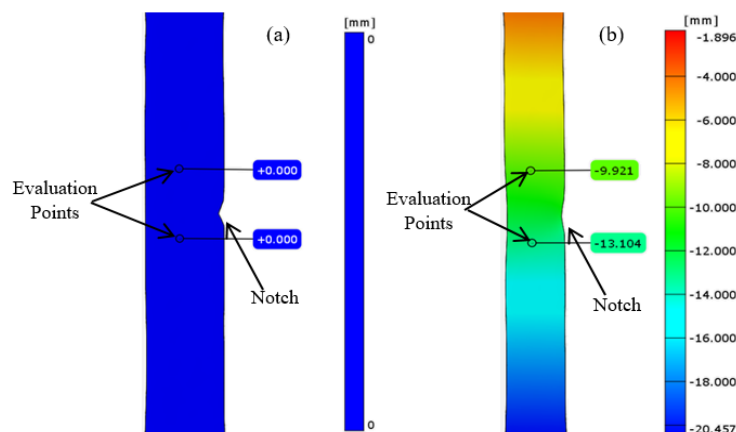


Figure 4-28: Images of displacement fields in the notched specimen (a) Reference stage (b) Prior to the onset of yielding

Image (a) in these figures corresponds to the state of the displacement maps, in the gauge section, before the onset of loading. This image is regarded as the reference image. Image (b) in these figures represents the state of the displacement maps, in the gauge section, prior

to the onset of yielding. The evaluation points in each of the images is marked with arrows. The reading of the evaluation points represents its displacement. It can be observed in image (a) of these figures that all the evaluation points had a zero reading. This image was taken before the onset of loading, as a result there was no displacement introduced in the specimen at the time. The distance between the evaluation points in each of the image (a) are 10mm. As the specimens are extended (as a result of loading), the displacement reading in the evaluation points increases. For instance, the displacement reading of the evaluation points in image (b) of figure 4-27 are -18.634 and -24.453 respectively and in image (b) of figure 4-28 are -9.921 and -13.104 respectively. The difference in displacement readings between the evaluation points of an image yields the resultant extension of the length of the specimen between these points. The resultant extension was extracted from the sequence of DIC images for the entire length of the test. The resultant extension and the initial distance of the evaluation points enabled the strain to be calculated for all the test conducted alongside DIC.

### **4.3.1.2 Comparison of material response extracted from DIC and global strain measurement.**

In this research material behaviours (such as engineering stress and strain) were extracted for all the specimens subjected to tensile deformation, using both the DIC and global strain measurement. Figure 4-29, 4-30 and 4-31 shows the variance of engineering stress against strain, extracted from the DIC and global strain measurement for the three specimens respectively. Graph (b) of these figures represents the material response up to 0.02 strain. The yield point marked in all the graph (b) represents the stress in the specimen at 0.002 strain. It is evident from these graph that the stress at yield point extracted from DIC is always smaller than that extracted from the global strain measurement.

Graph (a) of these figures represents the material response for the entire range of deformation. UTS marked in these graph represents the highest stress recorded in the specimen during deformation. It is evident in graph (a) that the UTS extracted by both the monitoring technique is identical. It can be observed from these graphs that the UTS and failure strain occurs at a larger strain in DIC measurement as compared to that of global strain.

The traditional strain measurement technique assumes that the strain in the gauge section is constant, and are not able to extract the local strain [132]. It is mentioned in [133] that in a

## Results

tensile deformation, extension depends on the gauge length over which the measurement is taken, smaller the gauge length, larger will be the elongation. In DIC strain is extracted from a localized area, in the centre of the specimen. Whereas, the strain in global strain measurement is based on the cross head displacement of the loading machine, which takes into account the entire length of the specimen between the loading jaw. Due to this reason in DIC measurement yield point (0.002 strain) occurs at a lower stress as compared to the global strain. The occurrence of UTS and failure at a larger strain in DIC measurement is also due to the difference in the strain extraction range between the DIC and global strain measurement. The failure strain in global strain measurement is the resultant displacement of the entire specimen length between the loading jaw. Whereas, the failure strain in DIC measurement is the resultant displacement of the localized area at failure (which is always greater than the failure strain in global strain monitoring).

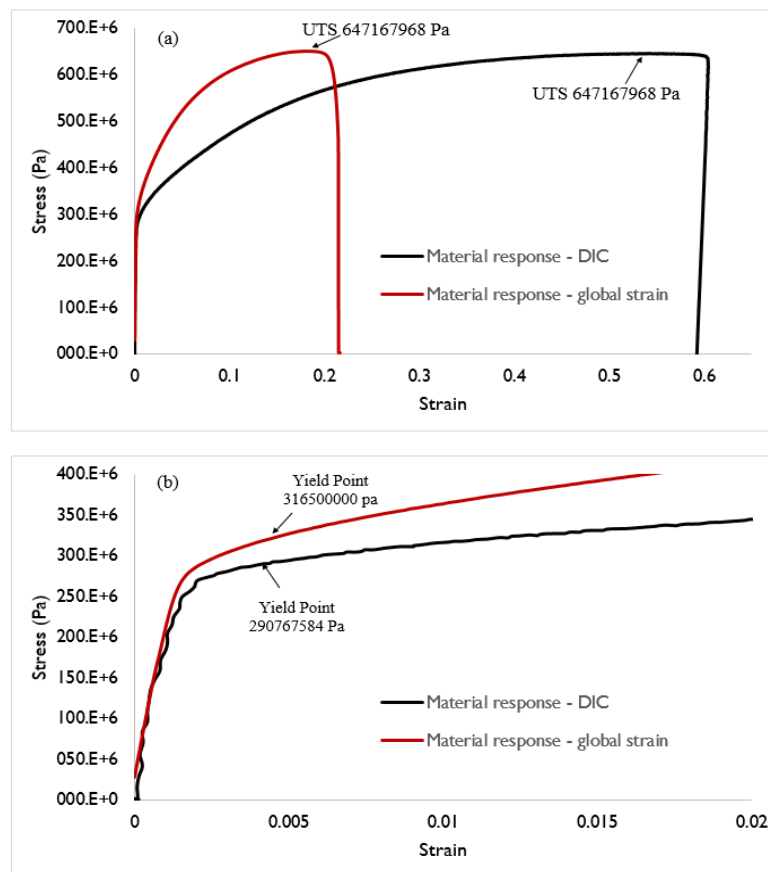


Figure 4-29: Material response of the first Un-notched specimen (a) For the entire length of the test (b) up to 0.02 strain

## Results

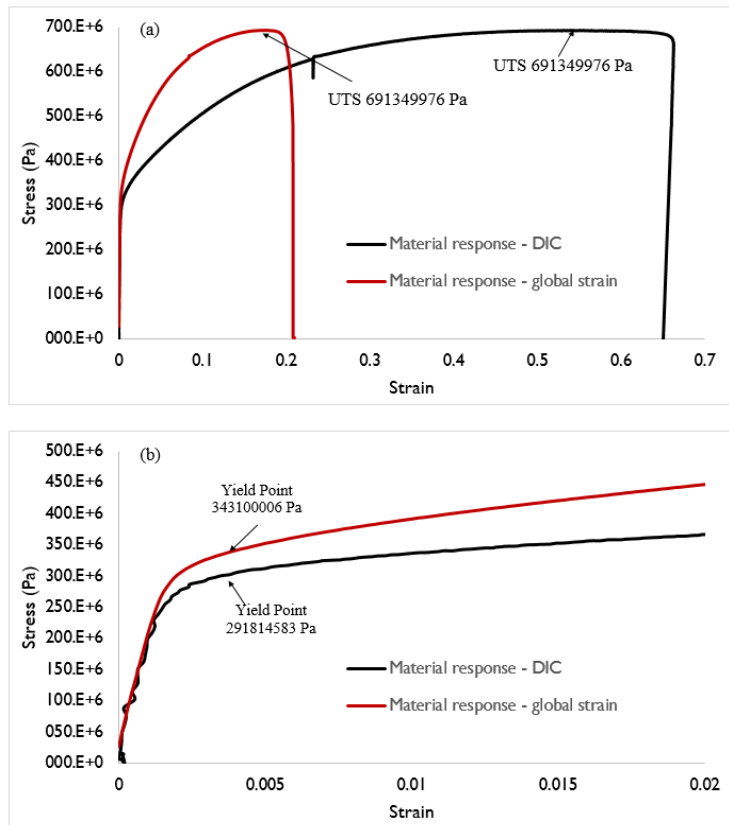


Figure 4-30: Material response of the second Un-notched specimen (a) For the entire length of the test (b) up to 0.02 strain

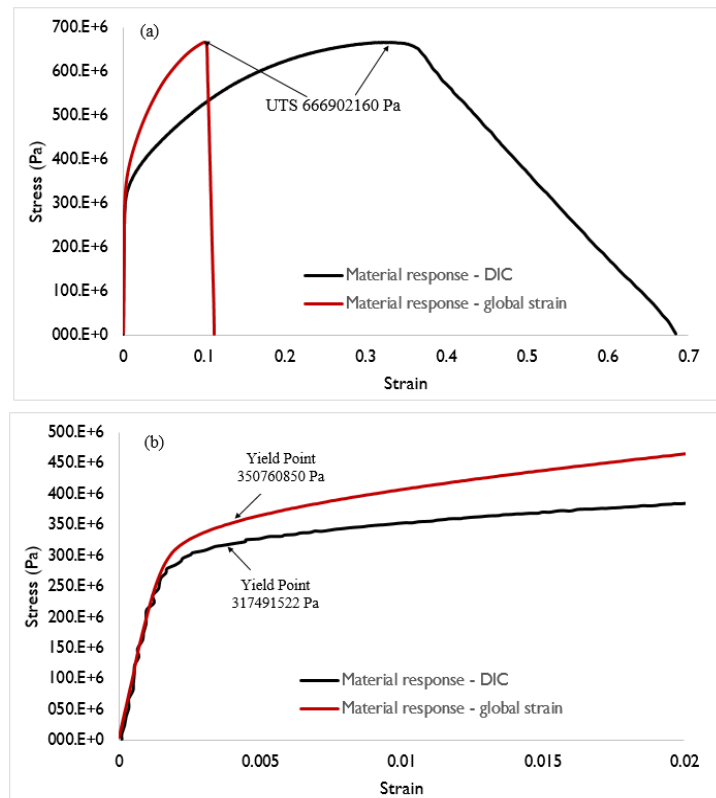


Figure 4-31: Material response of the notched specimen (a) For the entire length of the test (b) up to 0.02 strain

## Results

Figure 4-32 and 4-33 shows the material response for the notched and an un-notched specimen extracted by the DIC and global strain measurement respectively. It is mentioned in [36][38][37], that failure in un-notched specimen of austenitic stainless steel occurs by extensive necking. On the other hand, failure in the notched specimen of austenitic stainless steel takes place by progressive crack propagation. It can be observed in figure 4-32 that the failure strain in the notched specimen is significantly smaller as compared to the un-notched specimen. The failure strain in this figure is the collective strain of the entire specimen length between the loading jaw. In the un-notched specimen, the entire specimen length is extended when the specimen fails. As a result, the collective strain at failure is higher. Whereas in the notched specimen, extension is concentrated only in the centre of the specimen (extension in rest of the specimen is very low), as a result of yielding and progressive crack propagation of the notch plane. Therefore, the collective strain in the specimen at failure is lower.

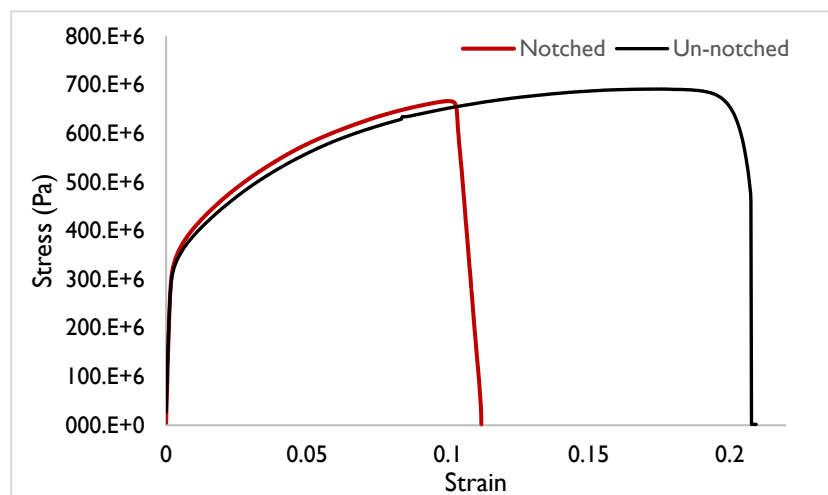


Figure 4-32: Material response extracted by Global strain

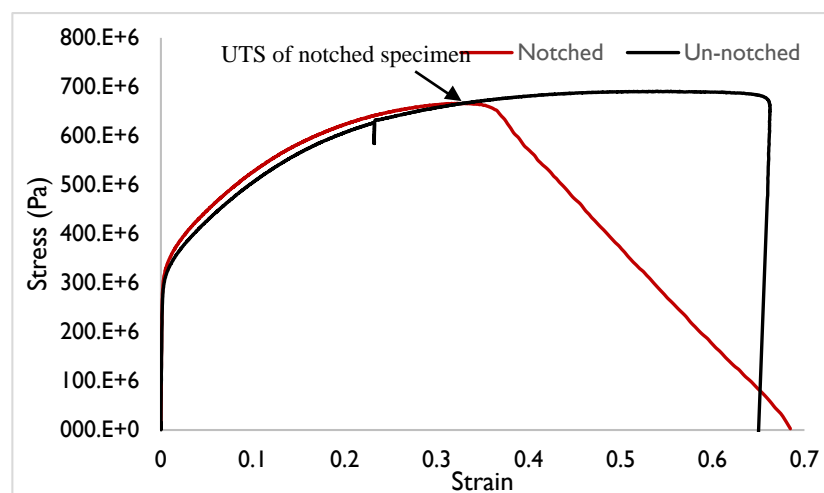


Figure 4-33: Material response extracted by DIC

## Results

It can be observed from figure 4-33 that the failure strain of both the notched and un-notched specimen is almost identical. The failure strain in this figure is the strain in the localized area (*i.e.* centre) of the specimen. It is clear from this figure that after the UTS, the gradient of the stress strain curve belonging the notched specimen falls steadily towards failure strain, unlike the notched specimen in figure 4-32. The steady fall in this gradient resulted in both the specimen (notched and un-notched) failing at the similar strain. In order to investigate on the mechanism of the steady fall in gradient, DIC images of displacement fields were analysed. Figure 4-34, 4-35 and 4-46 shows these images of the un-notched and notched specimen at 0.3, 0.45 and 0.52 strain respectively. It can be observed in figure 4-34 that at 0.3 strain (before UTS of the notched specimen) there is no sign of crack in the either of the specimen. It is clear from figure 4-35 that at 0.45 strain (after the UTS of the notched specimen), there is a tearing in the notch plane of the notched specimen. Whereas, the un-notched specimen is observed to stretch further, without any sign of crack initiation.

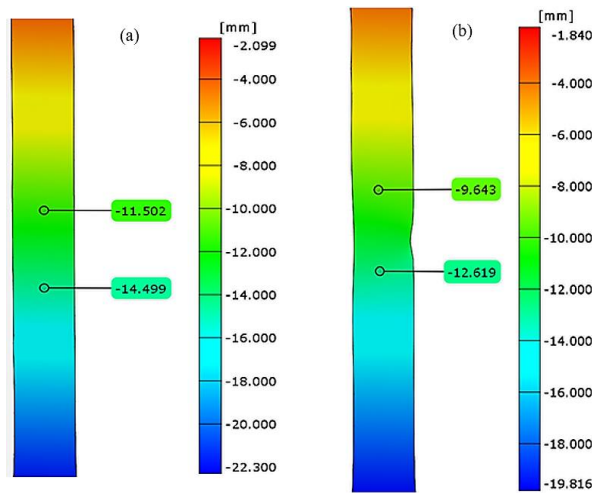


Figure 4-34: Displacement fields at 0.3 strain (a) Un-notched specimen, (b) Notched specimen

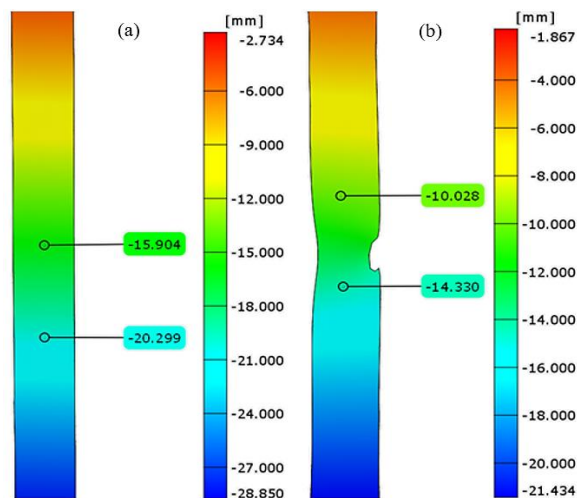


Figure 4-35: Displacement fields at 0.45 strain (a) Un-notched specimen, (b) Notched specimen

## Results

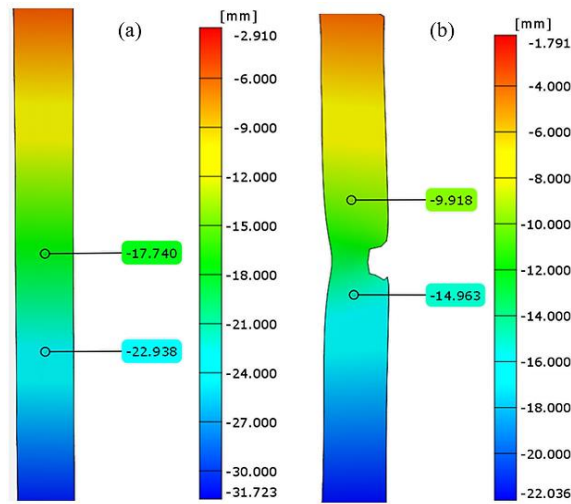


Figure 4-36: Displacement fields at 0.52 strain (a) Un-notched specimen, (b) Notched specimen

In figure 4-36, corresponding to 0.52 strain, the crack in the notch plane in the notch specimen is observed to extend even further, while the un-notched specimen is extended without any sign of crack initiation. Therefore, the steady decrease in the gradient of stress strain curve in figure 4-33 (of the notched specimen) is due to progressive crack propagation in the notch plane.

Between the two monitoring technique, DIC provides an actual representation of the material response during tensile deformation. It only takes into account of the localized area, in the centre of the specimen where the damage is concentrated and eventually fails. The collective strain measurement of the entire specimen length in the global strain technique can mask the localized strain in the notched specimen, as a result, information regarding crack propagation cannot be identified. Whereas, the localized strain measurement using DIC provides critical information of crack propagation. In fact, the onset of the steady decrease in the gradient of stress strain curve can also provide information regarding the crack initiation. Based on these conclusions, material response extracted from DIC was cross validated with AE activity.

### 4.3.2 Correlation of AE monitoring with DIC for tensile test

The traditional features and AE entropy of the AE events, captured with respect to the material response, from the first and second un-notched specimen is shown in figure 4-37 and 4-38 respectively. These specimens were tested until fracture. Graph (a), (b), (c), (d), (e) and (f) in these figures represents the variance of Risetime, Duration, Count, Energy, Peak-amplitude and AE entropy respectively for the entire range of deformation.

## Results

A number of research concluded that during tensile deformation of austenitic stainless steel, there are remarkable AE activity in the initial stages of deformation (*i.e.* from the onset of loading to during and just after yielding) [36][37][35][37][34]. These remarkable source of AE activity was attributed to the dislocation movement. It can be observed in figure 4-37 and 4-38 that from the onset of loading up to about 0.44 and 0.39 strain of the first and second specimen respectively, there are plenty of AE activity. Strain of 0.044 and 0.039 corresponds to an apparent plasticity in the specimen (as the yielding is considered at 0.02 strain). Therefore, like the previously reported research, the initial increase in AE activity observed in figure

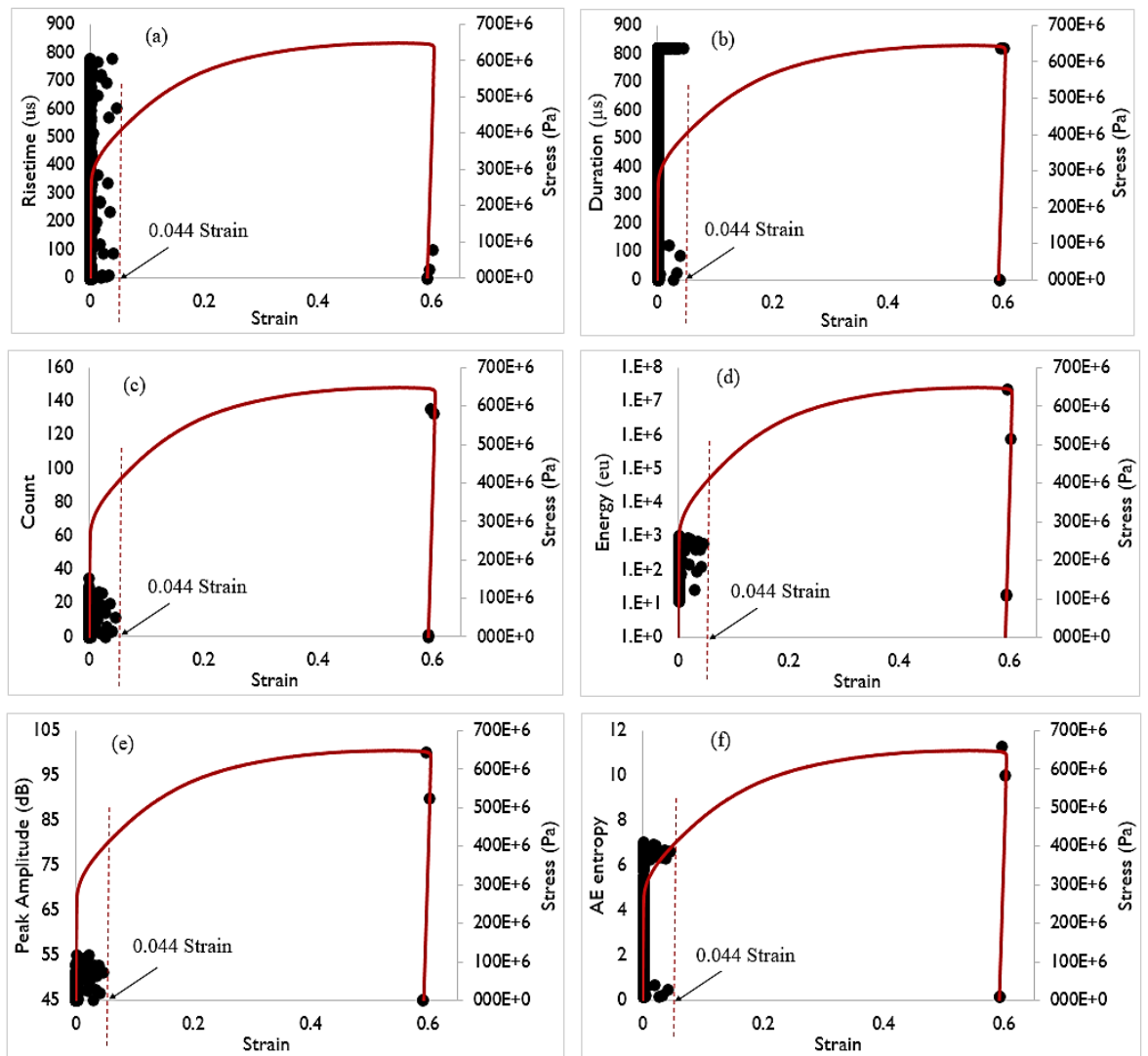


Figure 4-37: Variation of AE features with the material response for the first un-notched specimen: (a) Rise-time (b) Duration (c) Count (d) Energy (e) Peak-amplitude and (f) AE entropy

## Results

4-37 and 4-38 can be attributed to the dislocation movement as a result of yielding. It can be observed in these figure that after the initial increase, there is no AE activity recorded until fracture. It is mentioned in [37][34] that as the austenitic stainless steel continues to deform after yielding, the glide distance of the dislocation movement decreases. Owing to this reason, the dislocation movement after significant yielding does not produce any delectable AE activity. A similar study in austenitic stainless steel concluded that failure in un-notched specimen of austenitic stainless steel occurs by extensive necking, which generates very little elastic wave [36][37][38]. It is evident from these figures that at fracture, the AE activity is significantly lower as compared to the yielding. The occurrence of lower AE activity at fracture can therefore be attributed to the failure by extensive necking.

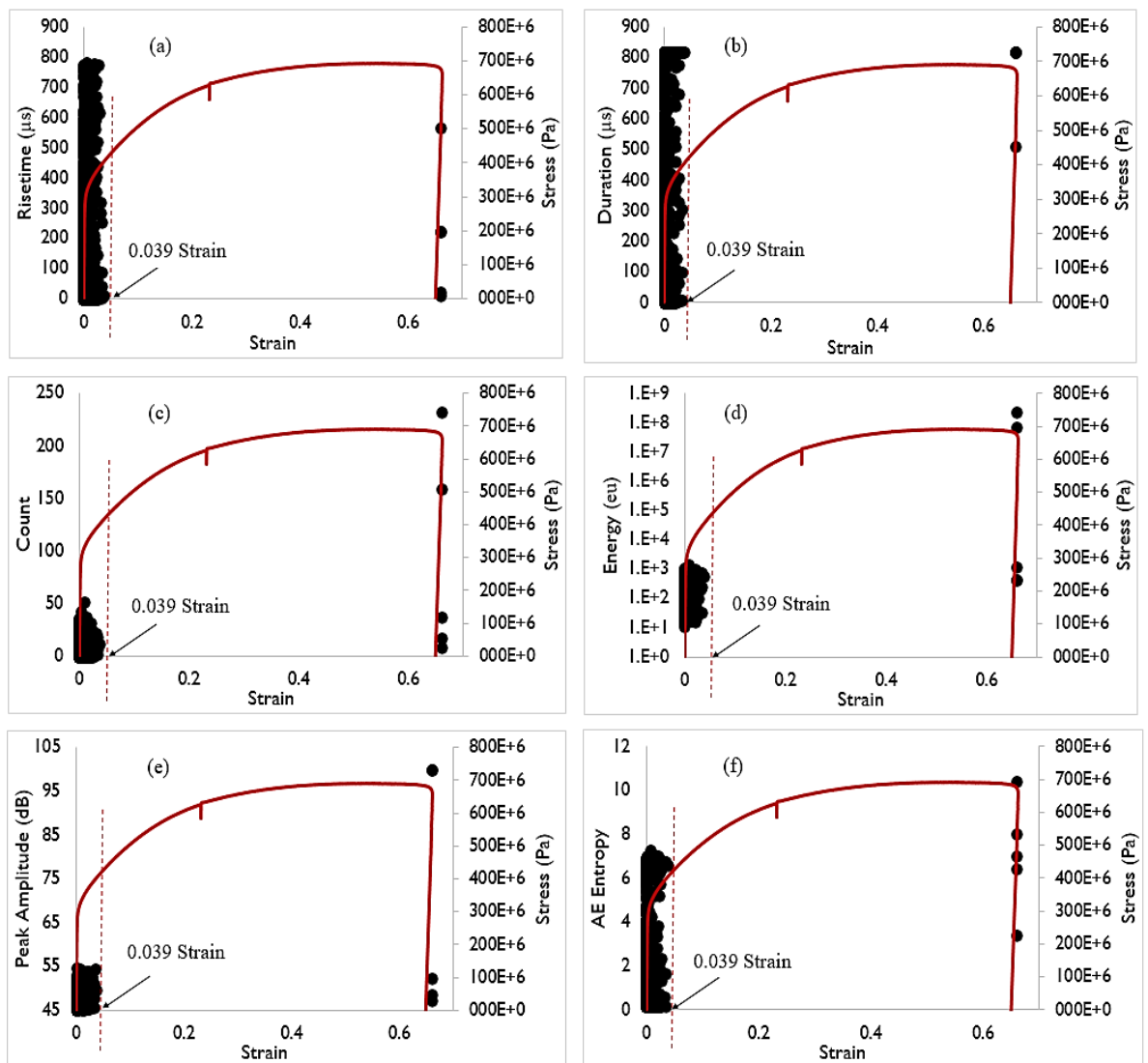


Figure 4-38: Variation of AE features with the material response for the second un-notched specimen: (a) Rise-time (b)Duration (c)Count (d)Energy (e)Peak-amplitude and (f) AE entropy

It can be observed in graph (a) of these figures that during yielding the Risetime of the AE events are distributed between 0 to 800 $\mu$ s. Whereas at fracture, it is noticeably lower. Risetime feature does not provide much information of tensile deformation, as a result it has never been used to predict failure in these circumstances. It can be observed in graph (c), (d), (e) and (f) that Count, Energy and Peak-amplitude exhibits the same trend as AE entropy. It is evident from these graphs that, events at fracture can be clearly distinguished from the rest of the events, as they have significantly higher value of features. However, during yielding there is no apparent distinguishable events. During yielding AE entropy is distributed between approximately between 0 to 8, whereas at the fracture is accompanied by value beyond 10. Count and peak voltage measurement (also known as Peak-amplitude) has been widely used to study the failure mechanism in austenitic stainless steel during tensile deformation [39][36][37][35][34]. It is clear from these result that AE entropy exhibits the same trend as the count and Peak-amplitude. Therefore, it has the potential to replace them in a similar investigation. It can be observed in graph (b) of these figures that there is no distinguishable change in Duration of the events during fracture from yielding. Like the fatigue test, the small FPLS (*e.g.* 800 $\mu$ s) limited the length of the waveform over with the duration is computed. As a result, there was no significant increase in duration at fracture.

The traditional features and AE entropy of the AE events, captured with respect to material response, from the notched specimen is shown in figure 4-39. Graph (a), (b), (c), (d), (e) and (f) represents the variation of Risetime, Duration, Count, Energy, Peak-amplitude and AE entropy respectively for the entire range of deformation. Like the un-notched specimen, it can be observed in figure 4-39 that during yielding, there are a remarkable number of AE activity. It is also evident from this figure that after the initial increase in AE activity, there is no AE activity recorded until 0.53 strain (corresponding to the necking region). This phenomenon is consistent with the un-notched specimen except the AE activity in the notched specimen starts to increase remarkably before the final fracture. It is mentioned in [36][38][37] that the necking of the notched specimen is takes place by progressive crack propagation which produces significant amount of AE activity. Therefore, the AE activity from 0.53 strain until final fracture can be attributed to the crack propagation in the notched plane. However, it is interesting to note that, the necking starts at approximately 0.35 strain,

## Results

whereas the AE activities are only recorded from 0.53 strain. The onset of necking region is an indication of crack initiation (as the steady decrease in the gradient of stress strain curve is as a result of crack propagation). Therefore, it can be deduced that AE activities begins to appear only after the crack has initiated and propagated to a certain length. In order to investigate this phenomenon, the change in crack length during the test, prior to the fracture was analysed. The crack length was obtained from the DIC images of the test. Figure 4-40 shows the variation in crack length against strain, from the onset of necking to just before the fracture of the notched specimen. It can be observed in this figure that the crack after 0.55 strain propagates much faster compared to the crack from the onset of necking. Therefore, the occurrence of AE activity at a higher strain (0.53 strain) after necking could result from the faster propagating crack.

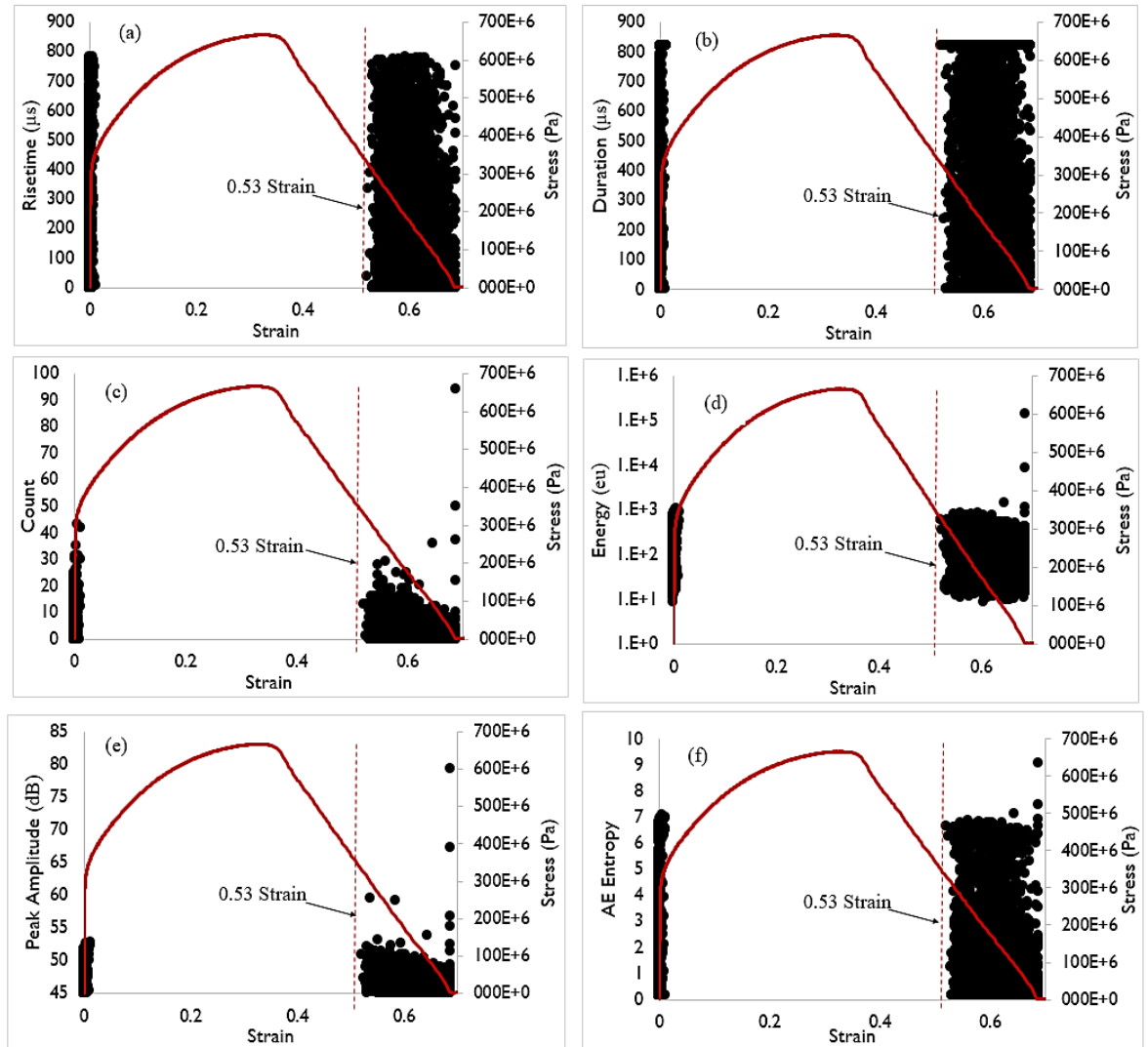


Figure 4-39: Variation of AE features with the material response for the notched specimen: (a) Rise-time (b)Duration (c)Count (d)Energy (e)Peak-amplitude and (f) AE entropy

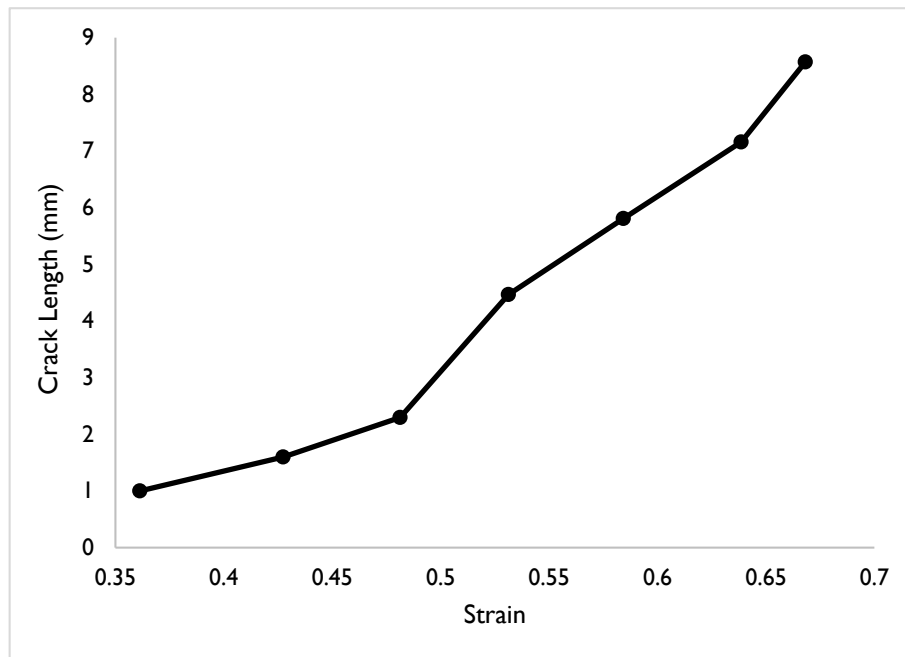


Figure 4-40: Crack length against strain of the notched specimen

This suggests that the slower propagating crack generates elastic waves which are below the threshold level. As a result, they are not recorded by the AE data acquisition system. It is clear from graph (c), (d), (e) and (f) of figure 4-39 that the Count, Energy, Peak-amplitude and AE entropy possess similar trends (the features at fracture are noticeably higher). At fracture, the AE entropy in the notched specimen is above 9, whereas, the rest of the event had an AE entropy between 0 to 8. The fracture of the un-notched specimen was accompanied by an AE entropy of above 10, which is slightly above the one recorded at fracture of the notched specimen. The fracture surface of the un-notched specimen was greater than that of the notched specimen, as a result it produced a slightly higher AE entropy (the fracture surface in the case of the notched specimen was reduced as a result of crack propagation in the notch plane).

#### 4.4 Chapter summary

Evaluation of AE entropy suggests that it is independent of threshold and HDT settings. This independency of AE entropy arises because it is directly derived from the discrete voltage values which has a component below the threshold and outside the HDT.

Prior to validation of AE entropy in a fatigue test, the AE data generated from the specimen was filtered using 1D linear localization technique. The filtration suggests that it had a significant effect in de-noising the dataset. Both the correlation and cumulative AE entropy

exhibits the same trend as the traditional AE features. This suggest that the traditional analysis can be replaced with AE entropy of the critical damage detection, as it is independent of acquisition settings and reduces the need for human judgement in measuring the AE waveform. The cross-validation of the correlation AE entropy with global strain measurement suggests that it is sensitive in identifying the initial yielding (*i.e.* as a result of the onset of loading) and fracture of the specimen. The global strain measurement did not provide the time of occurrence of plastic zone formation and crack initiation. In order to successfully cross-validate the formation of plastic zone with AE entropy, the next fatigue tests were conducted with simultaneous AE and DIC monitoring. However, the cross-validation of the correlation AE entropy with DIC suggests it to be ineffective in identifying the plastic zone formation before crack initiation in the specimen. The same conclusion is drawn for all other traditional AE features in this study. On the other hand, in the cumulative analysis a sharp jump in AE entropy was observed at the onset of plastic zone formation.

The correlation AE entropy in a tensile test exhibits the same trend as most of the widely used AE features (*i.e.* widely used AE feature in tensile test). This observation further suggest that the AE entropy has the potential to replace traditional AE features. The cross-validation of the correlation AE entropy with stress and strain suggest it to be sensitive to yielding. From the onset of loading to just after yielding there were plenty of AE activity however they did not have dominant AE entropy. Whereas, the fracture of the specimen was accompanied by a small number of AE activity but they had dominant AE entropy.

## 5 Discussion

### 5.1 Correlation between standard test on coupon specimen and real structures under operation.

In the fatigue tests of this research, it is clear from figure 4-20, 4-21, 4-25 that, cumulative energy is noticeably higher at the fracture. Significantly higher energy of a few AE events at fracture masks the cumulative trend in energy prior to the fracture. Whereas, cumulative AE entropy and count begins to increase in the later stages of fatigue towards fracture and there is no noticeable jump observed in these cumulative trend at the fracture. Although, AE entropy possesses the same trend as count, it is independent of threshold and HDT. As a result, can identify damages as reduced human interference with the acquisition settings. This research is focused in validating the performance of AE entropy, prior to and during the yielding and crack initiation (initial damage sources in LNG cargo containment). Therefore, the ineffectiveness of the features at fracture is not considered to be a disadvantage. It is evident from figure 4-26 that cumulative entropy, energy and count shows the same trend. There was no sharp jump in cumulative energy in figure 4-26 at the end, as this test was interrupted just before the specimen could fracture.

During fatigue of un-notched specimen, plastic zone is formed due to significant localized formation and coalescence of micro crack. The formation of plastic zone facilitates macro fatigue crack initiation, these fatigue cracks propagate and leads to an ultimate fracture of the specimen. Therefore, at the onset of plastic zone formation, the service operation of the structure could be interrupted to avoid the ultimate fracture. The cross validation in AE and DIC of the third and fourth fatigue test (figure 4-25 and 4-26), revealed that cumulative AE entropy is sensitive in identifying the onset of plastic zone formation in the specimen like the traditional cumulative analysis. The similar increasing trend in cumulative AE entropy and count, in all the fatigue test conducted, shows its feasibility and effectiveness as a damage identification feature. Unlike cumulative count and energy, cumulative AE entropy

## Discussion

is independent of user defined acquisition settings. This can reduce the need for human judgement in measuring the feature of the signal. Therefore, in AE monitoring of fatigue studies, cumulative AE entropy has the potential to replace some of the traditional features in the future. The cross validation of AE and DIC (in figure 4-25 and 4-26) also shows that the AE activity begins to increase noticeably before the damage manifest into plastic zone formation. The noticeable increase in AE activity before plastic zone formation is due to the growth and coalescence of micro-crack which is not identified by either DIC and global strain measurement. This suggest that AE is a good identifier when a failure is starting.

Cumulative analysis of AE feature is an important method in understanding the global damages mechanism of the specimen subjected to loading. As a result, it has been adopted in many studies on coupon specimen, to investigate the ability of AE as a damage identification technology in the material (*e.g.* material of the coupon specimen). These investigations are performed to determine whether AE can be implemented in structures, constructed from this material, to provide warning of developing damage. The loading conditions adopted for the previous studies on coupon specimens were all recurrent in nature, such that, a continuous loading spectrum is applied to the specimen from the onset of loading until the failure of the specimen. However, it is important to note that the loading condition of the structure under operational condition may not be continuous.

In LNG cargo tank, sloshing is the only un-predictive load that results in its structural degradation. The ABS and DNV.GL provided guidelines in order to predict the loading spectra in the LNG cargo tank through modelled sloshing experiments [13][26]. In accordance with these guidelines, many studies were conducted on the rigid model of a second tank in a four-tank 138000m<sup>3</sup> membrane type LNG carrier [11][30][134]. These studies suggested that the sloshing impacts are complex in shape, consisting of pressure, in the form of impulse, lasting for a few milliseconds. The maximum and mean duration of the sloshing impact recorded in their studies were 200ms and 11.7ms-27.4ms respectively [30][135]. The duration of typical sloshing impact in high filling (*e.g.* 92.5% tank of height) condition were 2-10ms with a risetime of 0.2-0.9ms [11], whereas in a low filling condition (30% tank of height) sloshing impact duration were 2-20ms. It is also suggested in [30] that the sloshing impacts are separated by a zero pressure intervals in the order of a few seconds and the interval between the sloshing impacts are not consistent. Figure 5-1 shows a typical sloshing impact spectrum in a LNG cargo tank.

## Discussion

Figure 5-2 shows the loading spectra adopted in fatigue test of this research. The specimens were subjected to the same loading spectra from the start of the test until fracture. This loading spectra was adopted to replicate the structural response in the coupon specimens due to sloshing impact. It is evident from figure 5-2 that the duration of the respective load (*e.g.* from one minimum load point to the next) is 200ms, which is comparable to the duration of the sloshing impact experienced by a LNG cargo tank during voyage. However, it can be observed from this figure that there is no delay between the subsequent load. In other words, there is no separation between the subsequent loads, as experienced by the real LNG cargo tank.

Although in this research, the cumulative AE entropy is able to provide valuable information of damages in coupon specimen, subjected to fatigue loading, it cannot be implemented as a condition monitoring technique on the primary wall of the cargo tank. Primarily because the

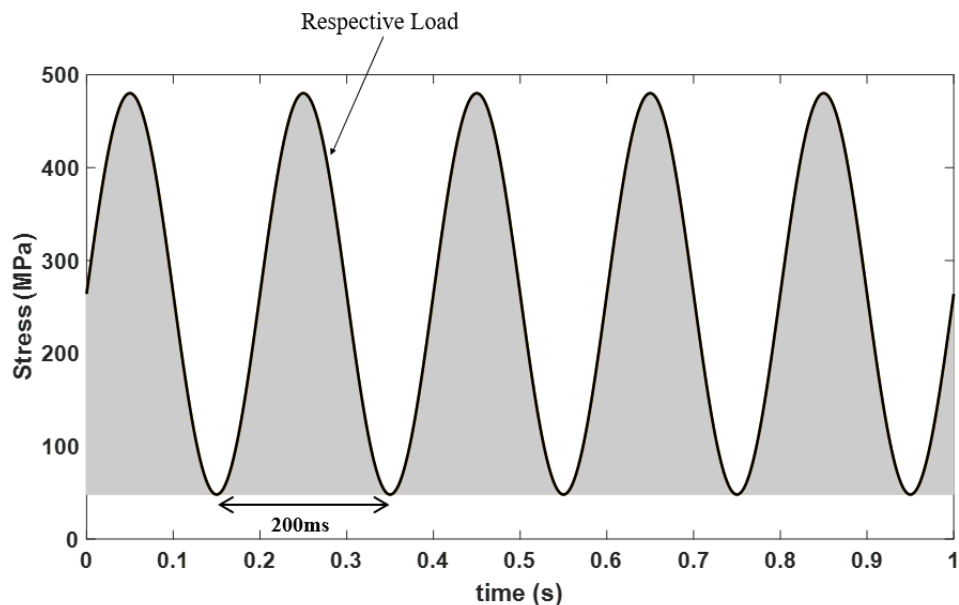


Figure 5-1: Replicated sloshing impact on a coupon specimen

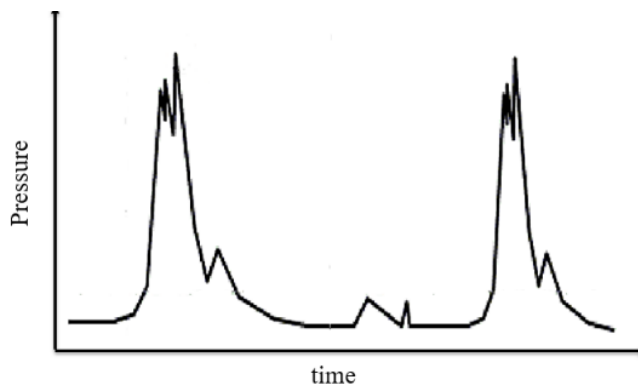


Figure 5-2: Pressure time history in a membrane LNG cargo tank [13]

loading condition of the coupon specimen in this research is continuous in nature without any delay between the subsequent load. Whereas, the sloshing impacts in the cargo tanks are separated by random length of zero pressure values. There may not be a noticeable increase in the cumulative AE entropy, during plastic zone formation, if it is used to monitor the cargo tanks. Specially, if the duration of zero pressure values increases during plastic zone formation or crack initiation, as compared to the other stages.

The cumulative analysis was employed in this research solely to validate the performance of AE entropy with respect to the traditional AE features. Since the previous fatigue studies of un-notched coupon specimens are mostly based on the cumulative analysis [77][78][79], there were plenty of data in the literature to compare and understand the trend in traditional cumulative features obtained in these research. The characteristic cumulative trend in traditional AE features were then used to investigate how effective the trend in AE entropy is in identifying the fatigue damage evaluation.

Considering that the cumulative AE analysis may not be a suitable condition monitoring technique for the primary wall, the only other technique which can be explored is the individual AE feature analysis. It can be observed in graph (f) of figure 4-23 and 4-24 that during the onset of plastic zone formation, there is no noticeable increase in AE entropy. In fact, it can be observed in graph (c), (d) and (e) of these figures that there is no noticeable increase in either Count, Energy and Peak-amplitude at the onset of plastic zone formation. It is mentioned in [136][137], that the rate of AE activity increases with the formation and growth of plastic zone. This increase is attributed to the continuous new yielding in and at the edge of plastic zone, which is reflected in the cumulative AE analysis (*e.g.* the third and fourth specimen in figure 4-25 and 4-26). Whereas the AE analysis (*e.g.* Count, Energy, Peak-amplitude and AE Entropy) does not provide any information regarding the formation of plastic zone. This indicates that although the rate of AE event generation is higher, the individual strength of AE events does not change noticeably. In austenitic stainless steel, plastic zone formation is known to produce AE events with weaker features as compared to the ones at fracture [73]. This is because the amount of material yielding in and at the edge of plastic zone is not sufficient to produce AE events with high strength. Since AE entropy during the formation of plastic zone is lower as compared to the ones at fracture and onset of loading, it suggests that AE events during in these period is less disordered. It can also be suggested

that the lower strength AE events during this period is responsible for its low disorderness. It is clear that the plastic zone formation due to repeated cyclic loading will not be identified by AE entropy and traditional features. The plastic zone precedes crack initiation in material subjected to fatigue loading. Since AE entropy is not sensitive to plastic zone formation, a warning prior to the crack initiation in the primary wall of the cargo tank cannot be successfully achieved.

It can also be observed in graph (c), (d), (e) and (f) of figure 4-23 and 4-24, that in the period between the plastic zone formation and the end of the test, there is no noticeable increase in AE entropy and the traditional features (*e.g.* Count, Energy and Peak-amplitude). During this period, fatigue crack propagates and leads to the ultimate fracture. Fatigue crack propagation and initiation is known to produce strong AE events where the damage mechanism is accompanied by cleavage [138][71]. According to these studies, in the absence of cleavage, there is no noticeable strong AE events. Austenitic stainless steel is a ductile material, therefore, the fatigue crack propagation takes place through ductile tearing without any cleavage failure. As a result, there is no noticeable increase in the AE entropy and traditional features during crack propagation. Based on its sensitivity, it can be concluded that it may not be a suitable technique for this damage mechanism.

It can be observed in graph (c), (d), (e) and (f) of figure 4-18, 4-19 and 4-23 that the fracture of the specimen is accompanied by a strong AE entropy and the traditional feature (*e.g.* Count, Energy and Peak-amplitude). The noticeable increase in AE entropy at fracture indicates that it can be used in application which requires real time information regarding fracture. This research is focused on validating the performance of AE entropy against the initial stages of damage in the primary wall. As a result, its effectiveness at fracture is not considered as an advantage.

It is clear in graph (f) of figure 4-18, 4-19, 4-23 and 4-24 that the initial yielding (at the onset of loading) is associated with a noticeable increase in AE entropy. In every fatigue test, the initial yielding is associated with AE entropy of above 10. Like the AE entropy, it can be observed in graph (c), (d) and (e) of this figure that during the initial yielding, there is also a noticeable increase in the traditional AE features (*e.g.* Count, Energy and Peak-amplitude). The yielding/deformation activities in the primary wall of the cargo tank are important source of information, as they are considered

to be a dominant damage mechanism due to sloshing impact during voyage [13][14]. Figure 1-4 illustrates an example where the primary barrier of the cargo tank has yielded/deformed permanently due to unexpected sloshing impact. Since AE entropy is sensitive in identifying yielding, it can be successfully applied to monitor the primary wall against this damage mechanism. The information of yielding/deformation in the primary wall can educate the ship operators regarding the structural condition of the cargo tank. So that an appropriate maintenance can be planned to avoid further failure and shut down cost.

In the tensile test of these research, it can be observed in graph (c), (d), (e) and (f) of figure 4-37, 4-38 and 4-39 that the only noticeable increase in AE entropy and the traditional features (*e.g.* Count, Energy and Peak-amplitude) are at the fracture. Unlike the fatigue test, the yielding in tensile test is not accompanied by a noticeable increase in AE entropy. This difference in AE behaviour between the tensile and fatigue specimen arises due to the respective loading conditions. During fatigue test the specimens were loaded gradually up to mean stress (*e.g.*  $\text{MaxStress} - \text{MinStress} / 2$ ), from which sinusoidal loading at a frequency of 5Hz was applied until fracture. Whereas, the tensile specimens were subjected to a constant strain rate of 0.0040 or 1mm/s from start of the test until fracture.

Graph (a) in figure 5-3 shows the global strain against time for the second fatigue specimen subjected to loading. Graph (b) and (c) of this figure shows the variation in the strain and stress respectively up to 500 seconds. The correlation dots in this figure corresponds to the maximum strain and stress in the load cycle and the interval between the correlation dots are 76 cycles. The initial increase in global strain (marked by an arrow) is due to the onset of loading (as peak load in the cycle was 480Mpa, which is greater than the yield stress of the material). Unlike the third and fourth fatigue test, this specimen was not monitored with DIC as a result the time of formation of plastic zone is not known. It can be observed in graph (b) of this figure that there is a gradual increase in strain up to mean stress. For the duration, the specimen is held at constant mean stress, there is no noticeable increase in strain. After the onset of sinusoidal loading there is a sharp increase in strain from 0.009 to 0.023, which remains noticeably constant until fracture. In fact, this sharp increase in strain takes place in 0.05 seconds (refer to the Appendix A.4 for the calculation), which is not reflected in graph (b) because the correlation dots are extracted in every 76 cycle (*e.g.* in approximately 15 seconds). Therefore, the strain rate at the onset of cyclic loading is 0.157 ( $0.023 / 0.05$  -

## Discussion

0.009/0.05). In comparison to the loading at constant strain rate during tensile test, the strain rate at the onset of cyclic loading in fatigue test is significantly higher.

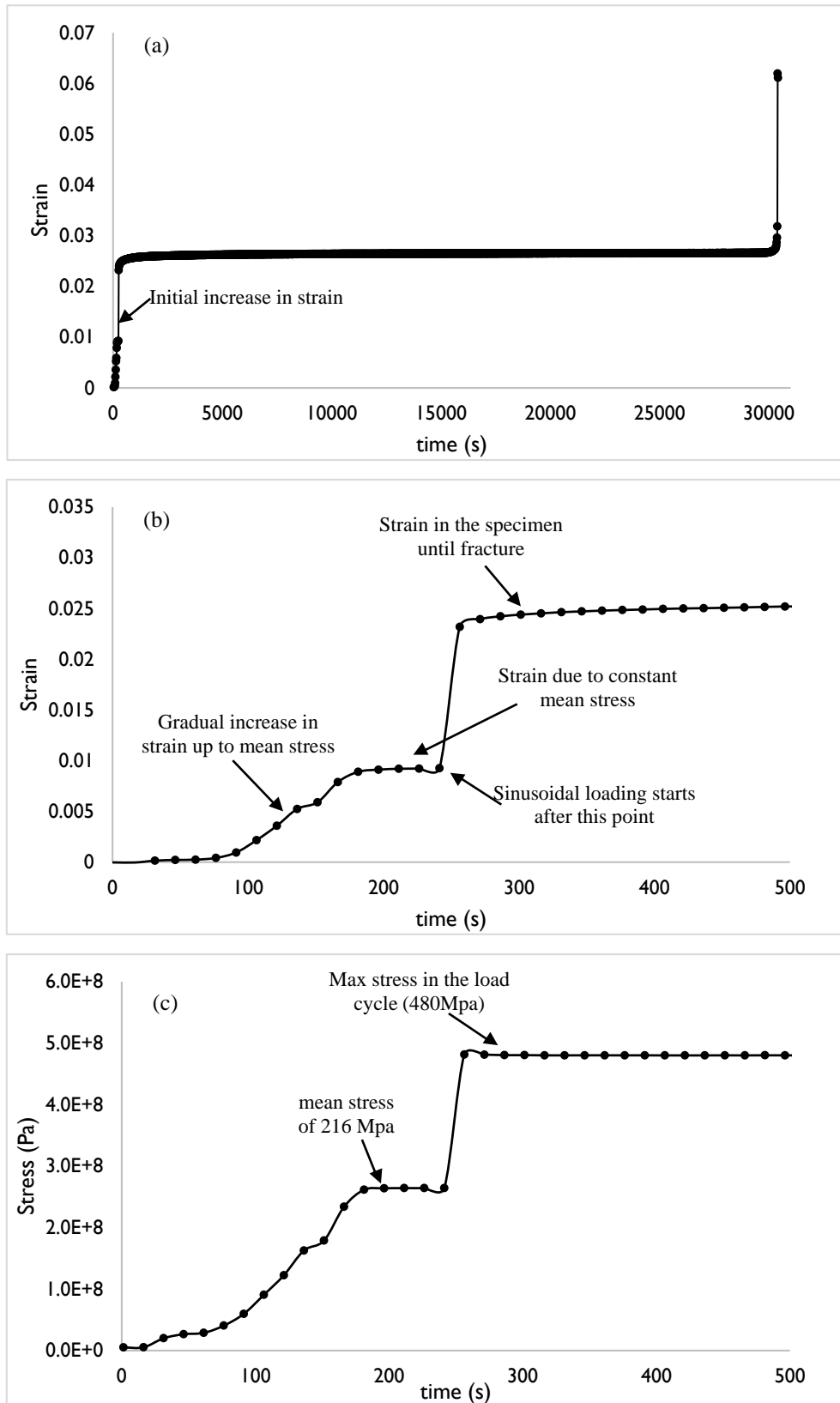


Figure 5-4: (a) Strain in the fatigue specimen for the entire duration of the test (b) strain in the specimen up to 500s (c) Applied stress up to 500s

Figure 5-4 shows the variation of tradition AE features and AE entropy with respect to strain for the second fatigue specimen up to 500 seconds. Graph (a), (b), (c) and (d) of this figure represents the variation of Count, Energy, Peak-amplitude and AE entropy respectively. It can be observed in these graphs that the sudden increase in strain at approximately 250s (a strain rate of 0.157 due to the onset of cyclic loading) is accompanied by a dominant AE features. For instance, AE event at the sudden increase in strain is associated with an AE entropy of above 10. It can also be observed that the AE features during gradual increase in strain from about 100s to 185s is comparatively lower. Therefore, it is clear that the dominant increase in AE feature in the beginning of the test in figure 4-19 is due to sudden increase in strain (at the onset of loading).

Strain rate has been shown to enhance the AE events generation in wide range of materials such as  $\alpha$  brass [91], 7075-T6 aluminium [139], discontinuous yielding material [89], single crystal copper [140] and austenitic stainless steel [34][37]. For instance, in  $\alpha$  brass the Count of AE events increased with the strain rate. In 7075-T6 aluminium, the RMS (Root Mean Square) voltage of AE events were proportional to the strain rate. The increase in strain rate on single crystal copper was accompanied by an increase in count and RMS voltage of AE events. In austenitic stainless steel, with the increase in strain rate, the RMS voltage, count and frequency content of the AE events was shown to increase.

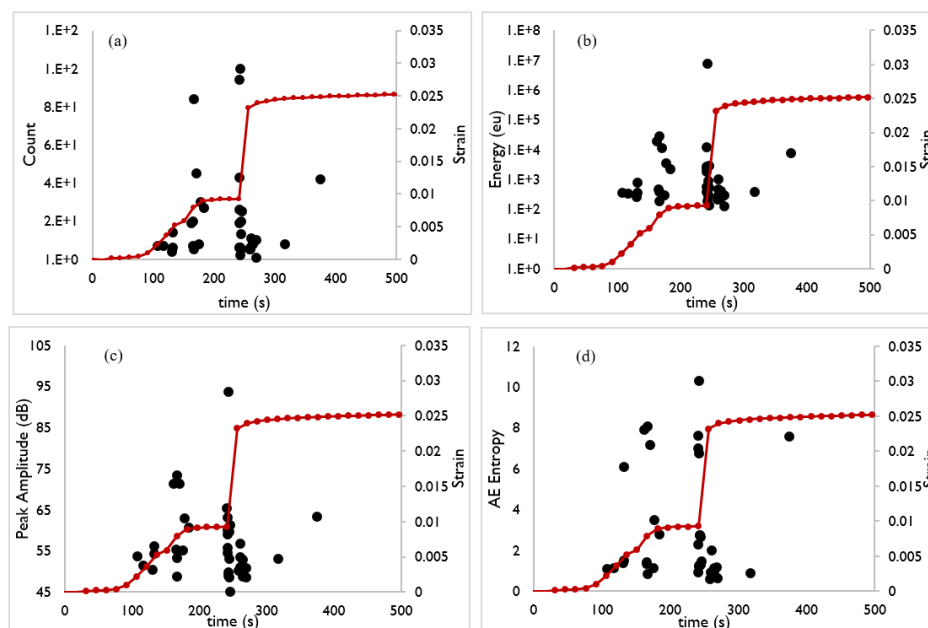


Figure 5-5: Variation of AE features and strain up to 500 seconds: (a)Count, (b) Energy (c) Peak Amplitude and (d) AE entropy

## Discussion

In these studies, (apart from the discontinuous yielding material), the increase in AE event generation was attributed to the increase in rate of source activation, instead of the formation of the new source. In austenitic stainless steel, this increased rate of source activation refers to the increase in velocity of the mobile dislocation [34][37]. In other word, with the strain rate, the velocity of the mobile dislocation also increases. It has been reported in [37][141] that the strain rate in austenitic stainless steel is related to the mobile dislocation velocity according to equation 5-1.

$$e = p_m b v_{av} \quad \text{Equation 5-1}$$

Where  $e$  is strain rate,  $p_m$  is the dislocation density,  $b$  is the Burgers vector and  $v_{av}$  is the average dislocation velocity. It has also been reported in [142] that the squared RMS voltage of the AE waveform recorded during deformation is directly proportional to the strain rate in many single and poly crystals. The relation between the strain rate and RMS voltage, according to this study is shown in equation 5-2. Where  $e$  is the strain rate and  $V_{rms}$  is the RMS voltage.

$$e = V_{rms}^2 \quad \text{Equation 5-2}$$

Thus from equation 5-1 and 5-2, it can also be deduced that the voltage RMS is related to the dislocation density  $p_m$ , the Burgers vector  $b$  and the average dislocation velocity  $v_{av}$ . The equation relating these quantities is shown in equation 5-3. By considering this relation, it is suggested in [34] that in austenitic stainless steel, with the increase in average velocity of the dislocation (due to higher strain rate), the  $V_{rms}$  of the waveform also increases.

$$V_{rms}^2 = p_m b v_{av} \quad \text{Equation 5-3}$$

Therefore, the significantly higher AE entropy and the traditional features in a fatigue test at the onset of cyclic loading, can be attributed to the enhanced average velocity of the dislocations. The higher strain rate in a fatigue test facilitated in an enhancement of the average velocity of dislocations, which gives rise to the AE events with higher feature. In the cargo tank, the maximum duration of sloshing impact is 200ms, which is identical to the duration of respective load in fatigue test. Owing to this reason, a strong sloshing impact has the potential to cause deformation in the primary wall with a significantly higher strain rate

(comparable to the one in fatigue test), than the standard tensile test of this research. Therefore, the deformation in the primary wall due to sloshing can be associated with a noticeable increase in AE features. AE entropy in particular can be expected to be above  $\times 0$  during the deformation caused by sloshing.

## 5.2 Factors affecting AE entropy computation

AE entropy has the potential to be implemented in the commercial data acquisition systems as it can provide valuable condition monitoring indication of damages in structures during operation and maintenance, at reduced reliance on human judgement to set the primary AE acquisition settings. However, there are some aspects to be addressed while performing AE entropy computation, particularly the voltage distribution range and bin width.

Firstly, the Voltage Distribution Range (VDR) is an important aspect to consider while performing AE entropy computation. VDR is the range of voltage over which probability distribution is calculated. Ideally, VDR should be set by taking into account the highest and lowest voltage value of the highest peak amplitude signal in the dataset. However, it is not possible to predict these values prior to the experiment. Therefore, VDR of -100mV to +100mV was chosen for these experiments, which is equal to the maximum limit of voltage range in AE data acquisition system for transient waveform recording. Insufficient VDR can result in an inaccurate computation of AE entropy.

Figure 5-5 shows the effect of VDR on the calculated AE entropy, of a waveform captured during the fracture of the first fatigue specimen. It can be observed in graph (a) of this figure that VDR of -10 to +10 restricts the probability distribution of the voltages from -10 to +10 and results in an AE entropy of 2.4. It can be observed in graph (b), (c), (d), (e) and (f) that with increasing the VDR, the AE entropy also increases. It is also evident that, the AE entropy in graph (f) is almost four times that in graph (a), although both the graphs correspond to the same waveform. This increase in AE entropy with VDR is due to the increase in available probability of mass of the voltage.

Like the effect of VDR on AE entropy, the traditional features are also effected by the maximum limit of the voltage range in the waveform. Figure 5-6 shows the representation of the waveforms, with a series of maximum limit of the voltage range, equivalent to each

of the VDR in figure 5-5. Each of the graph in figure 5-6 contain some of its traditional features. It is evident from this figure that with the maximum limit of the voltage range, the traditional features of the waveform increases. This can be attributed to the additional voltage values at the higher limit of the voltage range. Unlike the acquisition setting, the maximum limit of the voltage range is not a user input parameter. In other word, the traditional features are always calculated from a built-in voltage range. Therefore, in every situation the traditional features are going to be extracted from the same voltage range.

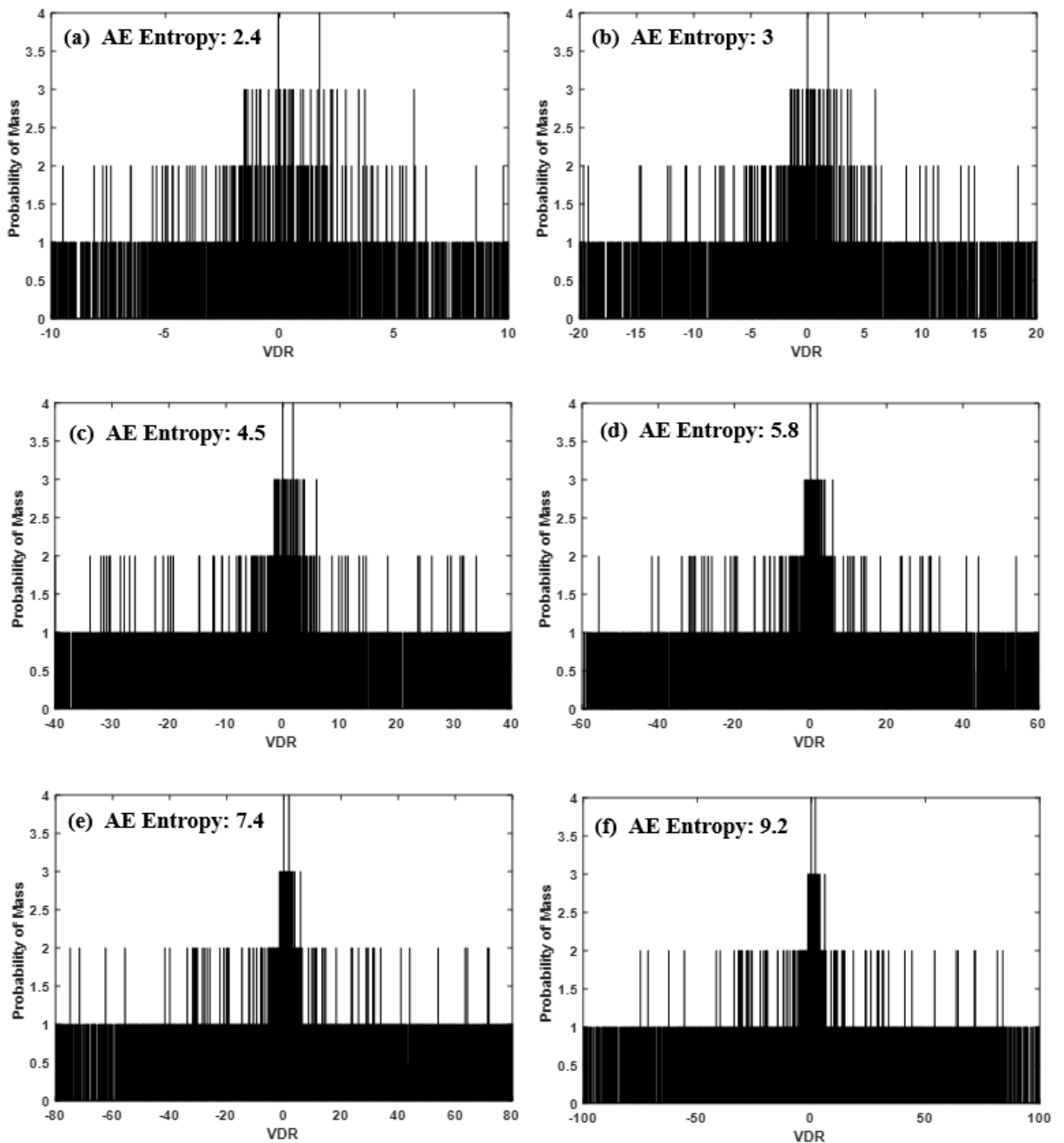


Figure 5-6: Effect of voltage distribution range on AE entropy: (a) VDR -10 to +10, (b) VDR -20 to +20, (c) VDR -40 to +40, (d) VDR -60 to +60, (e) VDR -80 to +80 and (f) VDR -100 to +100.

## Discussion

If AE entropy is implemented in the AE data acquisition system, the VDR can always be set equal to the built-in maximum limit of the voltage range.

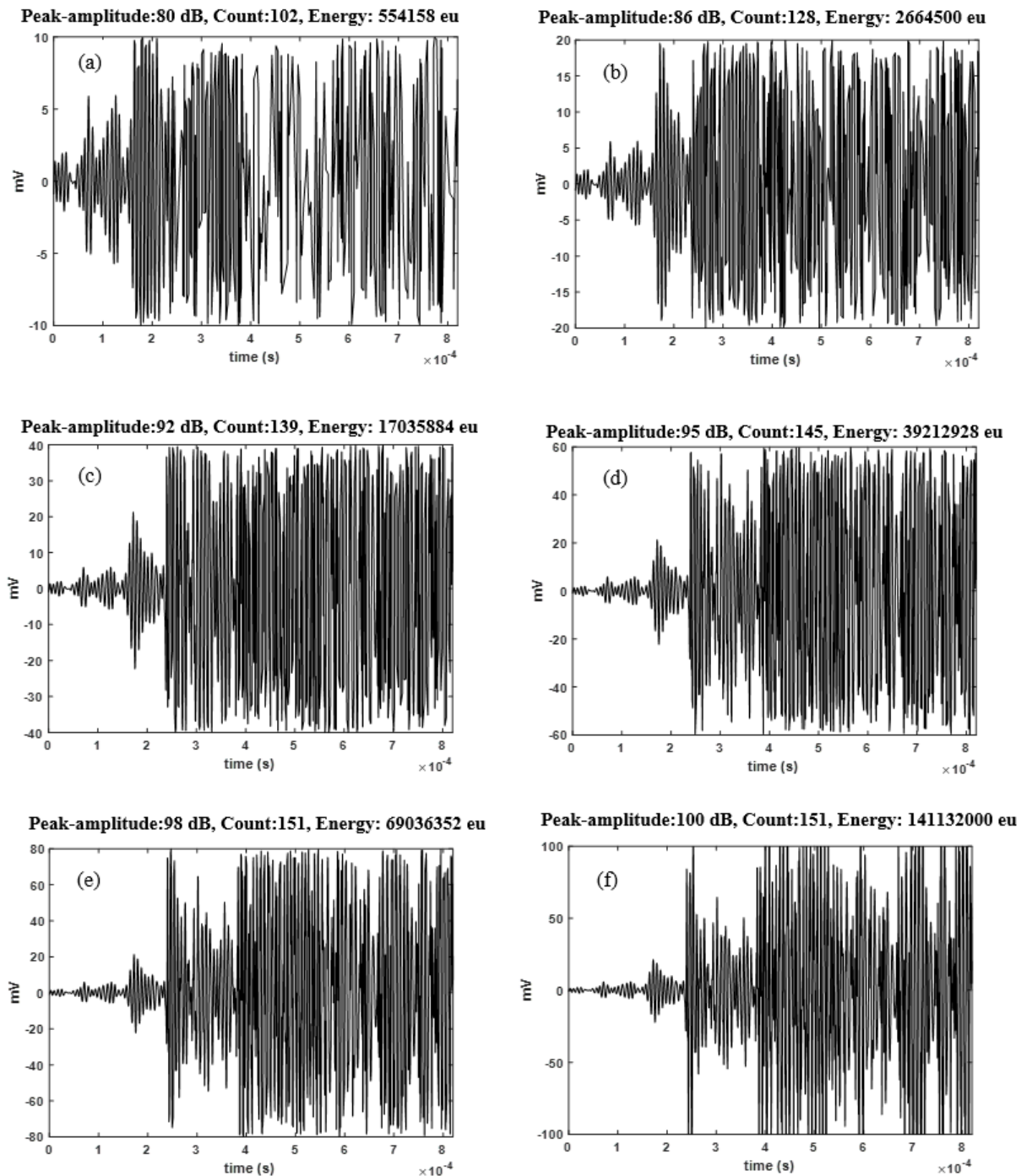


Figure 5-7: An AE waveform with a VDR of (a) -10 to +10, (b) -20 to +20, (c) -40 to +40, (d) -60 to +60, (e) -80 to +80 and (f) -100 to +100

Secondly, the choice of bin width to generate the discrete probability distribution is also of great importance. If the bin width is too large, there will be too many samples within each

bin that the disorderness of the probability distribution will be lost. If the bin width is too small, there will be too little sample within each bin that the disorderness of the probability will be unreliable. In order to extract a reliable measure of disorderness from the probability distribution, the bin width should be set equal to the AE data acquisition systems resolution.

In addition, it is worth noting that the present investigation was carried out under controlled experimental environment, where the sensors were placed close to the damage source. Under real condition monitoring of engineering structures using AE, damage source may be located far away from the AE sensors and the AE signals can be subjected to attenuation and dispersion. Attenuation and dispersion is likely to affect AE entropy value (as with all other traditional AE features). Moreover, noise generated from the grips and internal reflections within the test specimen were filtered out in these analysis. Under real operational conditions, noise sources may be difficult to filter out and can bring difficulty in interpreting the damages using AE entropy. Further research needs to be carried out to investigate the effectiveness of AE entropy on complex engineering structures. Firstly, the effect of attenuation and dispersion on the calculated AE entropy needs to be understood. Secondly, the performance of AE entropy in noisy environments needs to be assessed.

### 5.3 Advantage of Renyi's entropy over Shannon's entropy

It is clear from this research that, AE waveforms during damage (*e.g.* rapid yielding and fracture) are associated with higher AE entropy. Since AE entropy is a measure of disorderness, it is definite that AE waveforms during damage are highly disordered. Both Renyi's and Shannon's entropy can effectively measure the disorderness in the AE waveform. In fact, Shannon's entropy has been used in a few recent studies to measure the disorderness of the AE waveform [100][74][101].

Entropy of a variable is the average number of bits needed to represent it. According to Kolmogorov's theory [143], the average of variable  $\{x_1, x_2, x_3, \dots, x_n\}$ , is represented using equation 5-4.

$$Mean = g^{-1} \sum_{i=1}^n [w(x_i)g(x_i)]$$

Equation 5-4

Where:

$w(x_i)$  represent the weight of the variable, such that  $\sum_{a=1}^n w(x_i) = 1$ .

## Discussion

$g(x)$  is a strictly continuous monotonic function and  $g^{-1}(x)$  is its inverse function. For arithmetic mean  $g(x) = x$  and  $g^{-1}(x) = x$ .

When Kolmogorov's theory is used to determine the average or the arithmetic mean number of bit needed to represent a variable. Equation 5-4 takes the form as shown in equation 5-5.

$$Mean = g^{-1} \sum_{k=1}^m \left[ P(x_k) g \left( \log \left( \frac{1}{P(x_k)} \right) \right) \right] \quad \text{Equation 5-5}$$

Where:

$P(x_k)$  represents the discrete probability distribution of the voltage values with the kth number of bin.

$m$  represents the total number of bins.

$\log \left( \frac{1}{P(x_k)} \right)$  represents the number of bits need to represent the variable  $x_k$ .

Since,  $g(x)$  (*i.e.*  $g(-\log P(x_k))$ ) in equation 5-5) is a strictly continuous monotonic function, Renyi proved that it has two solution [107]. The first solution is  $g(x) = ax$  (*i.e.*  $g(-\log P(x_k)) = -a \log P(x_k)$  for equation 5-5), with  $a \neq 0$ . Substituting the first solution in equation 5-5 yields Shannon's entropy (shown in equation 3-3). Shannon's entropy is the average number of bits required to represent a variable, in other word it is the arithmetic mean of the total number of bits. The second solution is  $g_a(x) = 2^{(a-1)x}$  (or  $g_a(-\log P(x_k)) = 2^{(a-1)-\log P(x_k)}$  for equation 5-5). Substituting the second solution in equation 5-5 results in Renyi's entropy (shown in equation 3-1). Renyi's entropy is considered to be an exponential mean of the total number of bits. Both Renyi's and Shannon's entropy can be defined with five sets of postulates (definition of the postulates are provided in the Appendix A.5). The first four postulates are common between both the entropy measures. However, they differ in their fifth postulates as a result of the choice of  $g(x)$ . In contrast to the Shannon's entropy, Renyi's entropy has an additional term 'a' in the equation (refer to equation 3-1 and 3-3). The term 'a' in Renyi's entropy (shown in equation 3-1) appears as a power of the discrete probability distribution. As a result, the choice of 'a' makes Renyi's entropy unique. Equation 5-6, 5-7 and 5-8 shown the form of equation 3-1 when 'a' is 2,3 and 4 respectively.

## Discussion

$$H_2(x) = -\log\left(\sum_{k=1}^n (P(x_k))^2\right) \quad \text{Equation 5-6}$$

$$H_3(x) = -\frac{1}{2}\log\left(\sum_{k=1}^m (P(x_k))^3\right) \quad \text{Equation 5-7}$$

$$H_4(x) = -\frac{1}{3}\log\left(\sum_{k=1}^m (P(x_k))^4\right) \quad \text{Equation 5-8}$$

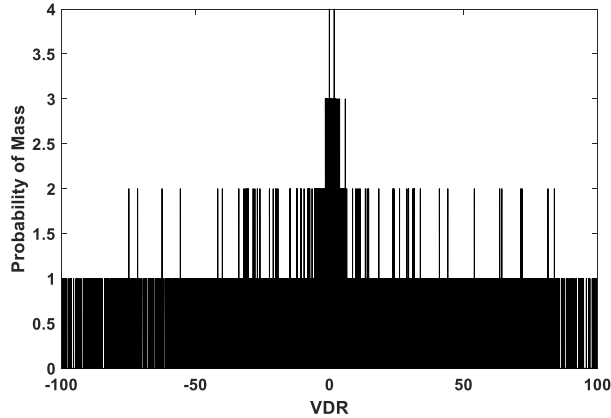


*Figure 5-8: Probability distribution ( in Shannon's entropy when 'a' is 1)*

In order to choose an appropriate value of 'a' for this research, the waveform in figure 5-6 (f) was analysed. Figure 5-7 illustrates the discrete probability distribution of this waveform against VDR. It is evident from this figure that the weight provided to all the probability of mass are the same. For instance, the height of the probability of mass for the highest probability voltage is 4, which is 4 times that of probability of mass for the lower probability voltage. The information extracted from this discrete probability distribution can also be regarded as arithmetic mean amount of information, which is called Shannon's entropy.

It is evident from this figure that the probability of mass for the voltage values close to zero are higher, compared to the ones that are further away from zero. It is reasonable to provide more weight to the dominant probability of mass for the voltage values. Because these voltages have occurred with higher frequency and can disclose the true nature of

## Discussion

disorderness in the waveform. Since, the term 'a' in Renyi's entropy is the power of the discrete probability distribution, increasing it can alter the weight provided to the individual probability of mass. Figure 5-8 shows the weight provided to the probability of mass for the waveform in figure 5-6 (f), as a result of raising it to the power 2, 3 and 4 (this circumstances appears in equation 5-6, 5-7 and 5-8, where the discrete probability distribution is raised to the power 2, 3 and 4 respectively). It is clear from graph (a) of this figure that raising the discrete probability distribution to the power 2, provides more weight to the dominant probability of mass. It can be observed in graph (b) of this figure that, raising the discrete probability distribution to the power 3, increases the weight of the dominant probability of mass even further. It is also evident from this graph that the weight provided to the lower probability of mass is considerably less compared to that of graph (a). In graph (c) of this figure, it can be observed that the weight provided to the dominant probability of mass are significantly more compared to that of graph (a) and (b). Whereas, the weight provided to the lower probability of mass are significantly less.

It is clear from this analysis that  $a=2$  provides more weight to the dominant probability of mass. However, a higher value of 'a' (e.g.  $a>2$ ) provides a much more weight to the dominant probability of mass. This can significantly weaken the contribution from the lower probability of mass. Considering this trade of,  $a=2$  was chosen for this research, as it provides more weight to the dominant probability of mass and also taken in to account of the contribution from the lower probability of mass.

As mentioned in section 3.1.2, Renyi's entropy with  $a=2$  is known as quadratic Renyi's entropy. In order to investigate the performance of Shannon's and quadratic Renyi's entropy to capture disorderness, waveform 1 in figure 3-6 and its corresponding SNR of 10, 20, 30, and 40 were analysed. Waveform 1 in figure 3-6 is considered to be highly ordered compared to its corresponding SNR. Therefore, the difference in each entropy measurement technique (e.g. Shannon's and quadratic Renyi's) between the waveform 1 in figure 3-6 and its corresponding SNR should provide a true measure of performance against capturing the disorderness. Figure 5-9 shows the delta entropy against SNR for both Shannon's and quadratic Renyi's entropy. The delta entropy corresponds to the difference in the entropy between waveform 1 and its corresponding SNR.

It can be observed in these graph that for each of the SNR, the delta entropy for quadratic Renyi is noticeably higher than that of Shannon's entropy. In other word, the spread in data between the ordered and disordered waveform will be much higher for quadratic Renyi's compared to Shannon's entropy. Therefore, it can be concluded that quadratic Renyi's entropy is much more efficient in capturing the disorderness.

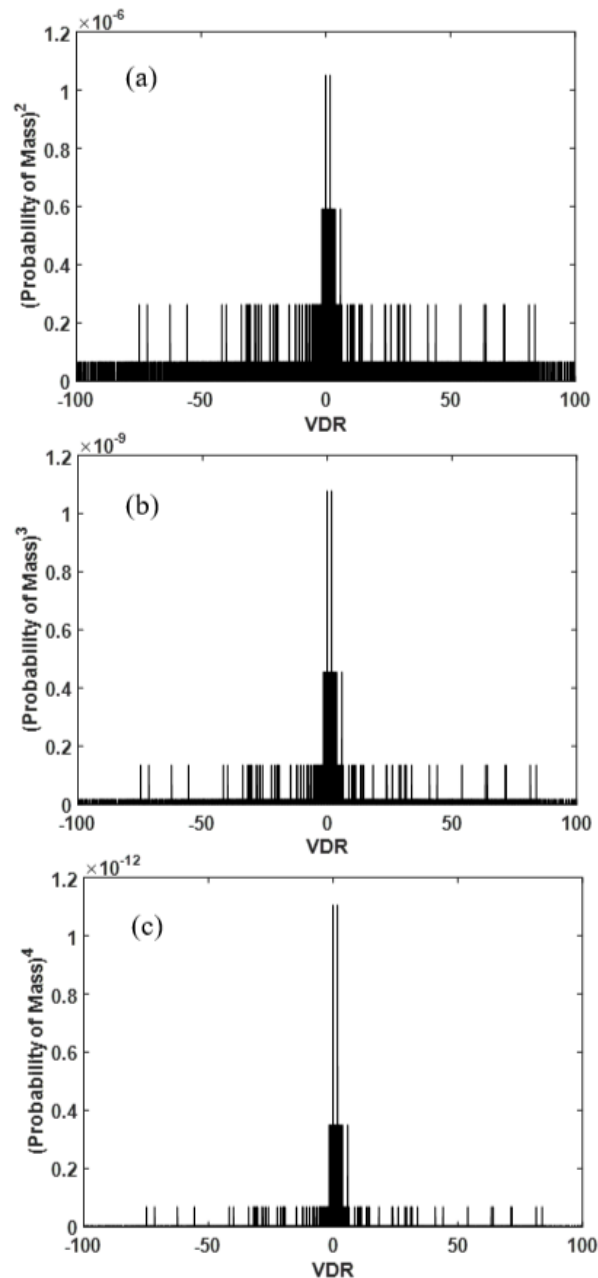


Figure 5-9: (a) Discrete probability distribution raised to the power 2 against VDR (used in Renyi's entropy when 'a' is 2), (b) Discrete probability distribution is raised to the power 3 against VDR ((used in Renyi's entropy when 'a' is 3) (c) Discrete probability distribution is raised to the power 4 against VDR((used in Renyi's entropy when 'a' is 4

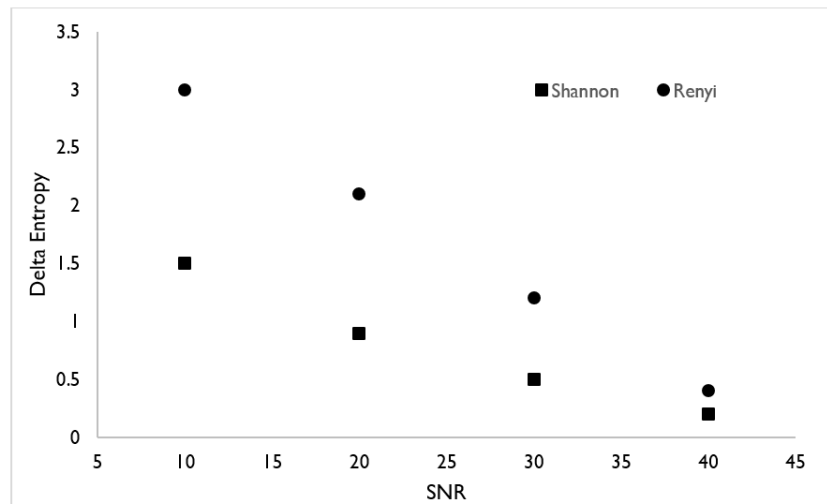


Figure 5-10: Delta entropy against SNR of each entropy technique

## 5.4 Effect of noise on Renyi's entropy

The noise generated from the grips of the test specimens were filtered out in these analysis. However, it is worth noting that the waveform of the filtered events may still contain some noise. These noise are impossible to filter out with the traditional AE filtration techniques (e.g 1D localization), as they are embedded on the waveform. The presence of noise in the waveform can affect the disorderness of the discrete probability distribution. Therefore, it has the potential to influence the calculated value of AE entropy from a waveform. Like the AE entropy, noise in the waveform can also influence the traditional AE features. This is because the shape of the waveform is also likely to change with noise content. This analysis will investigate the effect of noise in the waveform on the calculated AE entropy.

In order to eliminate the noise embedded in the AE waveform, few studies have proposed a signal processing approach [100][144][145]. These studies are based on de-noising (e.g. conditioning) the AE waveform with Discrete Wavelet Transform (DWT) prior to extracting the features. The result of these studies suggests, DWT to be very effective in reducing the noise in the waveform, therefore this technique is adopted in this research. De-noising using DWT is based on the wavelet theory. In this approach, a series of wavelet is used to obtain the wavelet coefficient, of the signal to be de-noised. The series of wavelet is generated by scaling and translating of a mother wavelet. Scaling represents expanding or contracting the mother wavelet, whereas translating represents moving the mother wavelet in discrete time interval from the beginning to the end of the waveform. The wavelet coefficient obtained are

referred to as the  $DWT(a,b)$ , which is a function of the translating  $b$  with a fixed scale factor  $a$ . The DWT helps analyse the waveform at a different level of frequencies by decomposing it into several level approximations and details. The DWT also provides similarity between the waveform and the series of wavelets, in other words it is the convolution between the waveform and the series of wavelets.

The procedure for waveform de-noising using DWT is accomplished with three steps. Firstly, the waveform is decomposed into several level  $N$  using a series of wavelet from a mother wavelet. Each level contains an approximation coefficients representing the low pass filter and a detail coefficient representing a high pass filter. Secondly, thresholding is carried out on every detail coefficient using a threshold rule (e.g. minimax, Heursure, sqtwolog, SURE), in conjunction with a hard or a soft thresholding. Finally, the signal is reconstructed by inverse DWT from the updated detail coefficient on every level and updated approximation coefficient on the final level. In this research, db8 was chosen as the mother wavelet, decomposition level was chosen to be 8 and a soft thresholding method was implemented. These parameters were chosen as they yielded the best de-noising performance of the AE waveform among many other set of de-noising parameters [144].

Graph (a) and (b) in figure 5-10 illustrates the original and de-noised waveform generated during yielding of the first and second fatigue specimen respectively. The AE entropy of the original waveform in first and second fatigue specimen is 10.3 and 10.5 respectively. Whereas, that of the de-noised waveform it is 8.7 and 8.4 respectively. It is clear from this analysis that de-noising the waveform, slightly reduces the AE entropy. This is because de-noising procedure decreases the disorderness in the probability distribution of the waveform. It is also evident that despite the presence of noise, the majority of the disorderness in the original waveform arises from microstructural changes in the material (as de-noising only slightly reduces the AE entropy). As a result, there is no need to perform the de-noising when AE entropy is used for damage monitoring. Similar conclusion is drawn in [100], where the effect of de-noising was investigated for Shannon's entropy.

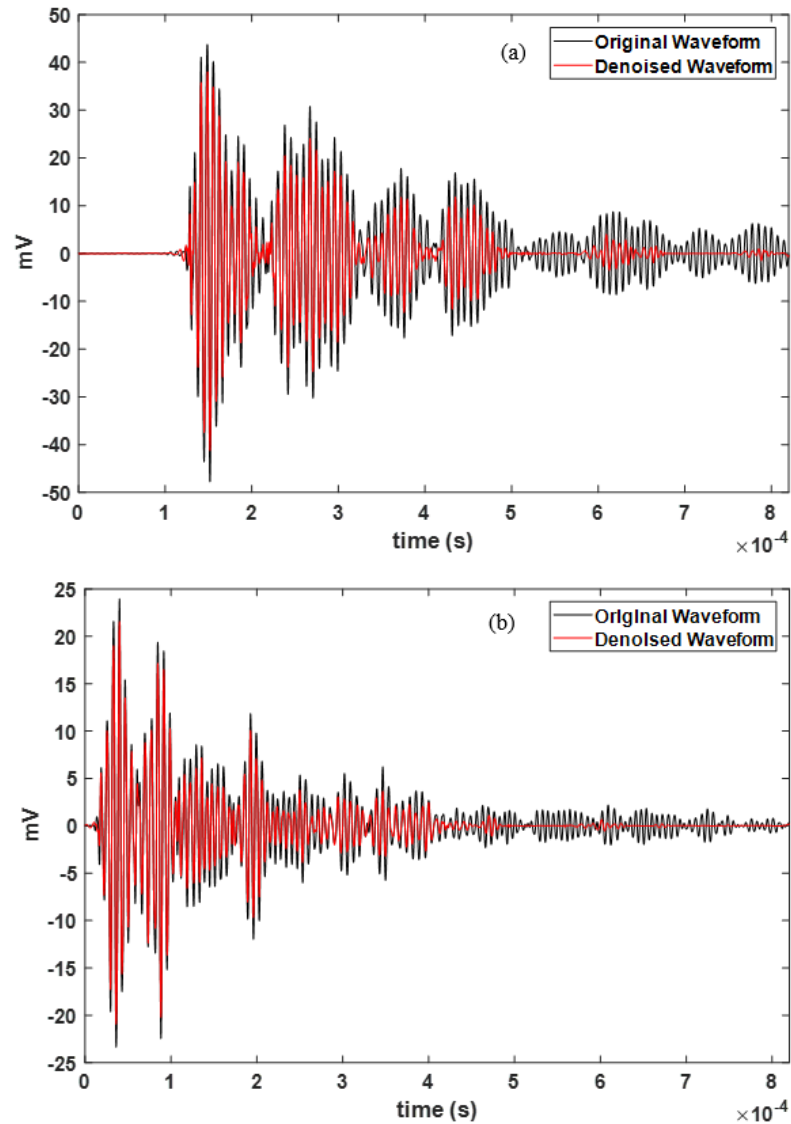


Figure 5-11: (a) Original and de-noised waveform of the first fatigue specimen (b) Original and de-noised waveform of the second fatigue specimen

## 5.5 Chapter summary

This chapter identifies the potential and demonstrates the capability of AE entropy to identify damages in the primary wall, as a result of sloshing impact. Special attention is given to the type of analysis (*e.g.* correlation or cumulative) that can provide reliable indication of damages in the primary wall. For instance, it is recognised that cumulative analysis may not be a suitable technique for identification of the plastic zone in the primary wall (despite being able to identify plastic zone formation in standard specimen), because sloshing impacts are separated by random zero pressure values. As a result, there may not be a significant jump in the cumulative AE entropy if the zero pressure intervals increases during plastic zone formation. This chapter also recognises that the plastic zone formation cannot be identified

with the correlation AE entropy (along with other traditional AE features). In fact, the only damage mechanism in the primary wall that can be identified using AE entropy (including the traditional AE features) is the localized deformation/yielding as a result of a single sloshing impact. The localized deformation/yielding is considered to be a dominant damage mechanism in the primary wall and since AE entropy is sensitive to this information, it can be implemented to monitor this structure against this damage mechanism.

This chapter also discusses the factors influencing the AE entropy computation (*e.g.* the bin width and VDR) and how to minimise their effects. For instance, the effect of bin width can be avoided by choosing it to be close to the AE data acquisition systems resolution and the effect of VDR can be avoided by choosing it to be equal to built-in maximum limit of the voltage range. The justification for the quadratic Renyi's entropy (among several other techniques) to measure the disorderness in a waveform is also provided in this chapter. It suggests that quadratic Renyi's entropy provides more weight to the dominant probability of mass, however it is close to Shannon's entropy, as a result the contribution from the lower probability of mass is not significantly minimised. Finally, the chapter shows that de-noising a waveform by DWT does not reduce its AE entropy significantly. This suggest majority of the disorderness in a waveform arises from the microstructural changes.

## 6 Conclusion and Future Work

### 6.1 Conclusions and contribution

This research is motivated by the potential risk of failure of the cargo tank, in supersized LNG carriers. Failure can not only cause shutdown of the vessel but also introduce risk to the safety of life and property. The IMO has set guidelines focusing on a maintenance strategy of the LNG carrier and the safe carriage of bulk LNG through ocean. Despite these guidelines there have been several potential risks of catastrophic failure. In order to successfully reduce the risk of failure, there is a growing demand to replace the traditional maintenance strategy with a CBM strategy.

The initial damages in a cargo tank that has the potential to cause catastrophic failure is the yielding/deformation and crack initiation in its primary wall. These damages occur as a result of sloshing impact of LNG cargo inside the tank. If real time information regarding these damages can be achieved, an appropriate maintenance can be carried out to avoid the risk of catastrophic failure. To extract the real time information, the SHM technique must be sensitive to the damage mechanism which can span several lengths of time. The current monitoring technique of the cargo tank provides information regarding the leakage of LNG from its primary wall. However, it does not provide any information regarding the damages that has resulted in the leakage. Leakages not only increases the risk of catastrophic failure but also results in the loss of cargo. Most of the research in LNG cargo containments are based on understanding the sloshing response. However, sloshing response is not a direct indication of critical damage as a numerical model would often be required to translate it into a useful condition monitoring indication. This would make its application in SHM extremely difficult.

The only SHM technique that can successfully extract the real time information regarding yielding/deformation from the material of the primary wall is AE. Despite this capability of

AE, it has never been implemented as a SHM technique on the primary wall. This research addresses the drawback of the state of the art AE monitoring technique and improves it so that it can be adopted for the SHM application on the primary wall of the cargo tank. The improved technique is based on an AE feature which is independent of some user defined parameter (*i.e.* threshold and HDT) used in AE data acquisition system, unlike many traditional AE features. The AE feature is a measure of randomness of the waveform, calculated using quadratic Renyi's entropy and has proven to be effective in identifying damages in austenitic stainless steel (*i.e.* material of the primary wall). The presented AE feature is referred to as AE entropy in this research. Since AE entropy reduces the human involvement with the data acquisition system and can identify damages, it has the potential to be implemented in the commercial AE data acquisition system. The following bullet points summarise the key findings of this research:

- The evaluation process adopted in this study suggests that AE entropy is independent of user defined acquisition threshold and extracts the collective information from a waveform. This independency of AE entropy arises as it is directly calculated from the discrete voltage values which are both in and outside the threshold.
- The evaluation process also suggests that AE entropy is independent of the user defined HDT. This is mainly because the computation of AE entropy takes into account the discrete voltage values in a waveform even after the expiration of HDT. The independence of AE entropy is an important property, as the loss of information from sub waveforms occurring at different time interval within a waveform can be avoided.
- AE entropy is dependent on the VDR and bin width. The effect of VDR on AE entropy can be avoided, by setting it to the built-in maximum limit of the voltage range, in AE data acquisition system. Whereas the effect of bin width can be avoided by setting it close to the resolution of the AE data acquisition system.
- In fatigue tests, the sharp increase in global strain at the initial stage can be attributed to the rapid yielding of the specimen. The sharp increase in this global strain is accompanied by the significantly dominant individual AE entropy. This indicates that AE entropy has the potential to identify yielding, which is considered to be a

dominant damage mechanism in the primary wall. Since AE entropy is sensitive to yielding, it can be successfully implemented to monitor the primary wall against this damage mechanism. At the formation of plastic zone and crack initiation (identified by DIC) there is no noticeable increase in the AE entropy. This suggests that it may not be a suitable technique for identification of crack initiation in the primary wall.

- Both the cumulative count and AE entropy increases noticeably before the damage manifests into plastic zone formation. At the formation of plastic zone (identified by DIC), there is a sharp increase in both of these cumulative features. A similar trend in these cumulative features suggest that the traditional analysis of cumulative count can be replaced with cumulative AE entropy, in the experimental investigation of fatigue damage evaluation, as the AE entropy can identify damages at reduced human involvement with the data acquisition system. Despite the potential of cumulative AE entropy in identifying the fatigue damage evolution, it cannot be used to monitor the primary wall. Primarily because the sloshing impact on the primary wall are separated by a zero pressure interval. As a result, there might not be a noticeable change in the cumulative feature if the duration of zero pressure values increases during damage formation.
- In a tensile test, AE entropy possessed the same trend as most of the widely used traditional AE features. From the onset of loading to just after yielding there were plenty of AE activity due to dislocation movement, however they did not have dominant AE entropy. Whereas the fracture of the specimen was accompanied by a small number of AE activity but they had dominant AE entropy.
- Compared to the yielding of tensile specimen, the yielding of fatigue specimen was accompanied by dominant AE entropy. This was due to an enhanced average velocity of the moving dislocation ( $v_{av}$ ), as a result of the higher strain rate ( $\dot{\epsilon}$ ) of fatigue specimens. Duration of a cyclic loading in the fatigue test adopted in this study was comparable to the duration of the sloshing impact. Therefore, a strong sloshing impact has the potential to cause deformation in the primary wall with a high strain

rate (than that of the strain rate of tensile test), which can produce dominant AE entropy.

- AE entropy is a measure of disorderness in the waveform, therefore higher AE entropy during yielding and fracture in a fatigue test and fracture in tensile test indicates that these waveforms are highly disordered. Both Renyi's and Shannon's entropy can effectively measure the disorderness. However, Renyi's entropy is much more flexible in capturing the disorderness because of the term 'a' in its computation. The spread in the data between the ordered and disordered waveform is higher for quadratic Renyi's entropy compared to Shannon's entropy. As a result, quadratic Renyi's entropy is much more efficient in capturing the disorderness.
- Majority of the disorderness in a waveform arises from the micro-structural damage, as a result, there is no need to perform the de-noising of the waveform prior to the calculation of AE entropy.

## 6.2 Future Work

The following suggestions are recommended for future work:

- In the primary wall, damage source can be far away from the AE sensor, therefore, the elastic waves from damages can be subjected to attenuation until they reach the AE sensor. Attenuation is likely to affect the AE entropy value (as with all other traditional AE features). To avoid the effect of attenuation there has to be an optimum sensor deployment in the primary wall. This can be achieved by having a clear understanding about the attenuation in the primary wall as per standard ASTM E1930/ E1930M [64]. Therefore, the future work should aim to establish the optimum sensor deployment, specially the number of sensors and the sensor configuration in a single plate of primary wall.
- There should be a clear understanding about the nature and source of noise generated in the primary wall under operational condition. This can be achieved through a calibration test, where AE data from the primary wall is be collected during voyage

and the noise content is analysed. A clear understanding of the noise content would enable in an efficient filtration of the AE data so that damages can be interpreted with AE entropy without any difficulty.

- The future investigations should aim to determine the performance of AE entropy to prediction damages in austenitic stainless steel, under cryogenic temperature (*i.e.* -162°C).
- The work performed in this research should be extended to thicker specimen of austenitic stainless steel and other materials to establish the effect of such changes on the effectiveness and reliability of the new technique.

## References

- [1] World Energy Council, “World Energy Resources,” 2016.
- [2] U.S. Energy Information Administration, “International Energy Outlook,” 2016.
- [3] BP Energy Economics, “BP Statistical Review of World Energy (67th Edition),” 2018.
- [4] International Gas Union, “World LNG Report,” 2018.
- [5] A. Benjamin Wilson, “Liquefied Natural Gas in Europe,” 2015.
- [6] M. C. Ryu, H. Jung, Y. S. Kim, and Y. Kim, “Sloshing design load prediction of a membrane type LNG cargo containment system with two-row tank arrangement in offshore applications,” *Int. J. Nav. Archit. Ocean Eng.*, vol. 8, pp. 537–553, 2016.
- [7] J.-H. Kim, S.-K. Kim, M.-H. Kim, and J.-M. Lee, “Numerical model to predict deformation of corrugated austenitic stainless steel sheet under cryogenic temperatures for design of liquefied natural gas insulation system,” *Mater. Des.*, vol. 57, pp. 26–39, 2014.
- [8] “Carrying liquefied natural gases by various type LNG ships.” [Online]. Available: <http://www.liquefiedgascarrier.com/Liquefied-Natural-Gas-Carriers.html>. [Accessed: 24-Jan-2019].
- [9] “GTT | Mark III systems.” [Online]. Available: <https://www.gtt.fr/en/technologies-services/our-technologies/mark-iii>. [Accessed: 24-Jan-2019].
- [10] M.-C. Oh, J.-K. Seo, K.-J. Kim, S.-M. Lee, and M.-H. Kim, “In Situ Measurement of Sloshing Impact on LNG Insulation Panel by using High Speed Fiber Optics,” *J. Intell. Mater. Syst. Struct.*, vol. 21, 2010.
- [11] M. Graczyk, T. Moan, and M. Wu, “Extreme sloshing and whipping-induced pressures and structural response in membrane LNG tanks Extreme sloshing and whipping-induced pressures and structural response in membrane LNG tanks,” *Ships Offshore Struct.*, vol. 2, pp. 201–216, 2007.
- [12] J.-J. Park *et al.*, “Study on tank shape for sloshing assessment of LNG vessels under unrestricted filling operation,” *J. Mar. Sci. Technol.*, vol. 20, pp. 640–651, 2015.
- [13] DNV GL, “Class guideline: sloshing analysis of LNG membrane tanks,” 2016.
- [14] J. K. Paik, J. M. Lee, Y. S. Shin, and G. Wang, “Design Principles and Criteria for Ship Structures under Impact Pressure Loads Arising from Sloshing , Slamming and Green Seas,” *Trans SNAME*, vol. 112, no. M, pp. 292–313, 2004.
- [15] H. Bum Lee, B. Jin Park, S. Hyung Rhee, J. Hong Bae, K. Won Lee, and W. Jo Jeong, “Liquefied natural gas flow in the insulation wall of a cargo containment system and its evaporation,” *Appl. Therm. Eng. J.*, vol. 31, pp. 2605–2615, 2011.
- [16] J. Sohn, D. Bae, S. Bae, and J. Paik, “Nonlinear structural behaviour of membrane-type LNG carrier cargo containment systems under impact pressure loads at –163 °C,” *Ships Offshore Struct.*, vol. 12, no. 5, pp. 722–733, 2016.
- [17] S. W. Choi, H. S. Kim, and W. Il Lee, “Analysis of leaked LNG flow and

## References

- consequent thermal effect for safety in LNG cargo containment system,” *Ocean Eng.*, vol. 113, pp. 276–294, 2016.
- [18] S. Han, “Assessing Structural Safety of Inner Hull Structure Under Cryogenic Temperature,” in *Proceedings of the ASME 2011 30th International Conference on Ocean, Offshore and Arctic Engineering*, 2011, pp. 1–7.
- [19] D. G. Kim, W. Yoo, P. Swinehart, B. Jiang, T. Haber, and A. Mendez, “Development of an FBG-based low temperature measurement system for cargo containment of LNG tankers,” vol. 6770, no. 2007, p. 67700D, 2007.
- [20] International Maritime Organization, “Resolution MSC.370(93) (adopted on 22 May 2014),” 2015.
- [21] T. Gavory and P. E. De Seze, “Sloshing in membrane LNG carriers and its consequences from a designer’s perspective,” 2009.
- [22] K. S. Wang, “Loss Prevention Through Risk Assessment Surveys of LNG Carriers in Operation , Under Construction , Conversion and Repair.”
- [23] S. Gowid, R. Dixon, and S. Ghani, “Profitability, reliability and condition based monitoring of LNG floating platforms: A review,” *J. Nat. Gas Sci. Eng.*, vol. 27, pp. 1495–1511, 2015.
- [24] E. E. Hurdle, L. M. Bartlett, and J. D. Andrews, “Fault diagnostics of dynamic system operation using a fault tree based method,” *Reliab. Eng. Syst. Saf. J. homepage www.elsevier.com/locate/ress Fault*, vol. 94, pp. 1371–1380, 2009.
- [25] Society of International Gas Tanker and Terminal Operators Ltd, “Gas concentration in the insulation space of membrane LNG career,” 2007.
- [26] American Bureau of Shipping, “Strength assessment of membrane-type LNG containment systems under sloshing loads,” 2014.
- [27] M. L. K. H. Bogaert, S. Léonard, L. Brosset, “Sloshing and scaling: results from the Slos shel project,” 2010.
- [28] Š. Malenica and S. H. Kwon, “An Overview of the Hydro- Structure Interactions During,” *Brodogradnja*, vol. 64, no. 1, pp. 22–30, 2013.
- [29] J. F. Kuo *et al.*, “LNG tank sloshing assessment methodology-the new generation,” *Int. J. Offshore Polar Eng.*, vol. 19, no. 4, pp. 241–253, 2009.
- [30] M. Graczyk and T. Moan, “A probabilistic assessment of design sloshing pressure time histories in LNG tanks,” *Ocean Eng.*, vol. 35, no. 8–9, pp. 834–855, 2008.
- [31] M. H. Kim, D. H. Kim, S. W. Kang, and J. M. Lee, “An interlaminar strain measurement for insulation panels of LNG carriers,” *Strain*, vol. 42, no. 2, pp. 97–106, 2006.
- [32] N. Yamamoto, T. Koiwa, H. Dobashi, O. Muragishi, and Y. Takaoka, “A study of a fatigue management system for long LNG carriers using a new fatigue damage sensor,” *Ships Offshore Struct.*, vol. 2, no. 4, pp. 361–370, 2007.
- [33] A. Anastasopoulos, D. Kourousis, S. Botten, and G. Wang, “Acoustic emission monitoring for detecting structural defects in vessels and offshore structures,” *Ships Offshore Struct.*, vol. 4, no. 4, pp. 363–372, 2009.
- [34] T. Haneef *et al.*, “Study of the tensile behavior of AISI type 316 stainless steel using acoustic emission and infrared thermography techniques,” *J. Mater. Res. Technol.*, vol. 4, no. 3, pp. 241–253, 2015.
- [35] C. K. Mukhopadhyay, T. Jayakumar, B. Raj, and K. K. Ray, “Acoustic emission-stress intensity factor relations for tensile deformation of notched specimens of AISI type 304 stainless steel,” *Mater. Sci. Eng. A*, vol. 293, no. 1, pp. 137–145, 2000.
- [36] C. K. Mukhopadhyay, K. K. Ray, T. Jayakumar, and B. Raj, “Acoustic emission from tensile deformation of unnotched and notched specimens of AISI type 304 stainless steels,” *Mater. Sci. Eng. A*, vol. 255, no. 1–2, pp. 98–106, 2002.

## References

- [37] B. Venkataraman, C. K. Mukhopadhyay, and B. Raj, "Effect of variation of strain rate on thermal and acoustic emission during tensile deformation of nuclear grade AISI type 316 stainless steel," *Mater. Sci. Technol.*, vol. 20, no. 10, pp. 1310–1316, 2004.
- [38] C. K. Mukhopadhyay, T. Jayakumar, B. Raj, and K. K. Ray, "The influence of notch on the acoustic emission generated during tensile testing of nuclear grade AISI type 304 stainless steel," *Mater. Sci. Eng. A*, vol. 276, no. 1–2, pp. 83–90, 2002.
- [39] V. Moorthy, T. Jayakumar, and B. Raj, "Acoustic emission technique for detecting micro-and macroyielding in solution-annealed AISI Type 316 austenitic stainless steel," 1995.
- [40] C. Hellier, *Handbook of nondestructive evaluation*. McGraw-Hill, 2013.
- [41] A. G. Beattie, "Acoustic Emission Non-Destructive Testing of Structures using Source Location Techniques," 2013.
- [42] B. Dodd, "Introduction to elastic wave propagation," *Eng. Struct.*, vol. 16, no. 7, p. 564, 2003.
- [43] K. M. Holford, "Acoustic emission - basic principles and future directions," *Strain*, vol. 36, no. 2, pp. 51–54, 2000.
- [44] H.-S. Lee, J.-H. Yoon, J.-S. Park, and Y.-M. Yi, "A study on failure characteristic of spherical pressure vessel," *J. Mater. Process. Technol.*, vol. 164, pp. 882–888, 2005.
- [45] J. M. Rajtar and R. Muthiah, "Pipeline Leak Detection System for Oil and Gas Flowlines," *J. Manuf. Sci. Eng.*, vol. 119, no. 1, p. 105, Feb. 1997.
- [46] L. Zhang, V. Sazonov, J. Kent, T. Dixon, and V. Novozhilov, "Analysis of boiler-tube erosion by technique of acoustic emission Part I. Mechanical erosion," *Wear*, vol. 250, no. 1–12, pp. 762–769, 2001.
- [47] C. M. Chen and R. Kovacevic, "Joining of Al 6061 alloy to AISI 1018 steel by combined effects of fusion and solid state welding," *Int. J. Mach. Tools Manuf.*, vol. 44, no. 11, pp. 1205–1214, 2004.
- [48] T. H. G. J. Tang, S. Soua, C. Mares, "An experimental study of acoustic emission methodology for in service condition monitoring of wind turbine blades," *Renew. Energy*, vol. 99, pp. 170–179, 2016.
- [49] X. Q. Ma, S. Cho, and M. Takemoto, "Acoustic emission source analysis of plasma sprayed thermal barrier coatings during four-point bend tests," *Surf. Coatings Technol.*, vol. 139, p. 5562, 2001.
- [50] M. F. Shehadeh, "Monitoring of Long Steel Pipes using Acoustic Emission," Heriot-Watt University, 2006.
- [51] M. G. Baxter, R. Pullin, K. M. Holford, and S. L. Evans, "Delta T source location for acoustic emission," *Mech. Syst. Signal Process.*, vol. 21, no. 3, pp. 1512–1520, 2007.
- [52] A. Tobias, "Acoustic-emission source location in two dimensions by an array of three sensors," *Non-Destructive Test.*, vol. 9, no. 1, pp. 9–12, 1976.
- [53] D. Aljets, A. Chong, S. Wilcox, and K. Holford, "Acoustic Emission Source Location in Plate-Like Structures Using a Closely Arranged Triangular Sensor Array," *J. Acoust. Emiss.*, vol. 28, p. 28, 2010.
- [54] D. Gagar, F. Bai, Y. Zhao, and P. Foote, "New methods for onset detection of acoustic emission signals," *8th Eur. Work. Struct. Heal. Monit. (EWSHM 2016)*, no. July 2016, pp. 5–8, 2016.
- [55] V. Salinas, Y. Vargas, J. Ruzzante, and L. Gaete, "Localization algorithm for acoustic emission," *Phys. Procedia*, vol. 3, no. 1, pp. 863–871, 2010.
- [56] H. Kolsky, "Stress waves in solids," *J. Sound Vib.*, vol. 1, no. 1, pp. 88–110, Jan. 1964.

## References

- [57] D. Gagar, "Validation and Verification of the Acoustic Emission Technique for Structural Health Monitoring," Cranfield University, 2013.
- [58] C. Willberg, S. Duczec, J. M. Vivar-Perez, and Z. A. B. Ahmad, "Simulation Methods for Guided Wave-Based Structural Health Monitoring: A Review," *Appl. Mech. Rev.*, vol. 67, no. 1, p. 010803, 2015.
- [59] S. Pant, J. Laliberte, and M. Martinez, "Structural health monitoring (SHM) of composite aerospace structures using Lamb waves," *19th Int. Conf. Compos. Mater.*, vol. 1, no. November 2015, p. 7532, 2013.
- [60] P. Gómez, J. P. Fernández, and P. D. García, "Lamb Waves and Dispersion Curves in Plates and its Applications in NDE Experiences Using Comsol Multiphysics," *Comsol Conf.*, pp. 1–5, 2011.
- [61] H. Dunegan and D. Harris, "Acoustic emission-a new nondestructive testing tool," *Ultrasonics*, vol. 7, no. 3, pp. 160–166, Jul. 1969.
- [62] K. M. Holford, "Acoustic Emission in Structural Health Monitoring," *Key Eng. Mater.*, vol. 413–414, pp. 15–28, Jun. 2009.
- [63] F. Chang, *Structural health monitoring ,condition based maintenance and intelligent structures : proceedings of the 8th International Workshop on Structural*. 2011.
- [64] "ASTM E1930 / E1930M - 17 Standard Practice for Examination of Liquid-Filled Atmospheric and Low-Pressure Metal Storage Tanks Using Acoustic Emission," 2017.
- [65] S. Shi *et al.*, "Quantitative monitoring of brittle fatigue crack growth in railway steel using acoustic emission," *Proc. Inst. Mech. Eng. Part F J. Rail Rapid Transit*, vol. 232, no. 4, pp. 1211–1224, Apr. 2018.
- [66] D. Roylance, "Article - Roylance - Fatigue MIT," pp. 2–10, 2001.
- [67] D. Wanger, N. Ranc, C. Bathias, and P. C. Paris, "Fatigue crack initiation detection by an infrared thermography method," *Fatigue Fract. Eng. Mater. Struct.*, vol. 33, no. 1, pp. 12–21, Nov. 2009.
- [68] N. Pugno, M. Ciavarella, P. Cornetti, and A. Carpinteri, "A generalized Paris' law for fatigue crack growth," *J. Mech. Phys. Solids*, vol. 54, no. 7, pp. 1333–1349, 2006.
- [69] T. M. Roberts and M. Talebzadeh, "Acoustic emission monitoring of fatigue crack propagation," *J. Constr. Steel Res.*, vol. 59, no. 6, pp. 695–712, 2003.
- [70] T. M. Roberts and M. Talebzadeh, "Fatigue life prediction based on crack propagation and acoustic emission count rates," *J. Constr. Steel Res.*, vol. 59, no. 6, pp. 679–694, 2003.
- [71] Z. Han, H. Luo, Y. Zhang, and J. Cao, "Effects of micro-structure on fatigue crack propagation and acoustic emission behaviors in a micro-alloyed steel," *Mater. Sci. Eng. A*, vol. 559, pp. 534–542, 2013.
- [72] Z. Han, H. Luo, J. Cao, and H. Wang, "Acoustic emission during fatigue crack propagation in a micro-alloyed steel and welds," *Mater. Sci. Eng. A*, vol. 528, no. 25–26, pp. 7751–7756, 2011.
- [73] M. Chai, J. Zhang, Z. Zhang, Q. Duan, and G. Cheng, "Acoustic emission studies for characterization of fatigue crack growth in 316LN stainless steel and welds," *Appl. Acoust.*, vol. 126, pp. 101–113, 2017.
- [74] M. Chai, Z. Zhang, Q. Duan, and Y. Song, "Assessment of fatigue crack growth in 316LN stainless steel based on acoustic emission entropy," *Int. J. Fatigue*, vol. 109, no. 28, pp. 145–156, 2018.
- [75] E. Limit, "Stress-Life Diagram (S-N Diagram)."
- [76] D. Fang and A. Berkovits, "Fatigue design model based on damage mechanism revealed by acoustic emission measurement," *ASME. J. Eng. Mater. Technol.*, vol.

## References

- 117, no. 2, pp. 200–208, 1995.
- [77] A. Ould Amer, A. L. Gloanec, S. Courtin, and C. Touze, “Characterization of fatigue damage in 304L steel by an acoustic emission method,” *Procedia Eng.*, vol. 66, pp. 651–660, 2013.
- [78] K. S. Han and K. H. Oh, “Acoustic Emission as a Tool of Fatigue Assessment,” *Key Eng. Mater.*, vol. 306–308, pp. 271–278, 2006.
- [79] A. Berkovits and D. Fang, “Study of fatigue crack characteristics by acoustic emission,” *Eng. Fract. Mech.*, vol. 51, no. 3, 1995.
- [80] R. GÜRBÜZ, “Metu department of metallurgical and materials engineering Met E 206 materials laboratory.”
- [81] V. Moorthy, T. Jayakumar, and B. Raj, “Acoustic emission technique for detecting micro- and macroyielding in solution-annealed AISI Type 316 austenitic stainless steel,” *Int. J. Press. Vessel. Pip.*, vol. 64, no. 2, pp. 161–168, 1995.
- [82] C. K. Mukhopadhyay, K. K. Ray, T. Jayakumar, and B. Raj, “Acoustic emission from tensile deformation of unnotched and notched specimens of AISI type 304 stainless steels,” vol. 255, pp. 98–106, 1998.
- [83] C. K. Mukhopadhyay, T. Jayakumar, B. Raj, and K. K. Ray, “The influence of notch on the acoustic emission generated during tensile testing of nuclear grade AISI type 304 stainless steel,” *Mater. Sci. Eng. A*, vol. 276, no. 1–2, pp. 83–90, 2002.
- [84] C. K. Mukhopadhyay, T. Jayakumar, B. Raj, and K. K. Ray, “Acoustic emission–stress intensity factor relations for tensile deformation of notched specimens of AISI type 304 stainless steel,” *Mater. Sci. Technol.*, vol. 18, no. 10, pp. 1133–1141, 2003.
- [85] C. K. Mukhopadhyay, T. Jayakumar, B. Raj, and K. K. Ray, “Acoustic emission during tensile deformation of pre-strained nuclear grade AISI type 304 stainless steel in the unnotched and notched conditions,” *J. Mater. Sci.*, vol. 42, no. 14, pp. 5647–5656, 2007.
- [86] C. K. Mukhopadhyay, K. V. Kasiviswanathan, T. Jayakumar, and B. Raj, “Acoustic emission during tensile deformation of annealed and cold-worked AISI type 304 austenitic stainless steel,” *J. Mater. Sci.*, vol. 28, no. 1, pp. 145–154, 1993.
- [87] K. Barat, H. N. Bar, D. Mandal, H. Roy, S. Sivaprasad, and S. Tarafder, “Low temperature tensile deformation and acoustic emission signal characteristics of AISI 304LN stainless steel,” *Mater. Sci. Eng. A*, vol. 597, pp. 37–45, 2014.
- [88] K. Máthiś, D. Prchal, R. Novotný, and P. Hähner, “Acoustic emission monitoring of slow strain rate tensile tests of 304L stainless steel in supercritical water environment,” *Corros. Sci.*, vol. 53, no. 1, pp. 59–63, 2011.
- [89] Z. Han, H. Luo, and H. Wang, “Effects of strain rate and notch on acoustic emission during the tensile deformation of a discontinuous yielding material,” *Mater. Sci. Eng. A*, vol. 528, no. 13–14, pp. 4372–4380, 2011.
- [90] N. Kiesewetter and P. Schiller, “The acoustic emission from moving dislocations in aluminium,” *Phys. Status Solidi*, vol. 38, no. 2, pp. 569–576, 1976.
- [91] A. B. Pattnaik, B. B. Jha, and R. Sahoo, “Effect of strain rate on acoustic emission during tensile deformation of  $\alpha$ -brass,” *Mater. Sci. Technol.*, vol. 29, no. 3, pp. 294–299, Mar. 2013.
- [92] I. G. Palmer, “Acoustic emission measurements on reactor pressure vessel steel,” *Mater. Sci. Eng.*, vol. 11, no. 4, pp. 227–236, 1973.
- [93] Y. F. S. V. G. Smirnov, “THE USE OF ACOUSTIC EMISSION FOR DETERMINATION OF FRACTURE TOUGHNESS AT CRYOGENIC TEMPERATURES,” *J Strength Mater.*, vol. 43, no. 11, pp. 24–27, 1991.
- [94] Y. Shindo, M. Sumikawa, F. Narita, and K. Sanada, “Acoustic emission and fracture behavior of GFRP woven laminates at cryogenic temperatures,” *Cryogenics*

## References

- (*Guildf.*), vol. 45, no. 6, pp. 439–449, 2005.
- [95] R. B. Kogbara, S. R. Iyengar, Z. C. Grasley, S. Rahman, E. A. Masad, and D. G. Zollinger, “Relating damage evolution of concrete cooled to cryogenic temperatures to permeability,” *Cryogenics (Guildf.)*, vol. 64, pp. 21–28, 2014.
- [96] D. H. Kohn, P. Ducheyne, and J. Awerbuch, “Acoustic emission during fatigue of Ti-6Al-4V: Incipient fatigue crack detection limits and generalized data analysis methodology,” *J. Mater. Sci.*, vol. 27, no. 12, pp. 3133–3142, 1992.
- [97] J. A. Pascoe, D. S. Zarouchas, R. C. Alderliesten, and R. Benedictus, “Using acoustic emission to understand fatigue crack growth within a single load cycle,” *Eng. Fract. Mech.*, vol. 194, no. March, pp. 281–300, 2018.
- [98] F. F. Barsoum, J. Suleman, A. Korcak, and E. V. K. Hill, “Acoustic emission monitoring and fatigue life prediction in axially loaded notched steel specimen,” *J. Acoust. Emiss.*, no. 27, pp. 40–63, 2009.
- [99] D. Gagar, P. Foote, and P. E. Irving, “Effects of loading and sample geometry on acoustic emission generation during fatigue crack growth: Implications for structural health monitoring,” *Int. J. Fatigue*, vol. 81, pp. 117–127, 2015.
- [100] M. Chai, Z. Zhang, and Q. Duan, “A new qualitative acoustic emission parameter based on Shannon’s entropy for damage monitoring,” *Mech. Syst. Signal Process.*, vol. 100, pp. 617–629, 2018.
- [101] C. Sauerbrunn, A. Kahirdeh, H. Yun, and M. Modarres, “Damage Assessment Using Information Entropy of Individual Acoustic Emission Waveforms during Cyclic Fatigue Loading,” *Appl. Sci.*, vol. 7, no. 6, p. 562, 2017.
- [102] M. G. R. Sause, “Investigation of pencil-lead breaks as acoustic emission sources,” *J. Acoust. Emiss.*, vol. 29, pp. 184–196, 2011.
- [103] P. Yilmazer, A. Amini, and M. Papaalias, “The Structural health condition monitoring of rail steel using acoustic emission techniques.”
- [104] J. C. Principe, *Information Theoretic Learning*. 2010.
- [105] R. V. L. Hartley, “Transmission Information,” *Bell Syst. Tech. J.*, vol. 7, no. 3, pp. 535–563, 1928.
- [106] Claude E. Shannon, “A Mathematical Theory of Communication,” *Bell Syst. Tech. J.*, vol. 27, pp. 623–656, 1948.
- [107] A. Rényi, “On measures of entropy and information,” *Proc. 4th Berkeley Symp. Math. Stat. Prob. Berkeley Univ. Press.*, vol. 1, pp. 457–561, 1960.
- [108] D. J. Cornforth, M. P. Tarvainen, and H. F. Jelinek, “How to Calculate Rényi Entropy from Heart Rate Variability, and Why it Matters for Detecting Cardiac Autonomic Neuropathy,” *Front. Bioeng. Biotechnol.*, vol. 2, pp. 1–8, 2014.
- [109] P. J. Coles, M. Berta, M. Tomamichel, and S. Wehner, “Entropic uncertainty relations and their applications,” *Rev. Mod. Phys.*, vol. 89, no. 1, pp. 1–65, 2017.
- [110] P. Bromiley, “Shannon entropy, Rényi entropy, and information,” *Stat. Inf. Ser.*, no. 2004, pp. 1–8, 2004.
- [111] S. Vinga and J. S. Almeida, “Rényi continuous entropy of DNA sequences,” *J. Theor. Biol.*, vol. 231, no. 3, pp. 377–388, 2004.
- [112] L. Zhang, Q. Cao, and J. Lee, “A novel ant-based clustering algorithm using Rényi entropy,” *Appl. Soft Comput. J.*, vol. 13, no. 5, pp. 2643–2657, 2013.
- [113] D. Sluga and U. Lotrič, “Quadratic mutual information feature selection,” *Entropy*, vol. 19, no. 4, pp. 1–16, 2017.
- [114] K. Ekstein and T. Pavelka, “Entropy And Entropy-based Features In Signal Processing,” *5th Int. PhD Work. Syst. Control a Young Gener. Viewp.*, pp. 1–2, 2004.
- [115] A. Vahaplar, C. Cengiz, and M. Zengin, “Entropy in dichotic

## References

- listening EEG recordings,” *Math. Comput. Appl.*, vol. 16, no. 1, pp. 43–52, 2011.
- [116] D. Erdogmus, *Information theoretic learning: Renyi’s entropy and its application to adaptive system training*. PhD Thesis, University of Florida, 2002.
- [117] V. Vijejan, M. Hariharan, S. Yaacob, M. N. B. Sulaiman, and A. H. Adom, “Objective investigation of vision impairments using single trial pattern reversal visually evoked potentials,” *Comput. Electr. Eng.*, vol. 39, no. 5, pp. 1549–1560, 2013.
- [118] V. Vijejan, H. M. S. Yaacob, and M. N. B. Sulaiman, “Application of clustering techniques for visually evoked potentials based detection of vision impairments,” *Biocybern. Biomed. Eng.*, vol. 34, no. 3, pp. 169–177, 2014.
- [119] “ASTM E466-15, Practice for conducting force controlled constant amplitude axial fatigue tests of metallic materials,” 2015.
- [120] ASTM E1106 - 12, “Standard Test Method for Primary Calibration of Acoustic Emission Sensors,” 2017.
- [121] P. A. Vanniamparambil, J. Cuadra, U. Guclu, I. Bartoli, and A. Kontsos, “Cross-validated detection of crack initiation in aerospace materials,” 2014.
- [122] P. A. Vanniamparambil, U. Guclu, and A. Kontsos, “Identification of Crack Initiation in Aluminum Alloys using Acoustic Emission,” *Exp. Mech.*, vol. 2015, no. 55, pp. 837–850.
- [123] K. Shrama, A. Clarke, R. Pullin, and S. L. Evans, “Detection of Cracking in Mild Steel Fatigue Specimens Using Acoustic Emission and Digital Image Correlation,” in *31st Conference of the European Working Group on Acoustic Emission (EWGAE)*, 2014.
- [124] S. Hensley, M. Christensen, S. Small, D. Archer, E. Lakes, and R. Rogge, “Digital image correlation techniques for strain measurement in a variety of biomechanical test models,” *Acta Bioeng. Biomech.*, vol. 19, no. 3, pp. 187–195, 2017.
- [125] D. G. Aggelis, E. Z. Kordatos, and T. E. Matikas, “Acoustic emission for fatigue damage characterization in metal plates,” *Mech. Res. Commun.*, vol. 38, no. 2, pp. 106–110, 2011.
- [126] M. D. Sangid, “The physics of fatigue crack initiation,” *Int. J. Fatigue*, vol. 57, pp. 58–72, 2013.
- [127] M. Risbet, P. Feissel, T. Roland, D. Brancherie, and J.-M. Roelandt, “Digital Image Correlation technique: application to early fatigue damage detection in stainless steel,” *Procedia Eng.*, vol. 2, pp. 2219–2227, 2010.
- [128] “Fatigue Fracture - an overview | ScienceDirect Topics.” [Online]. Available: <https://www.sciencedirect.com/topics/engineering/fatigue-fracture>. [Accessed: 20-Mar-2019].
- [129] K. Máthis, D. Prechal, R. Novotny’b, N. Novotny’b, and P. Hähner, “Acoustic emission monitoring of slow strain rate tensile tests of 304L stainless steel in supercritical water environment,” *Corros. Sci.*, vol. 53, pp. 59–63, 2011.
- [130] R. Singh, B. Raj, U. K. Mudali, and P. Singh, *Non-destructive evaluation of corrosion and corrosion-assisted cracking (chapter 1.4.2)*. 2019.
- [131] K. Ono, H. Cho, and M. Takuma, “THE ORIGIN OF CONTINUOUS EMISSIONS,” *J. Acoust. Emiss.*, vol. 23, pp. 206–214, 2005.
- [132] A. H. Aydilek, M. Guler, and T. B. Edil, “Use of Image Analysis in Determination of Strain Distribution During Geosynthetic Tensile Testing,” *J. Comput. Civ. Eng.*, vol. 18, no. 1, pp. 65–74, Jan. 2004.
- [133] NDT Resource Centre, “Tensile Properties.” [Online]. Available: <https://www.nde-ed.org/EducationResources/CommunityCollege/Materials/Mechanical/Tensile.php>. [Accessed: 28-Mar-2019].

## References

- [134] H. Lee, J. W. Kim, and C. Hwang, "Dynamic strength analysis of membrane type LNG containment system due to sloshing impact load," *Int. Conf. Des. Oper. Gas Carr.*, no. March, pp. 159–176, 2004.
- [135] S. H. B. & J. K. P. Sang Eui Lee, Bong Ju Kim, Jung Kwan Seo, Yeon Chul Ha, Toshiyuki Matsumoto, "Nonlinear impact response analysis of LNG FPSO cargo tank structures under sloshing loads," *Ships Offshore Struct.*, vol. 10, no. 5, pp. 510–532, 2015.
- [136] F. Hamel, "Acoustic Emission mechanism during high-cycle fatigue," *Eng. Fract. Mech. Vol.*, vol. 14, no. 4, pp. 853–860, 1981.
- [137] A. C. E. Sinclair and D. C. Connors, "Acoustic Emission Analysis during Fatigue Crack Growth in Steel," *Mater. Sci. Eng.*, vol. 28, p. 263, 1977.
- [138] Z. Han, H. Luo, C. Sun, J. Li, M. Papaelias, and C. Davis, "Acoustic emission study of fatigue crack propagation in extruded AZ31 magnesium alloy," *Mater. Sci. Eng. A*, vol. 597, pp. 270–278, 2014.
- [139] M. A. Hamstad and A. K. Mukherjee, "The dependence of acoustic emission on strain rate in 7075-T6 aluminum," *Exp. Mech.*, vol. 14, no. 1, pp. 33–41, Jan. 1974.
- [140] B. Raj and T. Jayakumar, "Acoustic Emission During Tensile Deformation and Fracture in Austenitic Alloys," in *Acoustic Emission: Current Practice and Future Directions*, 100 Barr Harbor Drive, PO Box C700, West Conshohocken, PA 19428-2959: ASTM International, 1991, pp. 218–241.
- [141] B. Raj, B. B. Jha, and P. Rodriguez, "Frequency spectrum analysis of acoustic emission signal obtained during tensile deformation and fracture of an AISI 316 type stainless steel," vol. 37, no. 8, pp. 2211–2215, 1989.
- [142] T. F. Drouillard *et al.*, "Acoustic emission produced by deformation of metals and alloys - A review," *J. Acoust. Emiss. (ISSN 0730-0050)*, vol. 6, pp. 177–204, 1987.
- [143] M. de Carvalho, "Mean, What do You Mean?," *Am. Stat.*, vol. 70, no. 3, pp. 270–274, 2016.
- [144] M. Kharrat, E. Ramasso, V. Placet, and M. L. Boubakar, "A signal processing approach for enhanced Acoustic Emission data analysis in high activity systems: Application to organic matrix composites," *Mech. Syst. Signal Process.*, vol. 70–71, pp. 1038–1055, 2016.
- [145] H. W. R. Christian U. Grosse, "Signal conditioning in acoustic emission analysis using wavelets," *NDT.net*, vol. 7, no. 9, 2002.

## Appendix A

### A.1 Equation for the modelled waveform

**Waveform 1:**  $y = \sin(2 \times \pi \times f \times t) \times e^{-3000 \times t}$

**Waveform 2:**  $y = \sin(2 \times \pi \times f \times t) \times e^{-6000 \times t}$

**Waveform 3:**  $y = \sin(2 \times \pi \times f \times t) \times e^{-12000 \times t}$

### A.2 Dispersion curve of the material used in this study

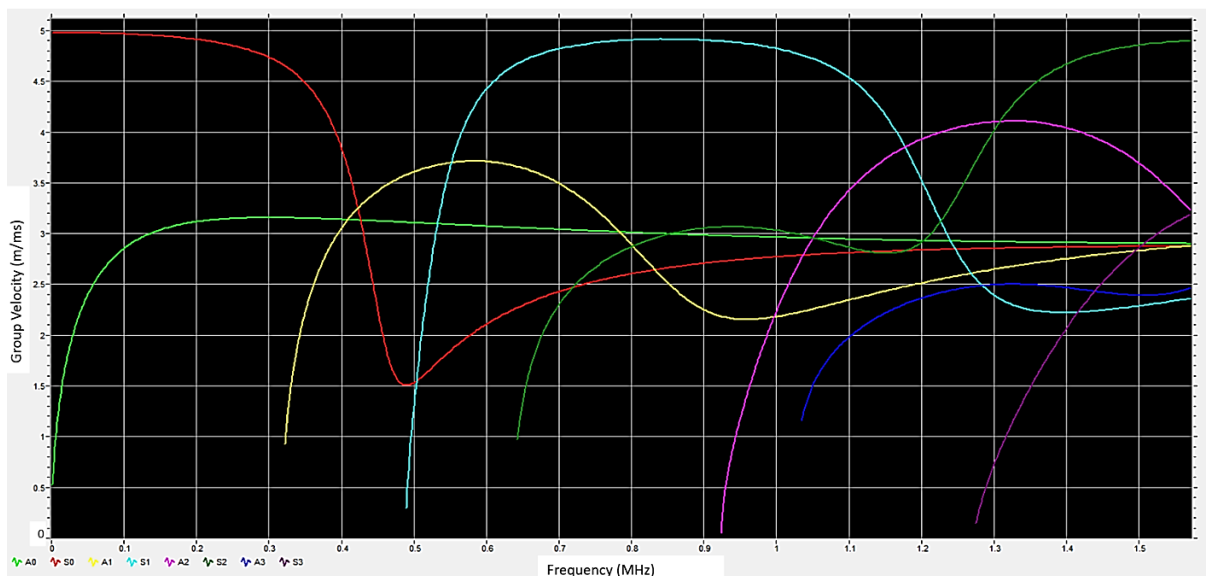


Figure A2: Dispersion curve of austenitic stainless steel

### A.3 Specification ARAMIS 3D 5MP system (DIC camera)

**Resolution:** 2448 x 2050 pixel

**Frame Rate:** 15Hz at full resolution or up to 29Hz at reduced resolution

**Camera support:** 150 / 300 600 / 1200 / 1600

### A.4 Representation of the increase in strain

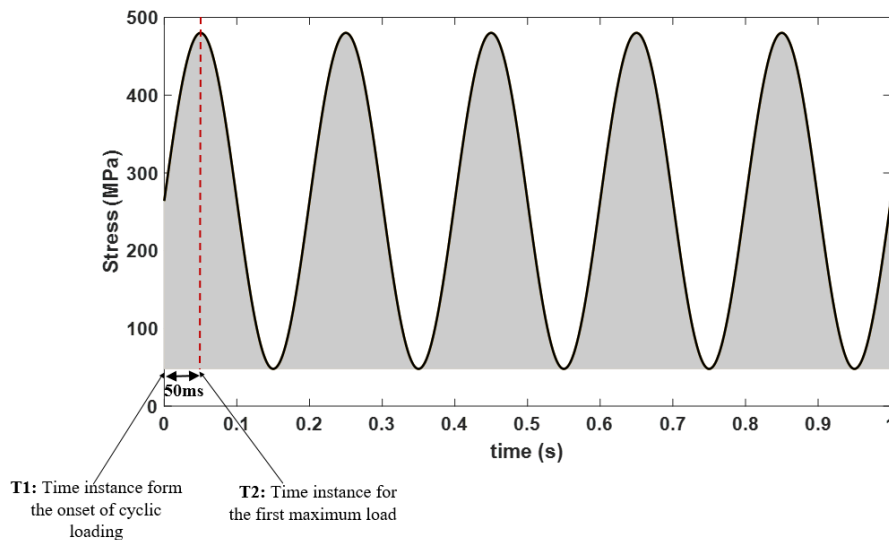


Figure A4: Illustration of the time taken to reach the first maximum load in a cycle

Time taken to reach the maximum stress after mean stress =  $T2 - T1 = 0.05s$

Since there is only a little variance in strain throughout the test, after the onset of sinusoidal loading. It can be assumed that the strain recorded by the loading machine after the first 76 cycles is equal to the strain caused due to the first maximum load.

### A.5 Postulates of Renyi's and Shannon's Entropy

Renyi's and Shannon's entropy is a function of the probability of mass  $P(x)$ . Therefore, they can be represented by the function  $H(p) = H(p_1, p_2, \dots, p_n)$ . There are five simple postulates that characterizes each Renyi's and Shannon's entropy. Among the five postulates, both Renyi's and Shannon's entropy shares four common postulates, which are as follows:

**Postulate 1:**  $H(p_1, p_2, \dots, p_n)$  is a symmetric function of the variable  $n = 1, 2, \dots, n$ .

**Postulate 2:**  $H(p_1, p_2, \dots, p_n)$  is a continuous function of  $p$ .

**Postulate 3:**  $H\left(\frac{1}{2}, \frac{1}{2}\right) = 1$

**Postulate 4:**  $H(p \times q) = H(p) + H(q)$ .

Entropy of an experiments that includes the contribution of the outcome of two experiments is sum of the entropies of the individual experiments.

The one postulate for which the Renyi's and Shannon's entropy differ are as follows:

**Postulate 5 (Shannon):**  $H(P \cup Q) = \frac{w(P)H(P) + w(Q)H(Q)}{w(P) + w(Q)}$

The total entropy as a result of the union of two incomplete distributions is the weighted mean value of the entropy of the respective distribution. This postulate is also called the arithmetic mean value property of the Shannon's entropy.

If  $H(p)$  satisfies postulates 1,2,3,4 and 5 then  $H(p) = H_1(p)$ , where

$$H_1(p) = \frac{\sum_{k=1}^m p_k \log \frac{1}{p_k}}{\sum_{k=1}^m p_k}$$

**Postulate 5\* (Renyi):**  $g^{-1} \left[ H(P \cup Q) = \frac{w(P)H(P) + w(Q)H(Q)}{w(P) + w(Q)} \right]$

$$\text{Where } g_a(x) = 2^{(a-1)x}$$

There exist an exponentially monotonic and continuous function of  $g(x) = g_a(x)$  which is also admissible.

If  $H(p)$  satisfies postulates 1,2,3,4 and 5\* then  $H(p) = H_a(p)$ , where

## Appendix A

$$H_a(p) = \frac{1}{a-1} \log \frac{\sum_{k=1}^m p_k^a}{\sum_{k=1}^m p_k}$$